Impact of turbulent mixing on the UTLS chemistry and radiation in chemistry climate models

Dissertation submitted
for the award of the title
Doctor of Natural Sciences (Dr. rer. nat.)
to the faculty of Physics, Mathematics, and Computer Science
of Johannes Gutenberg University Mainz
in Mainz

Chun Hang Chau

born 17.12.1997 in Hong Kong

Mainz, November 16, 2025

JOHANNES GUTENBERG UNIVERSITÄT MAINZ

JG|U

1. Examiner:
2. Examiner:
Day of the oral examination: January 7, 2026

Declaration

I hereby declare that I wrote this dissertation without any unauthorized or unacknowledged external assistance and I have used only those sources and aids which are duly cited in the text. All passages and figures derived from published or unpublished work are clearly marked, and their sources are listed in accordance with bibliographical rules. Throughout this research, I complied with the rules of standard scientific practice as set forth in the statutes of Johannes Gutenberg University Mainz.

Chun Hang Chau
Mainz, 16 November 2025

Acknowledgments

Zusammenfassung

Die obere Troposphäre und untere Stratosphäre (UTLS) spielen eine wichtige Rolle für das Erdklima, da diese Region den Strahlungshaushalt der Erde beeinflusst. Die Oberflächentemperatur reagiert empfindlich auf Veränderungen strahlungsaktiver Gase in der UTLS-Region. Der Stratosphären-Troposphären-Austausch (STE), ein bidirektionaler Austauschprozess zwischen Stratosphäre und Troposphäre, ist der Hauptweg des Austauschs zwischen beiden Sphären. Turbulente Vermischung durch Clear-Air-Turbulenz (CAT) als Form des STE kann die chemischen Substanzen zwischen Stratosphäre und Troposphäre schnell vermischen, insbesondere in der Nähe der Tropopause und des Jetstreams. Es wird auch erwartet, dass sich CAT unter dem Klimawandel intensiviert. Angesichts der Bedeutung des STE und seiner Verbindung mit turbulenter Vermischung sowie des zunehmenden Trends von CAT wird das Verständnis und die Darstellung des Prozesses, wie turbulente Vermischung die UTLS-Chemie und den Strahlungshaushalt der Erde umverteilen kann, zu einer entscheidenden Aufgabe.
Die erste Studie, die in dieser Arbeit vorgestellt wird, führte ein verbessertes vertikales Setup EH-84 mit hoher vertikaler Auflösung in der UTLS für das mesoskalige Klimachemiemodell MECO(n) und eine neuartige diagnostische Delta-Tracer-Tracer-Korrelation ein. Dieses neue vertikale Setup bietet ein geeignetes Werkzeug, um den bidirektionalen Transport über die Tropopause hinweg zu verstehen und zu quantifizieren, und ermöglicht eine detailliertere Analyse kleinskaliger Prozesse. Die Delta-Tracer-Tracer-Korrelation bietet auch eine neue Methode zur Trennung der alleinigen Auswirkung eines einzelnen Prozesses in einer Modellsimulation. Diese Studie konzentriert sich auf die Auswirkung turbulenter Vermischung auf Tracer in der UTLS. Die Ergebnisse zeigen, dass das verbesserte Setup in der Lage ist, mehrere unterschiedliche turbulente Vermischungsereignisse in der UTLS mit verschiedenen Eigenschaften zu erfassen, die durch Turbulenz und starke vertikale

Tracergradienten induziert werden.
Die zweite Studie, die in dieser Arbeit vorgestellt wird, untersucht die Sensitivität turbulenter Vermischung durch CAT auf die UTLS-Chemie und ihre strahlungsbezogenen Auswirkungen. Dies wurde durch die Implementierung eines neuen Submodells CAT im Klimachemiemodell EMAC durchgeführt. Diese Studie führte eine neue Turbulenzdiagnostik MoCATI ein, die auf vertikaler Windscherung, Deformation, Divergenztrend und statischer Stabilität basiert und als Vermischungskoeffizient des CAT-Vermischungsschemas dient. Die Simulationsergebnisse zeigen, dass Ozon in der UTLS nach Aktivierung des CAT-Submodells signifikant um 10 bis 20% reduziert wird, was nicht nur zu rein physikalischer Vermischung führt, sondern auch zur chemischen Rückkopplung anderer durch CAT vermischter Tracer. Die Umverteilung von Tracern durch CAT veränderte auch das chemische Regime von Ozon und die Methanlebensdauer. Die Ergebnisse zeigen auch, dass die turbulente Vermischung zu einer Strahlungsabkühlung an der Obergrenze der Atmosphäre (TOA) von etwa 0,2 W/m^2 .
Die dritte Studie erweitert das CAT-Vermischungsschema von EMAC von der alleinigen Anwendung auf Tracer auf die Anwendung auf Wasserdampf und Temperatur. Die Ergebnisse zeigen einen signifikanten Anstieg des Wasserdampfs in der Nähe der Tropopause, was eine signifikanten Strahlungserwärmung von 0,79 W/m^2 bewirkt.
Die vierte Studie bereitet das Simulationssetup für die TPEx I-Messkampagne von TPChange vor und untersucht die Darstellung der synoptischen Repräsentation des mehrskaligen Klimachemiemodells MECO(n). Die Ergebnisse zeigen, dass die grobe horizontale Auflösung von EMAC innerhalb von MECO(n) zu Abweichungen synoptischer Merkmale in den eingebetteten COSMO-Instanzen führen kann, was zu Schwierigkeiten beim direkten Vergleich mit Messungen führt. Die Erhöhung der horizontalen Auflösung von EMAC könnte die Darstellung synoptischer Merkmale verbessern.
Diese Arbeit erweitert unser Wissen über die Rolle turbulenter Vermischung auf Tracer in der UTLS, indem sie Werkzeuge zur Untersuchung der Darstellung kleinskaliger Prozesse wie turbulenter Vermischung in MECO(n) bereitstellt. Durch die Parametrisierung turbulenter Vermischung in EMAC wurde das Verständnis verbessert, wie Clear-Air-Turbulenz die UTLS-Chemie und Strahlung prägen kann.

Schließlich verbesserte die Untersuchung der MECO(n)-Darstellung das Verständnis dafür, wie die Modelldynamik auf unterschiedliche Auflösungen reagiert.

Abstract

The upper troposphere lower stratosphere (UTLS) plays an important role on Earth's climate by affecting the Earth's radiation budget. Surface temperature is sensitive to changing radiatively active gases in the UTLS region. Stratosphere-troposphere exchange (STE), the bi-directional exchange process between the stratosphere and troposphere is the major pathway of exchange between both spheres. Turbulent mixing by clear air turbulence (CAT), as a form of STE, could rapidly mix the chemical species between the stratosphere and troposphere, especially near the tropopause and jet stream. CAT is also expected to intensify under climate change. Considering the importance of STE and its link with turbulent mixing, and the increasing trend of CAT, understanding and representing the process on how turbulent mixing could redistribute the UTLS chemistry and its corresponding impact on Earth's radiation budget is becoming a crucial task.

The first study presented in this thesis introduced an enhanced vertical setup EH-84 with high vertical resolution in the UTLS for the multi-scale climate chemistry model MECO(n), and a novel diagnostic delta tracer-tracer correlation. This new vertical setup provides a suitable tool to understand and quantify the bidirectional cross-tropopause transport and allows a more detailed analysis on small-scale processes. The delta tracer-tracer correlation also provides a new method on separating the sole impact of a single process in a model simulation. This study focuses on the impact of turbulent mixing on tracers in the UTLS. The result shows that the enhanced setup is able to capture several distinct turbulent mixing events in the UTLS with different characteristics induced by turbulence and strong vertical tracer gradient.

The second study presented in this work investigates the sensitivity of turbulent mixing by CAT on the UTLS chemistry and its radiative impact. It is done by implementing a new submodel CAT in the climate chemistry model EMAC. This

study introduced a new turbulence diagnostic MoCATI based on vertical wind shear, deformation, divergent trend and static stability, as the mixing coefficient of the CAT mixing scheme. Simulation result shows that ozone in the UTLS is significantly reduced by 10 to 20% after enabling the CAT submodel. It is a result of not only the pure physical mixing but also the chemical feedback of other tracers mixed by CAT. The redistribution of tracers by CAT also changed the chemical regime of ozone and the methane lifetime. The result also shows the turbulent mixing leads to radiative cooling at the top of the atmosphere (TOA) for about 0.2 W/m^2.

The third study extends the CAT mixing scheme of EMAC from only applied on tracers to applied on water and temperature as well. Result shows a significant increase of water vapour near the tropopause, leads to a significant radiative heating of 0.79 W/m^2.

The fourth study prepares the simulation setup for the TPEx I measurement campaign of TPChange, examines the synoptic representation of the multi-scale climate chemistry model MECO(n). Result shows the coarse horizontal resolution of EMAC within MECO(n) could lead to deviation of synoptic features in the nested COSMO instances, leading to difficulties in direct comparison with measurements. Increasing the EMAC horizontal resolution could improve the representation of synoptic features.

This thesis enhanced our knowledge on the role of turbulent mixing on tracers in the UTLS by providing tools to investigate the representation of small-scale process e.g. turbulent mixing in MECO(n). By parametrizing turbulent mixing in EMAC, it enhanced the understanding of how clear air turbulence could shape the UTLS chemistry and radiation. Finally, the investigation on the MECO(n) representation enhanced the understanding on how the model dynamics respond to different model resolutions.

Contents

1 Motivation

The upper troposphere lower stratosphere (UTLS) plays an important role on Earth's climate. The chemical composition of the UTLS is crucial to the Earth's climate by affecting the radiation budget (Forster et al., 2021). The surface temperature is most sensitive to the distribution of the radiatively active gases in the UTLS (Riese et al., 2012). Stratosphere-troposphere exchange (STE) is the major process that modifying the UTLS chemical composition (Holton et al., 1995; Stohl et al., 2003). Besides of changing the radiative balance, STE is also responsible for the ozone budget in both the stratosphere and troposphere (Butchart and Scaife, 2001; Lelieveld and Dentener, 2000). Previous study from Stevenson et al. (2006) shows that the model representation of STE determine the upper troposphere ozone budget. Therefore, it is crucial to understand and improve the representation of STE in the model. Turbulent mixing, as one of the pathway of STE (Holton et al., 1995; Shapiro, 1980), is important to investigate its role on mixing the chemicals in the UTLS and improve its representation in the models. However, previous studies mainly focus on the dynamical aspect of turbulence (Kaluza et al., 2021; Muñoz-Esparza et al., 2020), but not on it impact on tracers. The turbulent mixing of tracer is also not represented well in several state-of-the-art chemistry climate models, such as EMAC (Jöckel et al., 2010).

Clear air turbulence (CAT) is the major types of turbulence that occurs in the UTLS (Dutton and Panofsky, 1970). It refers to turbulence occurs in the cloud free region (Ellrod et al., 2003), commonly found near the tropopause (Dutton and Panofsky, 1970; Wolff and Sharman, 2008), and jet stream (Keller, 1990; Traub and Lelieveld, 2003). CAT could lead to rapid mixing of chemical species between stratosphere and troposphere (Traub and Lelieveld, 2003). It is also expected to become more frequent and stronger under climate change (Williams, 2017). Considering the increasing trend of CAT and its role on STE, it is crucial to

investigate how CAT could modify the UTLS composition.

This thesis improves the understanding on how turbulent mixing modified the tracers in the UTLS by introducing a new high vertical resolution setup EH-84 for the multi-scale climate chemistry model MECO(n) as a tool for studying the small scale processes e.g. turbulent mixing in the UTLS, and a novel diagnostic delta tracer-tracer correlation to determine the impact and direction of turbulent mixing. This thesis also improves the representation of turbulent mixing on tracers in the climate-chemistry model EMAC by parametrizing CAT based on turbulence diagnostics. With the new parametrization, the thesis further investigate the sensitivity of radiatively active gases on vertical mixing by CAT in the UTLS, and its corresponding radiative impact. The impact of vertical mixing by CAT on the UTLS chemistry is also examined. Moreover, this work investigates the representation of specific synoptic event in MECO(n), providing a foundation for simulating the UTLS region for future measurement campaign.

2 Introduction

2.1 Upper troposphere lower stratosphere (UTLS)

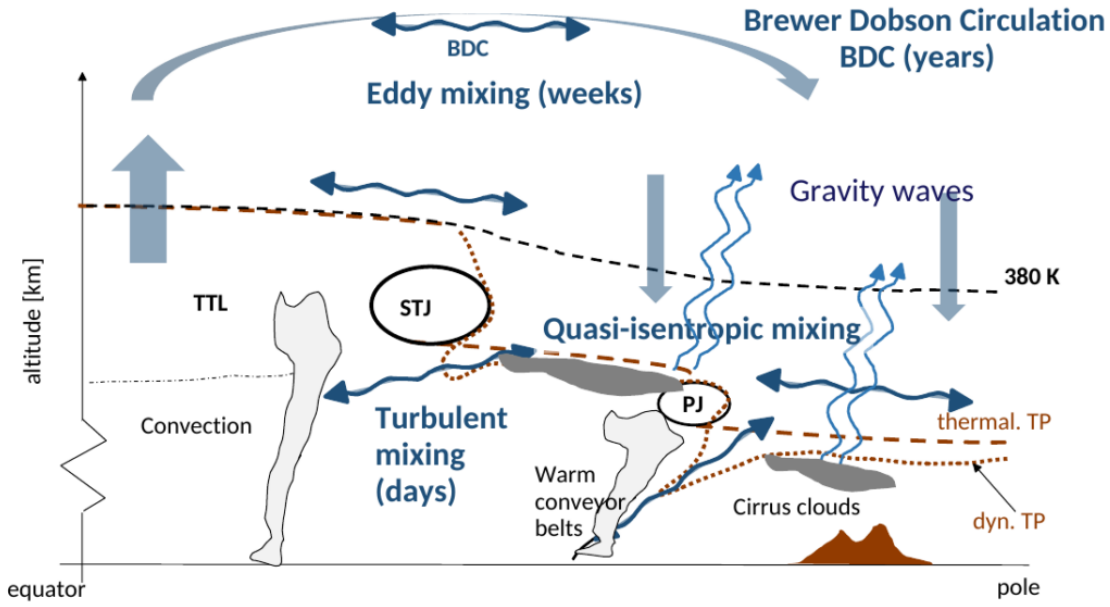

Figure 2.1: Schematic of the overview from Hoor (2022)

The upper troposphere and lower stratosphere (UTLS) is defined as the region ±5 km around the tropopause (Gettelman et al., 2011). This region acts as a transition layer between the well-mixed troposphere and the stably stratified stratosphere. They are separated by the tropopause, which serves as a transport barrier between the stratosphere and troposphere. The UTLS chemical composition plays an important role in the Earth's climate by influencing the radiation budget (Forster et al., 2021). Changes of the chemical composition in the UTLS could change the climate locally as well as at the surface. Previous studies show that

the surface temperature and Earth's radiation budget is sensitive to the changes in water vapour and ozone in the UTLS (Riese et al., 2012; Lacis et al., 1990; Randel et al., 2007; de F. Forster and Shine, 1997; Forster and Shine, 2002). Stratosphere-troposphere exchange (STE) is the bidirectional process that exchanges mass and chemical species between the stratosphere and troposphere (Holton et al., 1995). Besides of changing the radiative balance, STE also affects the chemistry in the stratosphere like stratospheric ozone recovery (Butchart and Scaife, 2001) and in the troposphere like tropospheric ozone budget (Lelieveld and Dentener, 2000)

2.1.1 Tropopause

The tropopause is the boundary between the stratosphere and troposphere that separates these spheres. Considering the complexity of the UTLS, the tropopause is defined differently depending on the chemical, dynamical and thermal properties. The tropopause height might vary as well depending on the definition of tropopause.

Lapse rate tropopause

The lapse rate tropopause, also known as the thermal tropopause, is defined using the lapse rate of the temperature $\Gamma = -\frac{\partial T}{\partial z}$. According to the World Meteorological Organization (1957), the lapse rate tropopause is defined as the lowest altitude that $\Gamma < 2\text{K/km}$, while the average lapse rate within 2 km above this altitude needs to be $< 2\text{K/km}$ as well. The thermal tropopause has the advantage of being easily determined by simple measurements like radiosondes. With the long history of radiosonde measurements, the trend of the thermal tropopause can be examined.

PV tropopause

The PV (Potential vorticity) tropopause, also known as the dynamical tropopause, is another widely used definition of tropopause. PV is a dynamical quantity combining the horizontal vorticity with the vertical static stability. It can be expressed

with static stability and absolute vorticity as:

$$PV = N^2 \frac{\theta}{\rho g}(\zeta_\theta + f) \tag{2.1}$$

The N^2 is the Brunt–Väisälä frequency$\frac{g}{\theta}\frac{\partial \theta}{\partial z}$, ζ_θ is the relative vorticity, f is the Coriolis parameter, θ, ρ and g represent potential temperature, air density and gravitational acceleration respectively.

The PV tropopause is defined by the PV value (1 PVU = 1×10^{-6} K m$^2 kg^{-1} s^{-1}$), 2 PVU (-2 for Southern hemisphere) is the most commonly used value (Stohl et al., 2003). Considering PV is conserved under adiabatic conditions, the PV tropopause is a quasi-impermeable surface, stratosphere-troposphere exchange across the PV tropopause is mostly required diabatic processes, e.g. turbulence mixing (Holton et al., 1995).

2.1.2 Jet stream

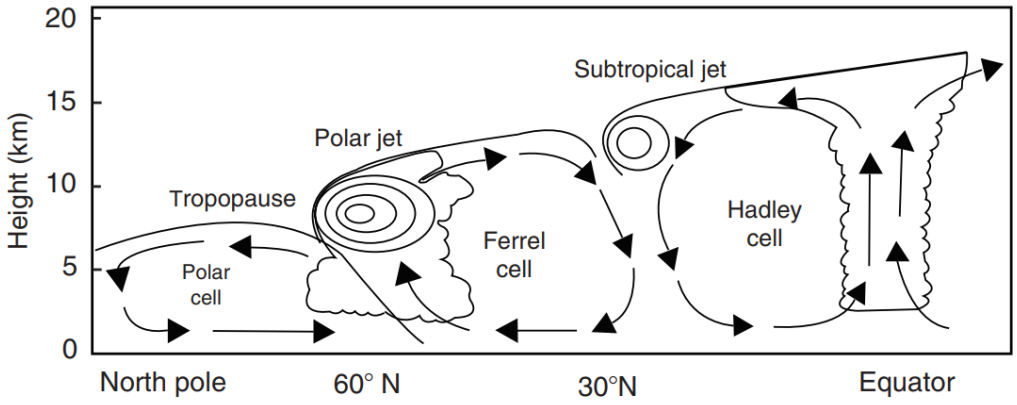

Figure 2.2: Positions of the meridional circulation and jet stream from Mohanakumar (2008)

Jet streams are the discontinuous, meandering bands of relatively strong wind near the tropopause. They form because of the meridional temperature gradient. According to the thermal wind relation, the stronger the horizontal temperature gradient, the stronger the vertical wind shear. There are two main types of jet streams: the polar jet and the subtropical jet. The polar jet and the subtropical jet

are located at around 50-60° and 30-40° respectively. The vicinity of the jet stream also experienced strong wind shear considering its high wind speed compared with the surrounding (Mohanakumar, 2008).

2.1.3 Stratosphere-Troposphere Exchange (STE)

The stratosphere-troposphere exchange is crucial for the chemical composition in the UTLS. STE is the bi-directional process that exchanges air mass between both spheres. The one-directional transport is referred to as stratosphere-to-troposphere transport (STT) and troposphere-to-stratosphere transport (TST). In terms of the global aspect of STE, it is mainly contributed by the Brewer-Dobson circulation, which brings the tropical tropospheric air vertically into the stratosphere, and horizontally advected to the extratropics and finally descends to the troposphere again in the extratropics and polar region (Holton et al., 1995). The tropopause fold is another dynamical process that leads to STE, especially in the extratropics. Tropopause fold is responsible for 50 to 70% of STE mass transport in the subtropics (Sprenger et al., 2003). The tropopause fold is the intrusion of stratospheric air into the troposphere. It forms when the tropopause level descends strongly near the jet. It mostly occurs near the tropical and polar jet stream. Previous study shows that turbulence is one of the important mechanism that occurs near to the jet stream which leads to significant exchange of air and chemical species between stratosphere and troposphere (Shapiro, 1980).

2.1.4 Clear Air Turbulence (CAT)

Turbulence is a fluid with irregular or seemingly random motion. It appears everywhere in the atmosphere. CAT is the major type of turbulence in the UTLS region and occurs frequently near the tropopause (Dutton and Panofsky, 1970; Wolff and Sharman, 2008) and jet stream (Keller, 1990; Traub and Lelieveld, 2003). It refers to turbulence in the free atmosphere that occurs in a cloud free region (Ellrod et al., 2003). It has a lifetime of 1 hour to a day, with a typical vertical length of 500 to 1000 m (Overeem, 2002). Kelvin–Helmholtz instability (KHI) is the major mechanism that leads to CAT formation (Watkins and Browning, 1973; Ellrod and Knapp, 1992). KHI occurs in stable layer when there is vertical wind shear.

CAT occurs when the vertical wind shear is strong enough to overcome the inhibition of the stable atmosphere (Williams and Joshi, 2013). Besides of vertical wind shear, deformation and divergence are also favouring the formation of CAT (Ellrod and Knox, 2010). CAT is important for the distribution of the UTLS chemical composition because it could rapidly mix the chemical species between stratosphere and troposphere as a form of STE (Traub and Lelieveld, 2003; Esler and Polvani, 2004). Recently proved tropopause shear layer (Kaluza et al., 2021) also shows the increasing importance on how it could affect the UTLS. CAT is becoming more frequent and intense considering climate change is strengthening the vertical wind shear (Williams, 2017). Recent study already shown an increasing trend between 1979 to 2017 for vertical wind shear in the North Atlantic by 15% (Lee et al., 2019). CAT is expected to increase in different region under different future scenario. Storer et al. (2017) shows that under the IPCC RCP 8.5 scenario, there will be over 100% increase of CAT in the mid latitudes of both hemisphere. Williams and Joshi (2013) also suggested similar results that the North Atlantic CAT will strengthen and more frequent if the atmospheric CO_2 is doubled to the pre-industrial time. Other studies also show similar increment for CAT under different future climate scenario (Smith et al., 2023; Hu et al., 2021). Therefore, there is an increasing importance on examining the impact of CAT on STE, hence the climate.

2.2 Chemistry

This section provides a brief overview of the stratospheric and tropospheric chemistry, mainly based on Ritchie (2017) and Seinfeld and Pandis (2006) with additional insights from Warneck (1999) and Brasseur and Jacob (2017).

2.2.1 Stratospheric chemistry

The stratospheric chemistry is mainly governed by odd oxygen O_x ($O + O_3$) and the related catalytic cycle. Since over 90% of ozone resides in the stratosphere, the stratospheric chemistry revolves around the production and loss of ozone. The production of stratospheric ozone is by the photodissociation of O_2 into atomic O,

which reacts with another O_2 molecule. The loss of stratospheric ozone is mainly due to the catalytic cycle with HO_x, NO_x and other halogen species.

Stratospheric ozone: The Chapman cycle

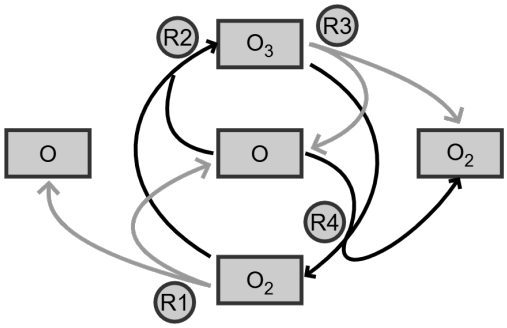

Figure 2.3: Schematic of the Chapman cycle, the grey line indicates the photolysis reaction. Figure by the author, based on Ritchie (2017).

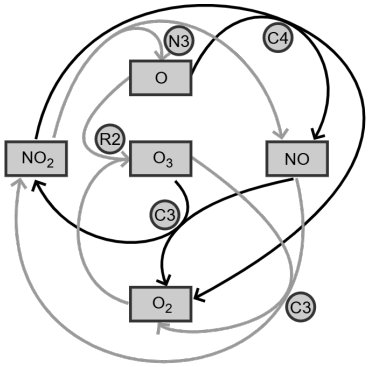

Figure 2.4: Schematic of the NO_X catalytic (black lines) and null (grey lines) cycle. Figure by the author.

The Chapman cycle, proposed by Sydney Chapman (1888-1970) in 1930, explains the origin of the ozone layer in the stratosphere. The Chapman cycle involves 4 reactions:

$$O_2 \xrightarrow{h\nu\,(\lambda < 242\text{ nm})} O + O \tag{R1}$$

$$O + O_2 + M \longrightarrow O_3 + M \tag{R2}$$

$$O_3 \xrightarrow{h\nu\,(\lambda < 1180\text{ nm})} O + O_2 \tag{R3}$$

$$O + O_3 \longrightarrow 2\,O_2 \tag{R4}$$

Reaction R1 is the main source of the stratospheric ozone; it requires high-energy photons from the ultraviolet radiation which is only found in the upper part of the atmosphere, e.g. stratosphere. It photodissociates the molecular oxygen into two atomic oxygen. The atomic oxygen then combines with another molecular oxygen by a three-body reaction to form ozone (R2). The third body M is an inert

molecule which required to stabilize the product. The ozone is then photolyzed by the photons from ultraviolet, visible and near infrared radiation to produce atomic oxygen and molecular oxygen (R3). The form of the atomic oxygen depends on the wavelength of the radiation, with $\lambda > 320$ nm, it produces the atomic oxygen in its electronically ground state $O(^3P)$. If the radiation have a wavelength with $\lambda < 320$ nm, it produces the atomic oxygen in its electronically excited state $O(^1D)$. Reaction R2 and R3 interconvert the odd oxygen and determine the O/O_3 ratio in the atmosphere. The atomic oxygen produced by R3 is either combined again with molecular oxygen to regenerate ozone (R2) or react with ozone to form two molecular oxygen (R4). In the Chapman cycle, the ozone concentration is controlled by the production of R2 by the production of atomic oxygen from R1 and the loss by R4. R3 is not an actual loss for ozone since the atomic oxygen instantaneously converts back into ozone. R2 by the production of atomic oxygen from R3 is also not an actual source of ozone. The ozone by R2 by the production of atomic oxygen from R1 peaks at around 40 km since the energetic photon required for photolysis increases with height. However, the maximum ozone concentration is located at around 25 km (Figure 2.5) because of the sink by R4 increasing with height due to the abundance of atomic oxygen.

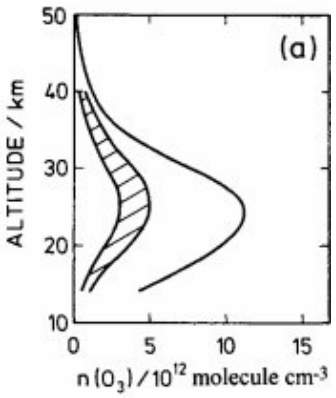

Figure 2.5: Vertical profile of ozone number density by Warneck (1999). The shaded area represents the measured profile, the solid line represents the calculated values by the Chapman cycle.

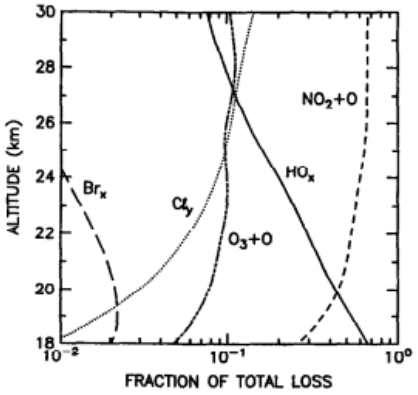

Figure 2.6: Fractional contributions of the ozone loss by species at 30N. Figure from McElroy et al. (1992)

Stratospheric ozone: Catalytic cycle

By only considering the oxygen only Chapman cycle, there is still a discrepancy between the calculated and the measured values (Figure 2.5). Additional ozone-destroying mechanisms beyond R4 had to be involved. Several catalytic cycles play roles in destroying the ozone in the stratosphere. A generic catalytic odd oxygen removal reaction cycle is:

$$\mathrm{X} + \mathrm{O_3} \longrightarrow \mathrm{XO} + \mathrm{O_2} \tag{C1}$$

$$\mathrm{XO} + \mathrm{O} \longrightarrow \mathrm{X} + \mathrm{O_2} \tag{C2}$$

$$\overline{\text{Net: } \mathrm{O} + \mathrm{O_3} \longrightarrow 2\,\mathrm{O_2}}$$

The X in the cycle is consumed and regenerated in the following steps, so that the removal of odd oxygen does not change the abundance of the catalytic X. The most important X are NO, H, OH and other halogen species like Cl, Br. The reaction C2 is a time-limiting step, competing with another cycle that interconverts X and XO

without removing odd oxygen. This is the null cycle competing with the catalytic cycle:

$$X + O_3 \longrightarrow XO + O_2 \tag{C1}$$
$$XO + NO \longrightarrow X + NO_2 \tag{N2}$$
$$NO_2 \xrightarrow{h\nu\,(\lambda < 410\text{ nm})} NO + O \tag{N3}$$
$$O + O_2 + M \longrightarrow O_3 + M \tag{R2}$$

Both cycle with the same reaction C1 converts X to XO, but the photolysis of NO_2 in N3 of the null cycle leads to the formation of atomic oxygen, which converts back to ozone via R2 of the Chapman cycle. Figure 2.6 shows the relative importance of the ozone loss species. NO_x and HO_x are of most important and is discussed specifically below. The main source of NO in the stratosphere is the oxidation of N_2O ($N_2O + O(^1D) \longrightarrow 2\,NO$). The NO then reacts with O_3 to form NO_2 and O_2 (C3), the NO_2 then reacts with O to regenerate NO. The catalytic cycle of NO_x can be written as:

$$NO + O_3 \longrightarrow NO_2 + O_2 \tag{C3}$$
$$NO_2 + O \longrightarrow NO + O_2 \tag{C4}$$
$$\overline{\text{Net: } O + O_3 \longrightarrow 2\,O_2}$$

The catalytic NO_x cycle is terminated by losing NO_x into an relatively stable reservoir like HNO_3 ($NO_2 + OH + M \longrightarrow HNO_3 + M$) or N_2O_5 ($NO_2 + O_3 \longrightarrow NO_3 + O_2$ then $NO_3 + NO_2 \longrightarrow N_2O_5$). As mentioned above, reaction C4 is the time-limiting step and competes with the null cycle that interconverts NO and NO_2:

$$NO_2 \xrightarrow{h\nu\,(\lambda < 410\text{ nm})} NO + O \tag{N3}$$
$$O + O_2 + M \longrightarrow O_3 + M \tag{R2}$$
$$NO + O_3 \longrightarrow NO_2 + O_2 \tag{C3}$$

The NO_2 can photolysed as NO and O (N3) instead of reacting with O to form NO and O_2 (C4). The schematic of the NO_x cycle are shown in Figure 2.4.

Another important catalytic cycle would be the HO_x cycle. The OH is produced through $O(^1D) + H_2O \longrightarrow 2\,OH$, where the $O(^1D)$ is a product of the O_3 photolysis. The OH radicals then interconvert to HO_2 through the catalytic cycle to destroy odd oxygen. The HO_x catalytic cycle can be written as:

$$OH + O_3 \longrightarrow HO_2 + O_2 \tag{C5}$$
$$HO_2 + O \longrightarrow OH + O_2 \tag{C6}$$
$$\overline{\text{Net: } O + O_3 \longrightarrow 2\,O_2}$$

This cycle involving O is becoming inefficient when it goes down to the lower stratosphere where the amount of O is markedly reduced. An alternative reaction occurs by involving O_3 in both steps:

$$OH + O_3 \longrightarrow HO_2 + O_2 \tag{C5}$$
$$HO_2 + O_3 \longrightarrow OH + 2\,O_2 \tag{C7}$$
$$\overline{\text{Net: } 2\,O_3 \longrightarrow 3\,O_2}$$

Reaction C6/C7 is also the time-limiting step competing with the null cycle:

$$OH + O_3 \longrightarrow HO_2 + O_2 \tag{C5}$$
$$HO_2 + NO \longrightarrow OH + NO_2 \tag{N3}$$
$$NO_2 \xrightarrow{h\nu\,(\lambda < 410\text{ nm})} NO + O \tag{N5}$$
$$O + O_2 + M \longrightarrow O_3 + M \tag{R2}$$

The HO_x cycles are terminated by removing HO_x radicals to form H_2O ($OH + HO_2 \longrightarrow H_2O + O_2$) and H_2O_2 ($HO_2 + HO_2 \longrightarrow H_2O_2 + O_2$), and HNO_3 as mentioned for the termination of the NO_x cycle.

2.2.2 Tropospheric chemistry

Tropospheric chemistry is significantly more complex than stratospheric chemistry. The hydroxyl radical OH becomes the key to understanding the tropospheric chemistry since it reacts with almost all of the trace species in the troposphere, serving as the atmosphere's detergent. In the other hand, the tropospheric ozone cannot be simply explained by the transportation of the stratospheric ozone and is explained by additional mechanisms.

The hydroxyl radical OH

The hydroxyl radical OH is the most important radical in the atmosphere. The OH is formed by the photolysis of O_3 with ultraviolet radiation and the reaction with H_2O:

$$O_3 \xrightarrow{h\nu\,(\lambda \leq 310\text{ nm})} O(^1D) + O_2 \tag{R5}$$

$$O(^1D) + H_2O \longrightarrow 2\,OH \tag{R6}$$

CH_4 oxidation with OH

Methane is abundant in the troposphere, with both natural and anthropogenic sources. The only atmospheric sink is the oxidation with OH. The ultimate fate of the complete reaction depends on the concentration of NO_x. The methane oxidation reaction is written as below:

$$OH + CH_4 \longrightarrow H_2O + CH_3 \tag{R7}$$

$$CH_3 + O_2 + M \longrightarrow CH_3O_2 + M \tag{R8}$$

The fate of the CH_3O_2 then depends on whether it is HO_2 or NO_x rich. For a clean (HO_2 rich) environment:

$$CH_3O_2 + HO_2 \longrightarrow O_2 + CH_3OOH \tag{R9}$$

CH_3O_2 reacts with HO_2 and form the water soluble CH_3OOH which washed out at the end. This reaction acts as the sink for HO_x, as well as for O_3 since it is

formed from O_3. For an unclean (NO_x rich) environment:

$$CH_3O_2 + NO \longrightarrow CH_3O + NO_2 \quad \text{(R10)}$$

$$CH_3O + O_2 \longrightarrow HCHO + HO_2 \quad \text{(R11)}$$

CH_3O_2 reacts with NO to form CH_3O and NO_2, which the NO_2 leads to O_3 formation. CH_3O then reacts with O_2 to form HCHO and HO_2. HCHO in the end could again yield HO_2, which further leads to ozone production at the end (discussed below).

Tropospheric ozone

The tropospheric ozone originates from stratosphere-troposphere exchange (STE). It also produces locally in the troposphere, for example via photolysis of NO_2 with oxygen, photolysis or reaction with HCHO from methane oxidation. There is also a small fraction of tropospheric O_3 produced by photolysis of O_2 (R1) at the upper troposphere.

In the troposphere, nitrogen oxides (NO_x) are interconverted via the NO_x null cycle (N3, R2, C3) under the photostationary state and do not affect the NO_x or O_3 budget. In the real atmosphere, the photostationary state is perturbed by the other reactions that oxidize NO to NO_2 (e.g. with HO_2 and with RO_2):

$$NO + HO_2 \longrightarrow NO_2 + OH \quad \text{(R12)} \qquad NO + RO_2 \longrightarrow NO_2 + RO \quad \text{(R13)}$$

The NO_2 then produce O_3 via N3 and R2. One of the most important oxidation mechanisms is the methane oxidation mentioned in section 2.2.2. It forms NO_2 via R10 and produce HO_2 via R11 to form another NO_2 via R12. The product

HCHO also plays a role in ozone production by producing HO_2:

$$\mathrm{HCHO} \xrightarrow{h\nu\,(\lambda \leq 330\ \mathrm{nm})} \mathrm{HCO} + \mathrm{H} \tag{R14}$$

$$\mathrm{HCO} + \mathrm{O_2} \longrightarrow \mathrm{CO} + \mathrm{HO_2} \tag{R15}$$

$$\mathrm{H} + \mathrm{O_2} + \mathrm{M} \longrightarrow \mathrm{HO_2} + \mathrm{M} \tag{R16}$$

$$\overline{\text{Net: } \mathrm{HCHO} + 2\,\mathrm{O_2} \longrightarrow \mathrm{CO} + 2\,\mathrm{HO_2}}$$

CH_3O_2, the precursor of HCHO, is then a good indicator for the O_3 sensitivity, since the formation of HCHO by CH_3O_2 (R10 and R11) acts as the ozone production pathway while the formation of CH_3OOH by HO_2 (R9) leads to the termination of ozone. Details of the indicators are discussed in Section 3.2.

2.3 Radiation

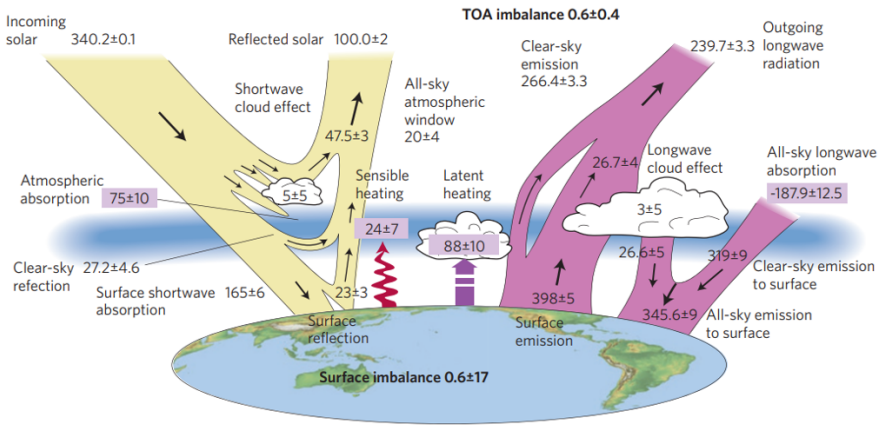

Figure 2.7: Earth radiation budget for the approximate period 2000–2010, showing the energy fluxes and uncertainties within the Earth system, from Stephens et al. (2012)

The Earth's climate is mainly controlled by the Earth's radiation budget. The distribution of the energy determines the thermal conditions, drives the atmospheric and oceanic circulations, and ultimately shapes the Earth's weather and climate. The Earth's radiation balance depends on the incoming solar and outgoing longwave radiation. The Sun is the ultimate source of the incoming solar radiation. It

depends on the Sun's solar activities (Hathaway, 2015; Ball et al., 2014) and the Milankovitch cycles of the Earth's orbit (Milankovitch, 1941; Spiegel et al., 2010). The Sun's solar activity determines how much energy emits from the Sun. It has an 11-year cycle, driven by the changes of its magnetic field (Hathaway, 2015), and is mainly changing the ultraviolet spectrum (Haigh, 2007). The Milankovitch cycles determine the energy received by the Earth. There are three astronomical cycles: eccentricity, obliquity, and precession. Eccentricity describes the changes between circular and more elliptical orbits of the Earth around the Sun. It is with a cycle of around 100000 years. Obliquity refers to the change in the tilting angle of the Earth's rotational axis with respect to the Earth's orbital plane. It ranges from 22.1 to 24.5 degrees with a cycle of 41000 years and is currently 23.5 degrees. Precession describes the changes in the orientation of Earth's rotational axis. It has a 23000-year cycle. The Milankovitch cycles are the dominant drivers of the incoming solar radiation on a geological time scale which induce the glacial and interglacial periods (Imbrie et al., 1992). However, in a climatological time scale, the incoming solar radiation should be relatively stable except for the slight contributions from the changing ultraviolet of the solar activity.

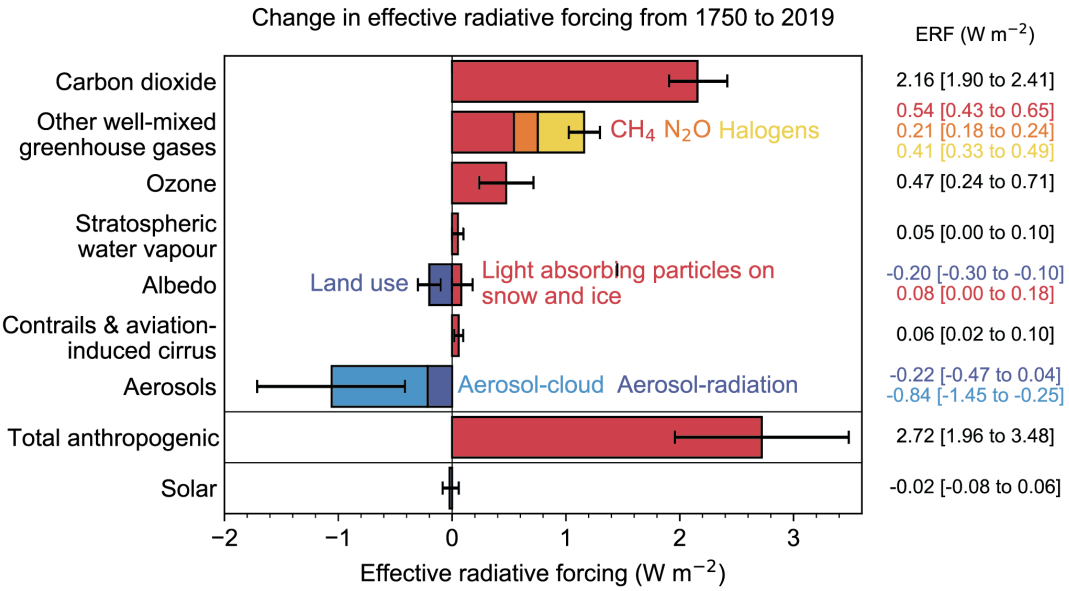

Figure 2.8: Change in effective radiative forcing from 1750 to 2019, from Forster et al. (2021)

The present-day radiation budget is governed more by the state of the atmosphere as well as the surface albedo. The state of the atmosphere, including the atmospheric composition and the clouds. The radiation is absorbed, scattered, and reflected by the gases, aerosols, and clouds in the atmosphere. The amount and distribution of greenhouse gases in the atmosphere determine the atmospheric absorption of shortwave radiation from the Sun and longwave radiation emitted from the surface. According to the recent Sixth Assessment Report of the United Nations Intergovernmental Panel on Climate Change (IPCC AR6; Forster et al., 2021; Figure 2.8), changes in greenhouse gases are the main contributor to the change in radiative forcing, leading to a positive radiative impact. It is mainly contributed by the well-mixed greenhouse gases (CO_2, CH_4, N_2O), ozone and water vapour. The increasing emission of aerosols to the atmosphere is another important contributor to the radiation budget. It leads to a negative radiative impact directly through aerosol-radiation interactions and indirectly through aerosol-cloud interactions. Aerosols could directly scatter and absorb solar and infrared radiation in the atmosphere depending on the aerosol optical depth (Penner et al., 2001). It could also interact with clouds as an additional cloud condensation nuclei (CCN) and ultimately increase the cloud albedo. Clouds could themselves be critical for the Earth's radiation budget, as they are expected to amplify the future warming by the changing altitude and amount of clouds (Forster et al., 2021). Surface albedo plays a significant role as well. It leads to both warming and cooling effects. The change of land use leads to a cooling effect by for example changing a darker forest to a brighter farmland, or the light-absorbing particles on snow and ice darken them and increase the snow melt rate, resulting in a warming effect on the radiation (Forster et al., 2021).

2.4 Modular Earth Submodel System (MESSy)

The Modular Earth Submodel System (MESSy; Jöckel et al., 2005) is a generalized interface structure for Earth System Modeling (ESM) with flexible complexity. It modularized the physical and chemical processes, infrastructures and diagnostic calculations into submodels and allowed coupling with different base models. These submodels are extendable to improve the representation of the ESM. MESSy al-

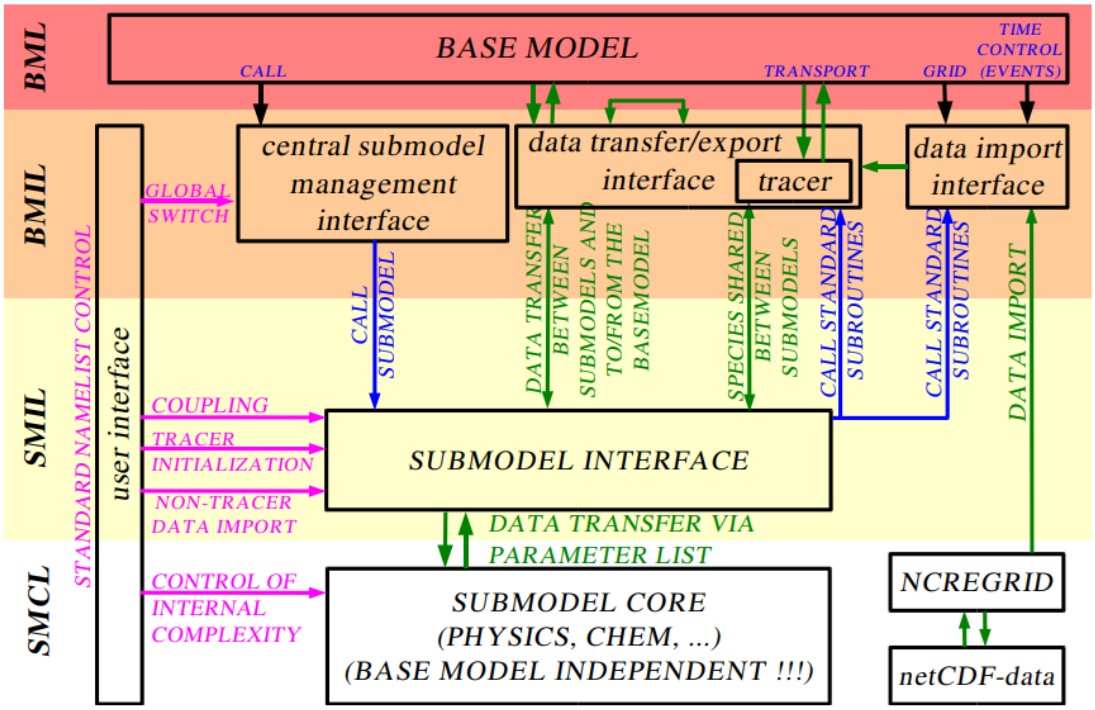

Figure 2.9: MESSy layer structure from Jöckel et al. (2005).

lows flexible model configuration via different combinations of submodels and base models to include various physical and chemical processes using a namelist interface. MESSy connects the base models with the submodels through a four-layer structure:

- Base Model Layer (BML): This layer consists of base models without the modularized components. Currently, the atmospheric general circulation model (AGCM) ECHAM5 (Roeckner et al., 2003), ICON (Giorgetta et al., 2018), numerical weather prediction model COSMO (Baldauf et al., 2011), Lagrangian transport model CLaMS (McKenna et al., 2002) and box model DWARF (Kerkweg et al., 2025) could serve as the base model of MESSy.

- Base Model Interface Layer (BMIL): This layer incorporates three functions: (1) allows the base model to control the submodel by calling and switching them. (2) data transfer between submodels and base models. (3) import of gridded initial and time-dependent boundary conditions.

- Submodel Interface Layer (SMIL): This layer collect the needed data from the BMIL and transfers it to the SMCL, call the SMCL routines and distributes the calculated results of SMCL back to the BMIL. Data exchange between submodels is also managed within this layer.
- Submodel Core Layer (SMCL): This layer includes the core routines of the submodels, which are independent of the base models.

2.4.1 EMAC

EMAC (ECHAM/MESSy Atmospheric Chemistry; Jöckel et al., 2006; Jöckel et al., 2010) is a state-of-the-art climate chemistry model that combines the AGCM ECHAM5 (Roeckner et al., 2003) as the base model with MESSy. In order to simulate the UTLS, a middle-atmosphere configuration of the ECHAM5 model is used (Giorgetta et al., 2006). It consists of 90 vertical hybrid pressure levels reach up to 0.01 hPa. It has been proven to be able to simulate the quasi-biennial oscillation (QBO) and is widely used for UTLS studies.

Quasi Chemistry Transport Model (QCTM)

EMAC can also operate in a Quasi Chemistry Transport Model (QCTM) mode (Deckert et al., 2011). It allows decoupling between the model dynamics with the chemistry in order to operate EMAC as a chemistry transport model (CTM). Operating EMAC in a QCTM mode could better quantify the impacts of a specific process by suppressing the feedback between the dynamics and chemistry. The feedback between dynamics and chemistry in EMAC is established by (1) radiation calculation of the gas-phase greenhouse gases CO_2, CH_4, O_3, N_2O, CFC-11 and CFC-12; and (2) the specific humidity and hydrological cycle influenced by methane oxidation; and (3) the thermodynamic partitioning between stratospheric water vapour, H_2SO_4 and HNO_3. Under the QCTM mode, these feedback mechanisms are decoupled by prescribing the influence parameters from external data, in order to maintain identical model dynamics as the common basis of comparison.

RAD

Radiation in EMAC is calculated by the flexible base-model independent submodel RAD (Dietmüller et al., 2016). RAD is implemented first from the ECHAM5 radiation code but with more flexibility. It calculates the radiation based on the atmospheric composition, including radiatively active gases (CO_2, CH_4, O_3, N_2O, CFC-11 and CFC-12), water vapour, cloud ice and water, aerosol and cloud optical properties and cloud cover. Orbital information is also required. These parameters are either provided online by the base model and other submodels in MESSy or prescribed offline by either importing external datasets or prescribing constant mixing ratios or vertical gradients. The ECHAM5 radiation scheme has 4 spectral bands for shortwave and 16 for longwave radiation. The shortwave bands include 1 for visible + ultraviolet and 3 for near-infrared. The longwave bands include 16 spectral bands covering from far-infrared to near-infrared. RAD also provides an option to calculate multiple diagnostic calls of the radiation within one model time step. The radiative feedback to the dynamics will be provided by the first call. In order to run EMAC in QCTM mode, the first radiation call must be prescribed offline. This feature provides the opportunity to isolate the individual impact of each greenhouse gas by setting each call with only one interactive online species, while the rest remain prescribed offline. A new radiation scheme PSrad (Pincus and Stevens, 2013; Nützel et al., 2024) has also been recently implemented into RAD. PSrad is the radiation scheme employed in ECHAM6 (Stevens et al., 2013) of the Max Planck Institute for Meteorology and ICON (Giorgetta et al., 2018) of Deutscher Wetterdienst. The main difference with the ECHAM5 radiation code is PSrad provides 14 shortwave bands instead of 4. However, PSrad is not used in this work and is beyond the scope of this thesis.

MECCA

In EMAC, chemistry is simulated using the MEECA submodel. MEECA (Module Efficiently Calculating the Chemistry of the Atmosphere; Sander et al., 2005; Sander et al., 2011; Sander et al., 2019) is an multi-purpose atmospheric chemistry submodule in MESSy. It includes comprehensive tropospheric and stratospheric chemistry in both gas and aqueous phase. It includes a wide range of chemi-

cal mechanisms (e.g. HOx, NOx, CH_4, nonmethane volatile organic compounds (NMVOCs), halogens (Cl, Br, I), sulfur and mercury chemistry). MECCA provides flexibility in the selection of chemical mechanisms according to the user's needs. A new tagging feature is available after version 3.0 (Sander et al., 2011). It allows an estimation of the contribution of specific species to the budget of another species within a complex chemical mechanism. For example, MECCA is able to calculate the contributions of ozone by different related species.

2.4.2 Nudging

Nudging, also known as Newtonian relaxation. It is a data assimilation method to adjust the dynamical variables of the AGCM towards the observed state (Jeuken et al., 1996). Nudging provides the foundation for comparing the model output with the observation on a shorter, synoptic time scale. It is done by adding a non-physical relaxation term to the model equations:

$$\frac{\partial X}{\partial t} = F_m(X) + G(X_{obs} - X)$$

X is the prognostic variable, $F_m(X)$ represents all the processes that determine X. $G(X_{obs} - X)$ is the non-physical relaxation term, where G is the relaxation coefficient and $(X_{obs} - X)$ is the difference between the observation and model values. In EMAC, Newtonian relaxation could be applied to prognostic variables, including temperature, surface pressure, divergence and vorticity, and is nudging towards the ECMWF Reanalysis in an hourly (ERA5; Hersbach et al., 2020) or 6-hour (ERA-I; Dee et al., 2011) interval. Depending on the vertical resolution and needs, EMAC could be nudged from the surface to up to 1 hPa.

2.4.3 MECO(n)

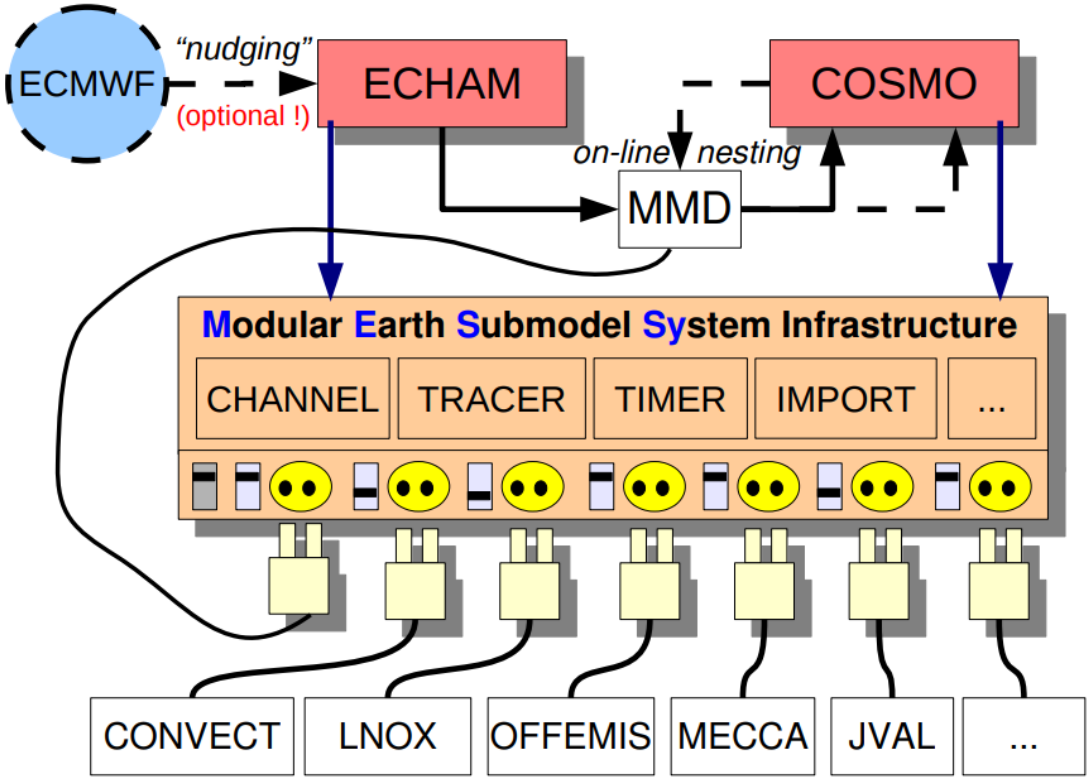

Figure 2.10: Schematic of the concept of the MECO(n) multi-scale climate chemistry model based on MESSy infrastructure from MESSy consortium (2015).

The MECO(n) model is a state-of-the-art multi-scale climate chemistry model based on the MESSy infrastructure. MECO(n) represents MESSy-fied European Centre Hamburg general circulation model (ECHAM) and Consortium for Small-scale Modeling (COSMO) models nested n times. It allows online coupling between the general circulation model ECHAM5 (Roeckner et al., 2003) and the regional atmospheric model COSMO (Baldauf et al., 2011) with both equipped with the MESSy infrastructure as EMAC (Chapter 2.4.1) and COSMO/MESSy (Kerkweg and Jöckel, 2012b). Under this approach, EMAC provides the initial and boundary conditions of COSMO/MESSy and ensures a high degree of consistency on meteorology and chemistry considering that both base models are built under the

MESSy infrastructure. EMAC can be nested with multiple COSMO/MESSy instances; these instances can be further recursively nested. The online nesting is established by the Multi-Model-Driver (MMD; Kerkweg and Jöckel 2012a, Kerkweg et al., 2018). MMD allows either a 1-way or a 2-way exchange of the meteorological and chemical information between the base models.

Table 2.1: Description of submodels in MESSy used in this work.

Submodel	**Function**	**Reference**
AEROPT	Aerosol optical properties	Dietmüller et al. (2016)
AIRSEA	Air-Sea exchange	Pozzer et al. (2006)
ALBEDO	Surface albedo for radiation	Nützel et al. (2024)
BIOBURN	Biomass burning	Kaiser et al. (2012)
CAT	Clear air turbulence	
CH4	Simplified Methane Oxidation	Eichinger et al. (2015)
CLOUD	Cloud cover	Roeckner et al. (2006)
CLOUDOPT	Cloud optical properties	Dietmüller et al. (2016)
CONTRAIL	Contrail cirrus	Burkhardt et al. (2008)
CONVECT	Process of convection	Tost et al. (2006b)
CVTRANS	Convective transport of tracers	Tost et al. (2010)
DDEP	Dry deposition	Kerkweg et al. (2006a)
DRADON	Emission and decay of 222-Rn	Jöckel et al. (2010)
E5VDIFF	ECHAM5 vertical diffusion	Roeckner et al. (2003)
EC2COSMO	Transform EMAC data into COSMO format	Kerkweg and Jöckel (2012b)
GWAVE	Gravity waves	Hines (1997)
H2O	Create H_2O tracer for EMAC	Deckert et al. (2011)
IMORT	Import data from external files	Kerkweg and Jöckel (2015)
JVAL	Calculation of the J values	Sander et al. (2014)
LNOX	Lighting NOx	Tost et al. (2007)
MECCA	Tropospheric & stratospheric chemistry	Sander et al. (2019)
MMD2WAY	Coupling of MECO(n) model instances	Kerkweg et al. (2018)
MSBM	Heterogeneous reaction rates on PSC	Jöckel et al. (2010)
O3ORIG	Origin of ozone	Grewe (2006)
OFFEMIS	Offline emissions	Kerkweg et al. (2006b)
ONEMIS	Online emissions	Kerkweg et al. (2006b)
ORBIT	Orbital parameters	Dietmüller et al. (2016)
OROGW	Orographic gravity wave	Roeckner et al. (2003)
PTRAC	Prognostic Tracers	Jöckel et al. (2008)
PTRACINI	Prognostic tracer initialisation	
QBO	Newtonian relaxation of quasi-biennial oscillation	Jöckel et al. (2016)
RAD	Radiation calculation	Dietmüller et al. (2016)
S4D	4D sampling	Jöckel et al. (2010)
SATSIMS	Satellite simulator	Klein et al. (2013)
SCAV	Scavenging	Tost et al. (2006a)
SCOUT	Stationary Column Output	Jöckel et al. (2010)
SEDI	Aerosol sedimentation	Kerkweg et al. (2006a)
SORBIT	sun-synchronous satellite orbits	Jöckel et al. (2010)
SURFACE	Surface processes	Roeckner et al. (2003)
TENDENCY	Trace process-based tendencies	Eichinger and Jöckel (2014)
TNUDGE	Tracer nudging	Kerkweg et al. (2006b)
TREXP	Tracer release experiments from point sources	Jöckel et al. (2010)
TROPOP	Tropopause	
VERTEX	Vertical diffusion	
VISO	Vertically layered iso-surfaces	Jöckel et al. (2010)

3 Results

3.1 Simulated mixing in the UTLS by small-scale turbulence using multi-scale chemistry-climate model MECO(n)

This chapter has been published in the journal Atmospheric Chemistry and Physics as a research article. I am the first author of this paper, where I designed and performed the simulations, analysed the data, generated the figures and wrote the manuscript. The co-authors contributed to discussing the results and proofreading the manuscript. Detailed author contributions can be found at the end of the paper in the section Author contributions.

How to cite: Chau, C. H., Hoor, P., and Tost, H.: Simulated mixing in the UTLS by small-scale turbulence using multi-scale chemistry-climate model MECO(n), Atmospheric Chemistry and Physics, 25, 13 123–13 140, https://doi.org/10.5194/acp-25-13123-2025, 2025b.

Submitted: 06 December 2024
Published: 21 October 2025

Atmos. Chem. Phys., 25, 13123–13140, 2025
https://doi.org/10.5194/acp-25-13123-2025

Atmospheric Chemistry and Physics
Open Access
EGU

Simulated mixing in the UTLS by small-scale turbulence using multi-scale chemistry-climate model MECO(n)

Chun Hang Chau, Peter Hoor, and Holger Tost

Institute for Atmospheric Physics, Johannes Gutenberg University Mainz, Mainz, Germany

Correspondence: Chun Hang Chau (cchau@uni-mainz.de) and Holger Tost (tosth@uni-mainz.de)

Received: 6 December 2024 – Discussion started: 20 December 2024
Revised: 30 August 2025 – Accepted: 1 September 2025 – Published: 21 October 2025

Abstract. The chemical composition of the upper troposphere and lower stratosphere (UTLS) plays an important role for the climate by affecting the radiation budget. Small-scale diabatic mixing like turbulence has a significant impact on the distribution of tracers which further affect the energy budget via their radiative impact. Current models usually have a higher vertical resolution near the surface and a coarser grid spacing in the free atmosphere, which is insufficient to resolve the occurrence of small-scale turbulence in the UTLS. In this work, we utilise enhanced vertical resolution (200 m in the UTLS) simulations focusing on mixing events in the Scandinavian region using the state-of-the-art multi-scale atmospheric chemistry model system MECO(n). These model simulations are able to represent different distinct turbulent mixing events in the UTLS and depict a significant impact of mixing on the tracer distribution in the UTLS. A novel diagnostic (delta tracer–tracer correlation) is introduced to determine the direction of the vertical mixing. The strength of the UTLS turbulent mixing depends on the particular situation, i.e., the vertical tracer gradient, and dynamical and thermodynamical forcing, i.e., vertical wind shear, deformation and static stability. This work provides evidence that high-resolution simulations are able to represent significant turbulent mixing in the UTLS region, allowing for further research on the UTLS turbulent mixing and its implications for the climate system.

1 Introduction

The upper troposphere and lower stratosphere (UTLS) is defined as the region around the tropopause which acts as a transition layer between the troposphere and stratosphere (Gettelman et al., 2011). The troposphere and stratosphere are fundamentally different in chemical composition and static stability, and they are separated by the tropopause, an immaterial surface acting as a vertical transport barrier. The dynamical tropopause (also known as the potential vorticity (PV) tropopause) is one of the commonly used definitions for the tropopause due to its conservation under isentropic conditions. The typical PV values for the dynamical tropopause can range from 1.6 PVU to 3.5 PVU, but 2 PVU is most commonly used (Stohl et al., 2003a). Since the PV tropopause is a quasi-impermeable surface for adiabatic frictionless flow, i.e., on isentropes, stratosphere–troposphere exchange (STE) across the tropopause may require diabatic processes, e.g., like turbulent mixing by small-scale turbulence (Holton et al., 1995).

The distribution of chemical constituents and the resulting changes in the UTLS chemistry are a consequence of the complex atmospheric processes on various spatial and temporal scales (Riese et al., 2012). Bidirectional STE is one of the crucial processes affecting the chemistry of UTLS (Holton et al., 1995; Stohl et al., 2003b), especially in the extratropical transition layer (ExTL) in the extratropics (Gettelman et al., 2011).

The chemical composition of the UTLS plays an important role on the climate by affecting the radiation budget (Forster et al., 2021). Local changes in the tracer distribution in the UTLS will not only lead to local changes on the energy budget but also affect the surface climate (Riese et al., 2012; Lacis et al., 1990; Randel et al., 2007). Previous studies showed that the surface temperature is highly sensitive to the changing chemical composition in the UTLS region (Forster

and Shine, 1999, 2002). For example, changes in ozone distribution especially at the tropopause and lower stratosphere could have large impacts on the surface temperature (Forster and Shine, 1997). Besides the radiation budget, STE also has impacts on other aspects, such as stratospheric ozone recovery (Butchart and Scaife, 2001) and the tropospheric ozone budget (Lelieveld and Dentener, 2000).

Turbulent mixing is one of the processes of STE (Holton et al., 1995), especially in the region near the jet streams and tropopause folds (Shapiro, 1980). Clear air turbulence (CAT) is one of the major types of turbulence that occurs in the UTLS which could lead to rapid mixing of chemical species between stratosphere and troposphere (Esler and Polvani, 2004; Traub and Lelieveld, 2003). CAT refers to the turbulence in the free atmosphere that occurs in cloud-free regions or within stratiform clouds (Ellrod et al., 2003). It has a lifetime of 1 h to 1 d, with a typical vertical dimension from 500 to 1000 m (Overeem, 2002). Kelvin–Helmholtz instability (KHI) as a result of vertical shear of horizontal wind (Kunkel et al., 2019), forming a shear layer at the tropopause (Kaluza et al., 2021), is the major mechanism that leads to CAT formation (Watkins and Browning, 1973; Ellrod and Knapp, 1992). Consequently, CAT occurs when the vertical wind shear is strong enough to overcome the stable layer's inhibition (Williams and Joshi, 2013).

CAT occurs most frequently in the UTLS, especially near the tropopause (Dutton and Panofsky, 1970; Wolff and Sharman, 2008) and along the jet streams (Keller, 1990; Traub and Lelieveld, 2003). This phenomenon shows the highest probability of occurrence in boreal winter and is less frequent in boreal summer (Jaeger and Sprenger, 2007). An exceptional region is the eastern Mediterranean (Jaeger and Sprenger, 2007; Traub and Lelieveld, 2003) which is also known as a region with strong STE (Sprenger and Wernli, 2003).

Climate change is expected to increase the occurrence and intensity of CAT due to the strengthening of vertical wind shear (Williams, 2017), such that CAT is expected to have a large relative increase globally under the IPCC RCP 8.5 scenario, especially at the mid-latitudes (Storer et al., 2017). Williams and Joshi (2013) results suggested that if the atmospheric CO2 is doubled compared to the pre-industrial time, the strength of CAT in the North Atlantic during winter will increase by 10 %–40 % and the occurrence of CAT which is moderate or greater will increase by 40 %–170 %. Recent studies by Smith et al. (2023) and Hu et al. (2021) also show similar results over the North Atlantic and East Asia, respectively.

Considering the increasing trend of CAT, the link between turbulent mixing and STE, and hence the radiation budget, it is crucial to investigate the relation between CAT and mixing of chemicals in the UTLS. However, previous studies mainly focus on the dynamical aspect of turbulence (Kaluza et al., 2021; Muñoz-Esparza et al., 2020), but not on tracers. The main objective of this study is not to analyze the representation and strength of the turbulence itself but to systematically analyze the impact of turbulence on tracer mixing in the UTLS. For that purpose, a novel diagnostic, i.e., the delta tracer–tracer correlation is used within the multi-scale climate chemistry model MECO(n). Consequently, the main objective of the study is on the resulting effects on the tracer distributions caused by turbulent mixing. Note to differentiate between the mixing itself, i.e., the "dynamical" mixing represented by e.g., the turbulent kinetic energy (TKE), and the local effects on the tracer distributions provided by the mixing and the tracer gradient and further effects of the mixing, i.e., the downwind changes in the tracer distributions, originating from the mixing and subsequent processes, e.g., advection. The latter especially can further enhance vertical differences in tracer concentrations in the case of modified vertical gradients of the respective tracers.

The paper is structured as outlined below. Section 2 introduces the applied model, describes the model configuration and the novel diagnostic delta tracer–tracer correlation. Section 3 presents the results and discusses the details of the mixing by passive tracer tests conducted in this study. Section 4 summarizes the findings and draws conclusions.

2 Model description and methodology

This section gives a brief introduction to MECO(n) (Mertens et al., 2016), the EMAC and Consortium for Small-scale Modeling (COSMO) setup (including horizontal and vertical resolution, model domain and time step), the COSMO turbulence scheme, the explanation of the enhanced vertical grid for COSMO and the introduction of the novel diagnostic delta tracer–tracer correlation.

2.1 MECO(n) modeling system (v2.55.2)

MECO(n) represents the MESSy-fied (Modular Earth Submodel System, MESSy) European Centre Hamburg general circulation model (ECHAM) and COSMO models nested *n* times (Kerkweg and Jöckel, 2012a; Kerkweg et al., 2018), and is a state-of-the-art online coupled global/regional atmospheric chemistry model system based on the Modular Earth Submodel System (MESSy; Jöckel et al., 2005), which allows users to switch on or off physical and chemical processes through namelist interfaces. In MECO(n), the regional atmospheric model COSMO (Baldauf et al., 2011; Doms and Baldauf, 2018; Schättler et al., 2021) is nested online within the global general circulation model ECHAM5 (Roeckner et al., 2003); both COSMO and ECHAM5 are equipped with the MESSy infrastructure as individual COSMO/MESSy (Kerkweg and Jöckel, 2012b) and ECHAM/MESSy instances (EMAC; Jöckel et al., 2006, 2010). Besides the meteorological data, also the chemical composition and tracer information is exchanged between the individual instances. MECO(n) consequently allows an online coupling between different models so that the larger-scale (parent, e.g., EMAC

or COSMO/MESSy) instance can provide the initial and boundary conditions for the smaller-scale (children, e.g., COSMO/MESSy) instances.

2.2 MECO(n) model configuration

In this study, MECO(n) contains two smaller nests besides the global instance: EMAC is coupled with an intermediate COSMO/MESSy instance (further denoted as CM40) and CM40 is further coupled with a target COSMO/MESSy instance (further denoted as CM10). EMAC is operated in T42L90MA (Giorgetta et al., 2006) resolution. It is a middle-atmosphere configuration that has 90 vertical layers up to 0.01 hPa (approximately 80 km in altitude) at T42 horizontal resolution (approximately $2.8° \times 2.8°$ at the equator). The model time step is 360 s and it is initialized with the ERA-Interim reanalysis data (Dee et al., 2011). EMAC has been weakly nudged (Jeuken et al., 1996) towards the ERA-Interim reanalysis data up to 10 hPa. The CM40 domain covers most of Europe from Spain and Iceland in the west to parts of Russia in the east with a horizontal resolution of 0.4° and a model time step of 120 s. The initial and boundary data are provided by the EMAC instance. The CM10 model region focuses on the Scandinavian region with a horizontal resolution of 0.1° and a model time step of 40 s. The initial and boundary data are provided by the CM40 instance. Both CM40 and CM10 have 84 vertical layers with an enhanced resolution in the UTLS, details of the enhanced grid are discussed in Sect. 2.4.

2.3 Vertical mixing in COSMO

The mixing in the COSMO model is divided into two parts: (1) small-scale turbulent diffusion, and (2) organized moist convection. In this study, we focus on the impact of the small-scale turbulent diffusion. In COSMO, the subgrid-scale turbulent diffusion is based on K-theory, the constitutive equation is as follows:

$$F_\psi = -K_\psi \cdot \nabla\psi. \tag{1}$$

This equation relates the subgrid-scale turbulent flux of a scalar quantity F_ψ to the gradient of ψ and a diffusion coefficient K_ψ. The determination of the K_ψ depends on the chosen turbulent closure scheme. COSMO provides two different turbulent schemes. The default setup uses a 1-D diagnostic closure scheme by Muller (1981). In this scheme, K_ψ is determined by the Blackadar length scale (Blackadar, 1962), vertical wind shear, Brunt–Väisälä frequency and stability functions which are based on the flux-Richardson number. However, this scheme comes with several drawbacks including insufficient vertical mixing in stable stratification. COSMO also provides another newer turbulent scheme based on prognostic turbulent kinetic energy. The K_ψ in this prognostic TKE-based scheme is in the forms

$$K^{\mathrm{H}} = q\lambda S^{\mathrm{H}}, \tag{2}$$

$$K^{\mathrm{M}} = q\lambda S^{\mathrm{M}}, \tag{3}$$

where K^{H} and K^{M} are the turbulent diffusion coefficients for heat and momentum respectively. They are computed by the corresponding stability functions for scalars (S^{H}) and for momentum (S^{M}) which are determined by the flux-Richardson number, the turbulent length scale λ (which is assumed to be the Blackadar mixing length) and the turbulent velocity scale $q = \sqrt{2\overline{e_t}}$, where $\overline{e_t}$ is the TKE. The latter scheme is used in this study. Details for the turbulent schemes can be found in Sect. 3 (Sect. 3.3.2 for the used scheme) of the COSMO model documentation by Doms et al. (2018).

2.4 Enhanced vertical grid for COSMO instances

The default vertical grid for COSMO is either 40 or 50 levels that reach up to 22 km, with an 11 km damping layer starting at 11 km. Furthermore, these default vertical grids have a finer resolution near the surface and a coarser resolution in the free atmosphere, which makes the default setup too low and too coarse for resolving small-scale turbulence or other processes in the UTLS. Previous studies also show that STE-related processes are sensitive to the model resolution (Miyazaki et al., 2010; Meloen et al., 2003; van Velthoven and Kelder, 1996). In MECO(n), the model TKE is sensitive to the vertical resolution and the mixing strength is sensitive to both horizontal and vertical resolution (details in the Supplement). Therefore, in this study, we introduce an enhanced vertical grid focused on the UTLS which is applied to both CM40 and CM10. It is modified from an established extended vertical grid (Eckstein et al., 2015) with 60 levels (further denoted as EX-60) which reaches the lower stratosphere up to 33 km, with a 5 km damping layer starting at 27 km. Our enhanced setting has 84 levels and also reaches up to 33 km, with an identical 5 km damping layer starting at 27 km considering that Eckstein et al. (2015) show that the differences between 5 and 11 km damping layers are marginally small, and the analysis carried out in this study are far below the damping layer with more than 20 model levels, the potential reflection from the model top should be negligible. In order to reduce modifications of the boundary layer due to the change of vertical grid, we kept the levels below 8 km unchanged and only increase the resolution between 8 and 15 km to 200 m per level considering the typical size of CAT (Overeem, 2002). The level definition for the default 40 levels (further denoted as D-40), 50 levels (further denoted as D-50), EX-60 and the enhanced vertical grid (further denoted as EH-84) are shown in Fig. 2. EH-84 is evaluated with ERA5 data as well as comparisons with the tested EX-60 setup.

EH-84 is able to simulate the atmosphere reasonably. Although there is some discrepancy, the temperature pattern from ERA5 is generally well produced by the model as well as the relative humidity. There is a systematic cold bias in the CM10 output. However, the systematic cold bias that occurs in EH-84 is also found in EX-60 as well as the CM40

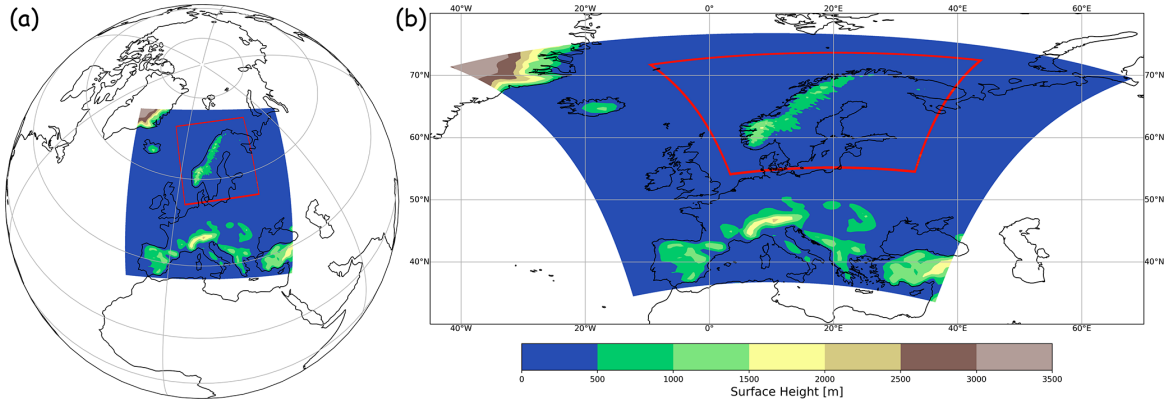

Figure 1. Model domain for MECO(n) with surface height: **(a)** an overview and **(b)** a close-up for CM40 and CM10.

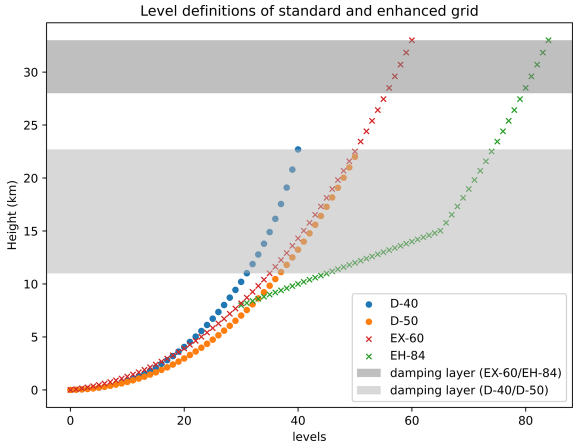

Figure 2. The vertical level definition of D-40, D-50, EX-60 and EH-84 vertical grid, the shaded area represents the damping layer of the respective vertical grid.

and EMAC output, indicating that the occurrence of the cold bias is not a result of the increased vertical resolution in the UTLS. There is a strong alignment of the main meteorological parameters between the EH-84 and EX-60 output, and the latter is well evaluated against observations (Eckstein et al., 2015). Consequently, the model output from the enhanced vertical grid EH-84 can be seen as reliable and suitable for the needs of this study. Details of the evaluation of EH-84 can be found in the Supplement. Furthermore, a sensitivity study was conducted in the Supplement to show the necessity of higher vertical and horizontal resolution. The occurrence of high TKE values in EH-84 is more frequent than in EX60 (Fig. S9), hence the mixing is more frequent (Figs. 8 and S11). CM10 (Fig. 8) also shows more efficient mixing than CM40 (Fig. S12) despite the similar TKE frequency.

2.5 Delta tracer–tracer correlation

In order to investigate the tracer mixing in the UTLS, we introduced a novel diagnostic, namely a delta tracer–tracer correlation, which is a similar concept to the tracer–tracer correlation, but makes use of the model capabilities. While the tracer–tracer correlation can be compared to the real world, the delta tracer–tracer correlation is a correlation between the differences of the tracers from model experiments. Instead of showing the mixing as an accumulation affected by other processes, it shows the impact of a single process (and potential subsequent advection differences). It requires two pairs of tracers (one pair of stratospheric and one pair of tropospheric). The difference of each pair, is a particular process being deactivated on one of the tracers in the model to investigate the impact of it. In our study, it is the turbulent vertical diffusion (vdiff). The detailed released tracers are described in Sect. 3.2. The delta tracer–tracer correlation can also be used to determine the direction of vertical mixing. Several distributions are expected for different scenarios: (1) concentrated distribution at the center [0,0] if no vertical mixing takes place at all; (2) diagonal distribution for bidirectional mixing, where both tracers change at a similar rate, causing the data point spread along the diagonal. The bidirectional mixing could be either balanced or imbalanced, meaning an even (case 1, spread equally from the center [0,0]) or uneven (case 2, spread unequally from the center [0,0]) spread along the diagonal. Balanced bidirectional mixing indicates a similar amount of stratospheric tracers being exchanged with the tropospheric tracers, while imbalanced bidirectional mixing indicates a different amount of stratospheric tracers being exchanged with the tropospheric tracers. It could be attributed to different situations, details are discussed in the following cases. The upper left section of the diagram indicates the downward mixing of stratospheric tracers into the troposphere since at the same grid, there are increasing stratospheric tracers and decreasing tropospheric tracers. And the

lower right quadrant indicates the opposite, with decreasing stratospheric tracers and increasing tropospheric tracers, i.e., upward mixing of the tropospheric tracers. Scatter further away from the center indicates irreversible mixing, as the composition of the air masses is substantially modified, and the tracer is mixed irreversibly into the grid, i.e., instantaneously horizontally mixed. Additionally, this scatter is caused by initial differences from the mixing which are then amplified by (mostly horizontal) advection into regions where the vertical gradient of the tracers are different. Those different gradients can originate both from the tracer mixing event itself further upstream or from specific meteorological conditions, e.g., tropopause folds with strong gradients. Scatter away from the diagonal (case 3) indicates that the mixing occurs in a region with a different tracer gradient, a non-local effect introduced by other processes like horizontal advection acted on the mixed tracer. The scatter away from the diagonal gives an indication that the mixing is non-local, but the strength of mixing itself is still solely contributed by the turbulent mixing.

3 Results and discussion

3.1 Turbulence in the UTLS

Considering that turbulence in EMAC is dampened in the free atmosphere due to its hydrostatic characteristic and the formulation of the turbulence scheme (designed for the boundary layer only), this section analyzes how well the COSMO instances are able to represent turbulence and associated mixing. Therefore, the model TKE is compared with a calculated turbulence index using the grid-scale wind data from COSMO, i.e., the turbulence diagnostic TI1 from Ellrod and Knapp (1992), which includes a vertical wind shear term and a deformation (stretching and shearing) term to examine whether the highly parameterized subgrid-scale turbulence scheme is consistent with the grid-scale wind. The calculated TI1 is divided into five categories (i.e., null, light, moderate, severe and extreme) according to the thresholds set by Sharman et al. (2006). The features of the turbulence including the distribution and relative strength are reproduced by the COSMO instance as can be seen in Figs. 3 and 4, which shows the calculated TI1 (Fig. 3) and model TKE (Fig. 4) on the selected vertical levels, respectively. The TI1 generally agrees with TKE in terms of distribution and relative strength. The discrepancy between them might be caused by the neglected mechanisms of the Ellrod index or other subgrid-scale processes that could potentially lead to the formation of turbulence in the UTLS, e.g., subgrid-scale gravity waves. The high TKE and Ellrod index shown in Figs. 3 and 4 is caused by the jet stream as shown in Fig. S18. The increased shear could be attributed to the higher vertical and horizontal resolution, as shown in Fig. S19. CM10 shows a finer structure and hence more shear. It is important to note that the Ellrod index does not fully represent the turbulence in the atmosphere since it does not account for all producing mechanisms. For example TI1 might neglect the shear related to anticyclonic flow (Ellrod and Knox, 2010). It is also important to note that the comparison between the TI1 and TKE is not sufficient enough considering both of them are calculated from the COSMO wind field; comparison with observation should be conducted when there is available data. In addition, the strength between TI1 and TKE is not directly comparable since the TI1 threshold was set according to the verbal report of pilots and is subjective to the pilot's feelings and there is no similar threshold available for TKE. However, the results at least show consistency in the distribution on different levels. To conclude, the model grid-scale wind field is consistent with the model turbulence scheme and can detect the occurrence of turbulence in the model.

We also compare the model results with the last flight in the GW-LCYCLE II campaign (Witschas et al., 2023) on 1 February in northern Scandinavia. We derive a measure of turbulence from the high-frequency measured N_2O (Lachnitt et al., 2023) and link it with the model TKE. We computed a 31-point running standard deviation normalized with the variability of the window for N_2O. The running standard deviation shows the N_2O fluctuation from the background in a short period of time, while the normalization eliminates the effect of a tracer gradient due to the changing flight altitude or large-scale exchange of air masses. Figure 5 shows the model TKE at the flight time with the normalized running standard deviation of the measured N_2O. It shows that the derived turbulence signal often coincides well with the simulated TKE (Fig. 5a), the stronger signals (higher percentiles, Fig. 5b) coincide with the higher model TKE as well. This indicates that there is a reasonable degree of consistency between the derived turbulence signal from the measured N_2O with the simulated turbulence.

3.2 Passive tracer test

In order to investigate the ability of mixing by turbulence in MECO(n), a series of passive tracer tests is performed by initializing several pairs of passive tracers in the simulation via the MESSy submodel PTRAC (Jöckel et al., 2008). The PTRAC submodel allows users to define the physical and chemical properties of specific tracers. In this study, we define a total of four pairs of artificial passive tracers with different distributions and slightly different physical properties. For the same pair of tracers, the only difference is whether the physical process of vertical diffusion (vdiff) is turned on or off. The vertical diffusion was switched off at the very beginning. An O_3-like tracer with a relatively steep linear gradient and a N_2O-like tracer with a relatively gentle gradient are initialized to investigate the effect of the tracer gradient on the strength of mixing under a relatively realistic scenario. The tracers change linearly at the transition layer near the tropopause between approximately 300 and 100 hPa. The initial condition of the tracers is shown in Fig. S20 as a ver-

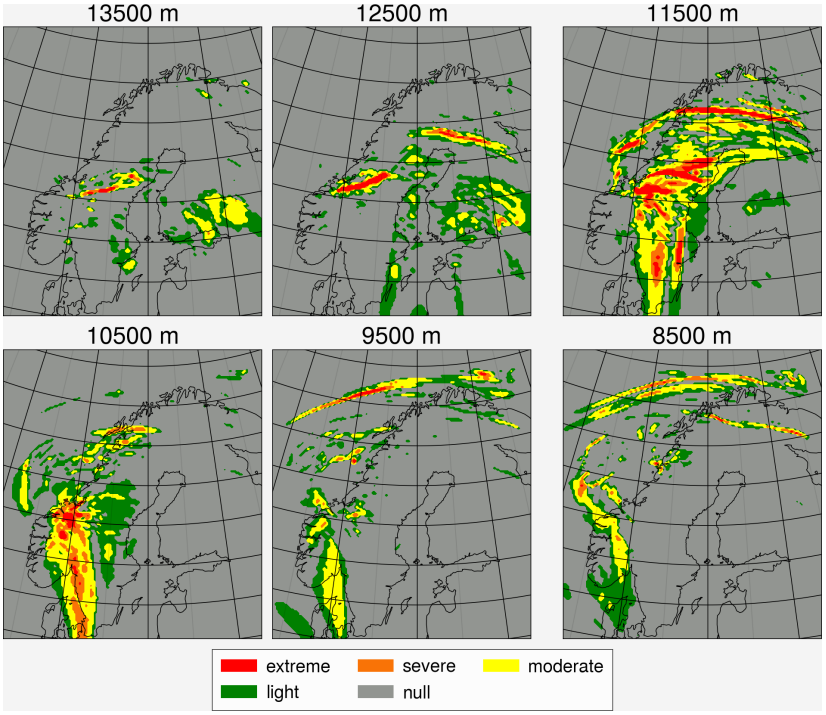

Figure 3. Calculated turbulence index (TI1) on 7 February 2016 at 20:00 UTC: null: grey, green: light, yellow: moderate, orange: severe, red: extreme.

Table 1. Summary of the released passive tracers.

Pair no.	Tracer	vdiff (on/off)	Mixing ratio [mol mol^{-1}]	Stratospheric/tropospheric
1	O_3-like	on	2.4×10^{-8} to 4.0×10^{-6}	Stratospheric
1	O_3-like	off	2.4×10^{-8} to 4.0×10^{-6}	Stratospheric
2	N_2O-like	on	3.2×10^{-7} to 6.4×10^{-8}	Tropospheric
2	N_2O-like	off	3.2×10^{-7} to 6.4×10^{-8}	Tropospheric
3	Inverted O_3-like	on	4.0×10^{-6} to 2.4×10^{-8}	Tropospheric
3	Inverted O_3-like	off	4.0×10^{-6} to 2.4×10^{-8}	Tropospheric
4	Inverted N_2O-like	on	6.4×10^{-8} to 3.2×10^{-7}	Stratospheric
4	Inverted N_2O-like	off	6.4×10^{-8} to 3.2×10^{-7}	Stratospheric

tical profile. In order to investigate the direction of mixing, inverted versions of both tracers are also released in order to have stratospheric and tropospheric tracers with a similar gradient at the same time. A summary of the tracers is shown in Table 1.

3.3 Results: case studies

3.3.1 Case 1: turbulence induced balanced bidirectional mixing in a stable region

Case 1 (Fig. 6) is located within a typical high-level ridge trough system over Europe in the transition region between the anticyclonic ridge and the cyclonic trough, with the potential for strong wind shear and convergence. It is also associated with the jet stream, regions with relatively low *Ri* are found at the vicinity of the tropopause and the core of the jet stream (Fig. 7).

Figure 8 shows the cross section of the distribution (top) and differences (bottom; vdiff on – vdiff off) for the O_3-like (right) and inverted O_3-like (left) tracers. The results show that vertical turbulent diffusion has a significant impact on the tracers. For the tropospheric inverted O_3-like tracers, a higher mixing ratio above the tropopause and a lower mixing ratio below the tropopause is simulated when vertical turbu-

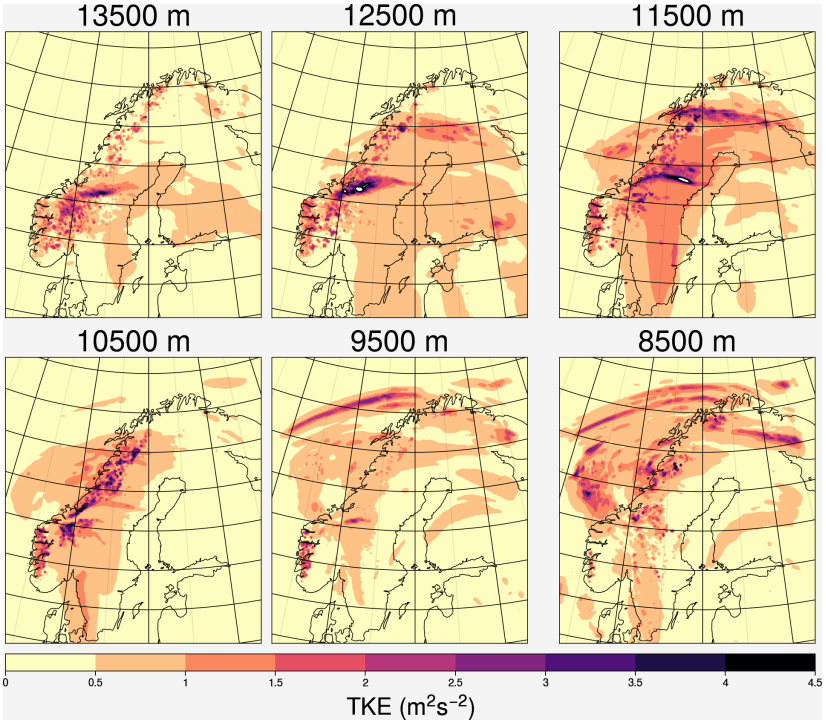

Figure 4. Model turbulence kinetic energy (TKE) on 7 February 2016 at 20:00 UTC.

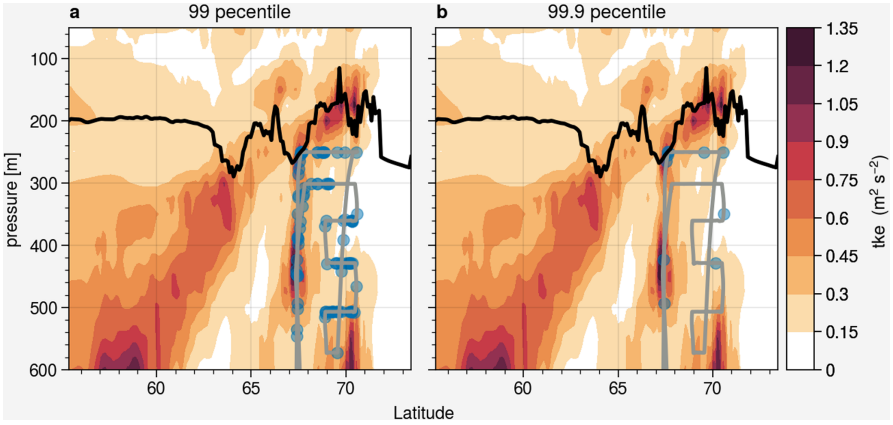

Figure 5. Cross section of average model TKE during the flight time. The black line represents the PV tropopause, the grey line represents the flight track, and the scatters represent the **(a)** 99th percentile and **(b)** 99.9th percentile of the normalized running standard deviation, i.e., the regions where the N_2O shows high normalized variability, potentially due to turbulence.

lent diffusion is present. This indicates that the tracers were transported across the tropopause by turbulent mixing from the troposphere to the stratosphere. The stratospheric O_3-like tracer shows analogous behavior but in an inverse manner, in which the turbulent mixing shifts the tracers from the stratosphere into the troposphere. By comparing the differences with the background mixing ratio, vertical mixing could lead to almost 10 % of differences near the tropopause. Similar mixing behavior is also noticeable for the N_2O-like and inverted N_2O-like tracers but in a weaker form (approximately 5 %) due to its relatively gentle gradient (Fig. S8). Note that the tracer differences are strongest, exactly in the region with

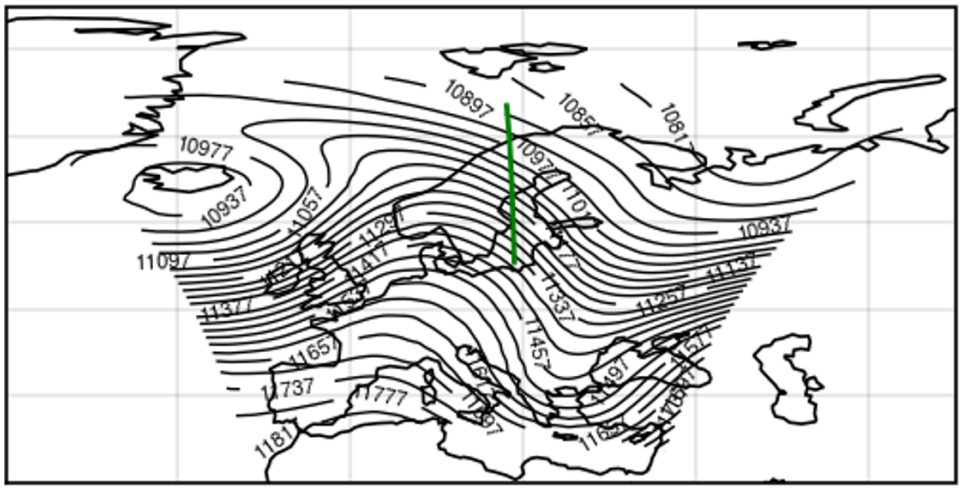

Figure 6. Case 1: geopotential height (gpm) at 200 hPa from CM40 on 5 February 2016 at 18:00 UTC. Green line indicates the location of the selected cross section of case 1.

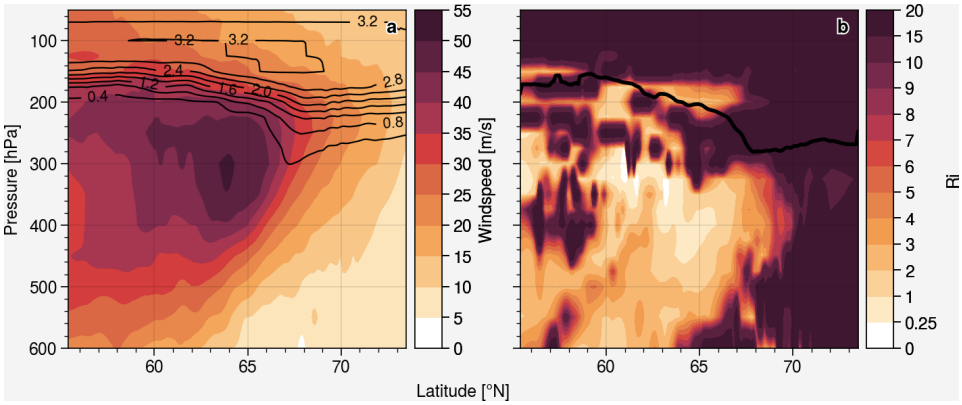

Figure 7. Case 1: **(a)** CM10 horizontal wind speed, the black contour line show the O_3-like tracer and **(b)** gradient Richardson number (*Ri*), the black line indicates the PV tropopause.

the lowest gradient Richardson number (cf. Figs. 7b and 8c, d), indicating turbulence as the origin of the high spatial correlation.

Figure 9 shows the tracer–tracer correlation for different pairs of passive tracers at the same time and location as the cross section of Fig. 8. Figure 9a and b show a tracer–tracer correlation between the O_3-like stratospheric tracer and N_2O-like tropospheric tracer with and without vertical diffusion respectively. Considering the passive tracers were released with a linear gradient, the tracer–tracer correlation shows a linear distribution as well, unlike the other classic tracer–tracer correlation which normally has an exponential relationship. Perfect correlation with diagonal distribution is expected if vertical diffusion does not play any role in transporting the tracer. Considering the magnitudes of the mixing ratio in both tracers, the difference is hard to distinguish for a single mixing event of Fig. 8 in the tracer–tracer correlation. Therefore, the tracer–tracer correlation of the same tracer with and without vertical diffusion was performed as well. Figure 9c and d show the correlation with and without vertical diffusion for the stratospheric O_3-like and tropospheric N_2O-like tracer respectively. Both tracers show some dispersion from the diagonal, indicating that vertical diffusion is affecting the tracers, leading to a deviation from perfect correlation. In addition, a delta tracer–tracer correlation (see Fig. 2.5 for an explanation of this diagram) is performed for O_3-like and N_2O-like tracers.

Figure 10 shows the color-coded delta tracer–tracer correlation for the stratospheric O_3-like/inverted tropospheric O_3-like tracers of the mixing event on 5 February 2016 at

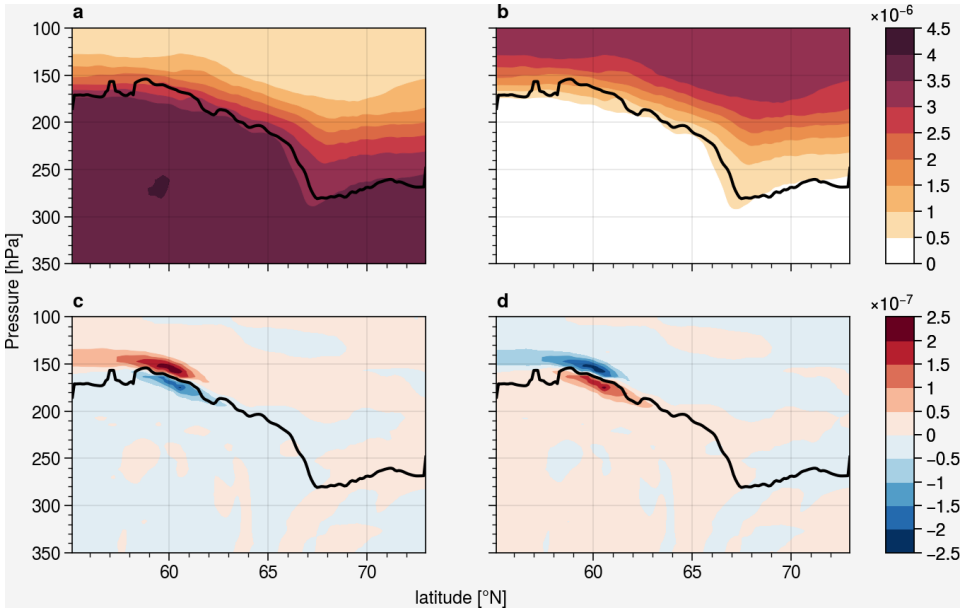

Figure 8. Cross section of the distribution: **(a)** inverted O_3-like tracers (mol mol^{-1}), **(b)** O_3-like tracers (mol mol^{-1}); and **(c)** difference (vdiff on – off) of the inverted O_3-like tracers (mol mol^{-1}), **(d)** difference of the O_3-like tracers (mol mol^{-1}) on 5 February 2016 at 18:00 UTC. The black line indicates the PV tropopause.

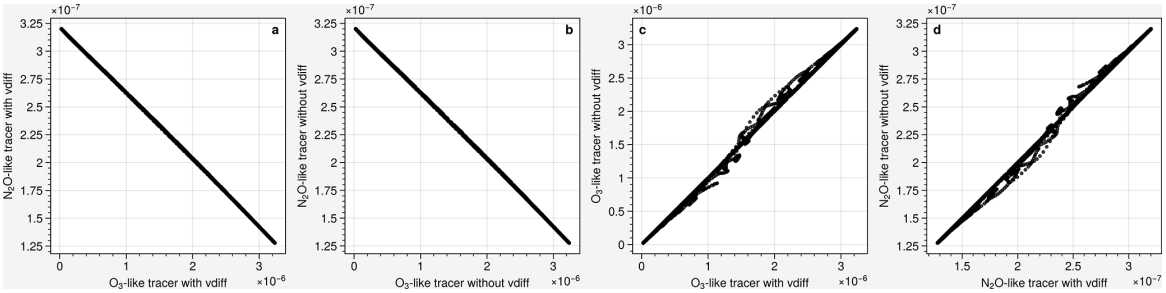

Figure 9. tracer–tracer correlation for **(a)** O_3-like/N_2O-like tracers with vdiff (mol mol^{-1}); **(b)** O_3-like/N_2O-like tracers without vdiff (mol mol^{-1}); **(c)** O_3-like tracers with/without vdiff (mol mol^{-1}), **(d)** N_2O-like tracers with/without vdiff (mol mol^{-1}) on 5 February 2016 at 18:00 UTC.

18:00 UTC (Fig. 8). It is conducted using every grid point between 100 and 350 hPa at the indicated location on Fig. 6. It is a bidirectional mixing event associated with turbulence, which shows a diagonal distribution, indicating that at a specific location, the change of stratospheric tracer is similar to the change of tropospheric tracer. The symmetric distribution indicates that the mixing is balanced in strength in both directions. The strong downward mixing of the stratospheric air is caused by vertical wind shear or/and deformation: the region with strong downward mixing is concurrently the region with extreme turbulence according to the Ellrod index, as well as the strong vertical wind shear (VWS), deformation and relatively high TKE values. Considering that the vertical wind shear and deformation are the key mechanisms for turbulence formation, and vertical wind shear is related to the calculation of TKE, it is reasonable that they show similar behavior. For static stability, the Brunt–Väisälä frequency (N^2) shows no distinct behavior, with most of the region reaching the typical stratospheric value. These characteristics of the mixing event are consistent with the findings by Kaluza et al. (2021), where strong vertical wind shear is able to be maintained under stable conditions. The strong upward mixing of the tropospheric air cannot be easily attributed to the vertical wind shear or deformation. Although light turbulence occurs in the strong upward mixing regions, the same strength of mixing as the downward flow cannot be explained. According to the

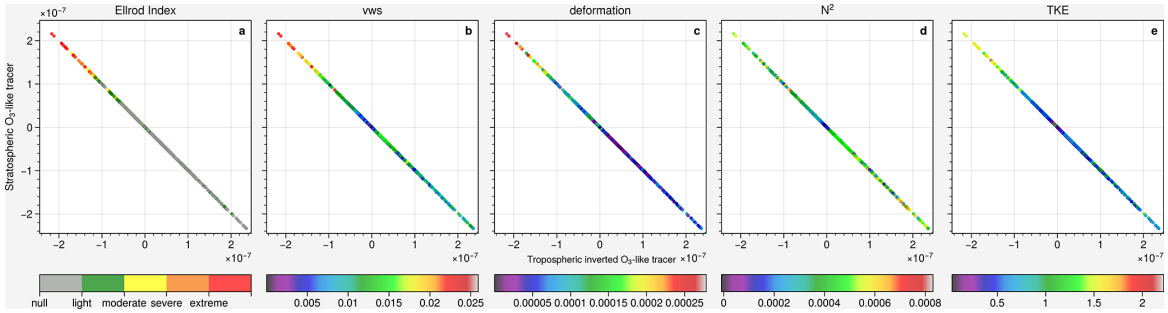

Figure 10. Case 1: Delta tracer–tracer correlation for determining the direction of vertical mixing of stratospheric O_3-like/inverted tropospheric O_3-like tracers (mol mol^{-1}) color-coded with **(a)** Ellrod index (s^{-2}), **(b)** vertical wind shear (s^{-1}), **(c)** deformation (s^{-1}), **(d)** Brunt–Väisälä frequency (s^{-2}), and **(e)** turbulence kinetic energy (m^2 s^{-2}) on 5 February 2016 at 18:00 UTC.

constitutive equation of vertical diffusion in Fig. 2.3, the turbulent flux of tracers is calculated by the diffusion coefficient and the gradient of the tracer. Besides the diffusion coefficient, which is determined by the dynamics and thermodynamics of the atmosphere, the tracer gradient also plays a role on the mixing strength, such that mixing in a homogeneous atmosphere will have no effects on the tracers no matter how strong the mixing coefficient would be. In order to investigate the impact of the tracer gradient, the mixing is normalized by the tracer gradient to remove its impact. Figure 11 shows the same delta tracer–tracer plot but color-coded with absolute value of the difference of the stratospheric O_3-like tracer (left, $|dO_3ST|$) and absolute value normalized with the tracer gradient (right, $|dO_3ST|/|\text{gradient}|$). The downward mixing attributed to the dynamical forcing remained strong after normalization, while the upward mixing with much weaker dynamical forcing became weaker compared to the downward flow after normalization, showing that the upward flow could be attributed to the tracer gradient.

3.3.2 Case 2: imbalanced bidirectional mixing

Case 2 (Fig. 12), again located within a typical high-level ridge trough system over Europe instead of within the transition region as in case 1, is closer to the ridge axis. It is also associated with the jet stream, region with relatively low *Ri* are found at the vicinity of the tropopause and jet stream (Fig. 13).

Figure 14 shows a similar plot to Fig. 10, however, this time for an imbalanced bidirectional mixing event on 5 February 2016 at 05:00 UTC. The graph also shows a diagonal distribution, but asymmetrically. The lower right have a significantly shorter range than the upper left (unlike Case 1, which has a similar range on both ends). This indicates that in this specific profile, the changes in stratospheric air are different from the tropospheric air. This is a consequence of asymmetric stability and flow conditions, i.e., the stable layering of the stratosphere prevents deeper mixing into the stratosphere, whereas the lower static stability in the troposphere allows for deeper penetration of stratospheric tracers into the troposphere (where in Fig. 14d the lower right with high N^2 has a shorter range than the upper left with low N^2, while Fig. 10d of case 1 has a similar N^2 on both ends).

The mixing strength in this case is relatively weak compared to the other cases. The stronger downward mixing of stratospheric air could again be attributed to the relatively strong vertical wind shear and deformation, most of the region with downward mixing is at least experiencing light to moderate turbulence. The low static stability also plays a role in the stronger downward mixing.

The region with weaker upward mixing exhibits noticeably weaker vertical wind shear and deformation compared to the region with downward mixing. The atmosphere is also much more stably stratified than the region with strong downward mixing (the N^2 is distinctly higher in this region). The upward mixing tropospheric air is therefore weaker because the weak dynamical instability is suppressed by the strong static stability.

3.3.3 Case 3: mixing associated with strong vertical gradient

Case 3 (Fig. 15) is located at the outflow region of the high-level trough ridge system, with potential of strong divergence. It is also the only case that the jet stream was shifted outside of the CM10 model domain, causing it to be relatively stable compared to the other two cases (Fig. 16).

Figure 17 shows another mixing event associated with strong vertical gradient on 3 February 2016 at 22:00 UTC. The mixing again shows a diagonal and symmetric distribution but with more scatter from the diagonal. This means, that the mixing does not only lead to equal changes in the tracer distributions, but more to entries of tropospheric tracers into regions of typically stratospherically dominated regimes. The scatter away from the diagonal, unlike the other two cases, where the modeled TKE is better correlated with the mixing (not shown), is due to the advection, the mixing shown in Fig. S17 and S22 located at the downwind re-

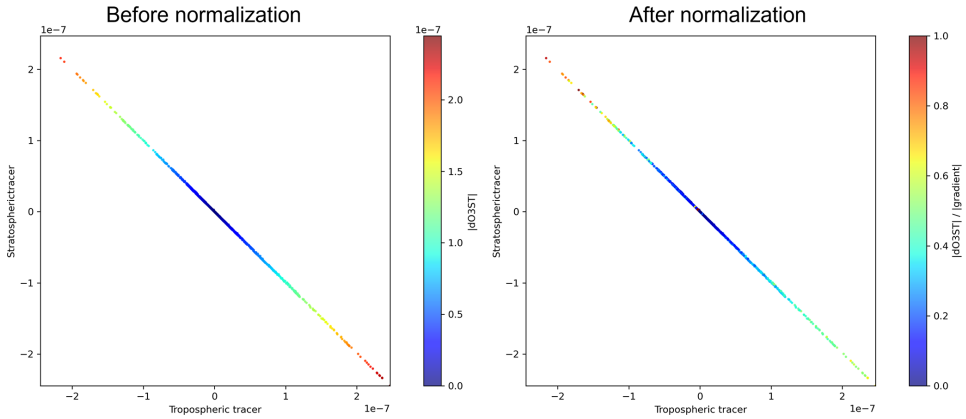

Figure 11. Delta tracer–tracer correlation color-coded with $|dO_3ST|$ (mol mol^{-1}; left) and $|dO_3ST|/|gradient|$ (right).

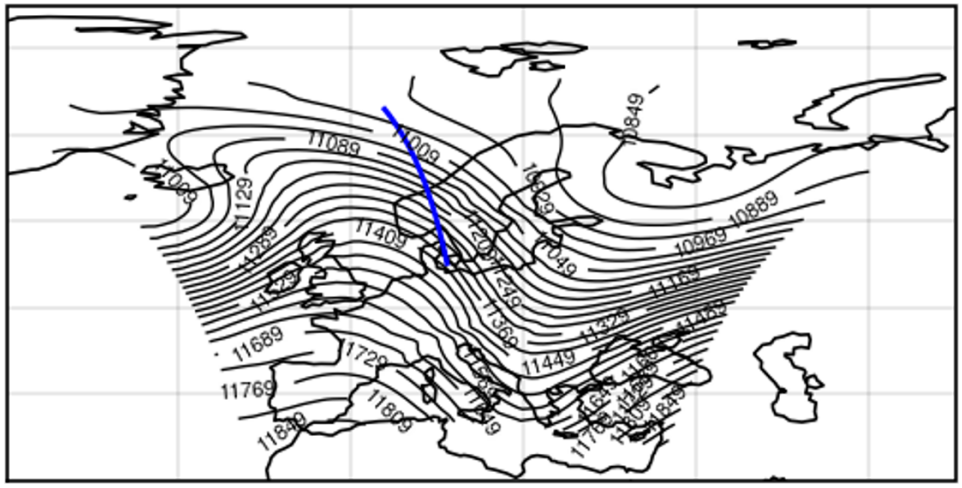

Figure 12. Case 2: geopotential height (gpm) at 200 hPa from CM40 on 5 February 2016 at 05:00 UTC. The blue line indicates the location of the selected cross section of case 2.

gion of the high TKE region (Fig. S21). In the earlier time, the mixing region (Fig. S22, left panel) is more co-located with the high TKE region (Fig. S21, left panel). After several hours, the mixing region (Fig. S22, right panel) propagates to the downwind region, while the high TKE region (Fig. S21, right panel) remains at the same location. The strong horizontal advection in the region of strong horizontal gradients changes the background ratios in addition to the vertical mixing and thus introduces additional mixing during each time step compared to the other cases. The wider the scatter is, the more, e.g., tropospheric tracer depletion is found at similar stratospheric tracer values.

However, in contrast to case 1, the dynamical and thermodynamical forcing do not play a key role in this case. The Ellrod index shows nearly no turbulence at all, neither vertical wind shear nor deformation shows any distinct behavior as in case 1. The static stability does not reach very high values in the stratosphere, such that the mixing is almost equally balanced.

3.3.4 Case inter-comparison

In order to examine whether the tracer gradient is responsible for the strength of the mixing events, the mixing is again normalized by the tracer gradient. Figures 18 and 19 show the frequency distribution for all 3 cases before (|mixing|) and after (|mixing|/|gradient|) normalization. Cases 1 and 3 have similar strength on mixing while case 2 is significantly weaker. Moreover, Cases 1 and 2 have similar distributions on dynamical forcing whereas case 3 forcing is notably weaker. After normalization, the mixing of Case 3 becomes much weaker considering the dynamical forcing does

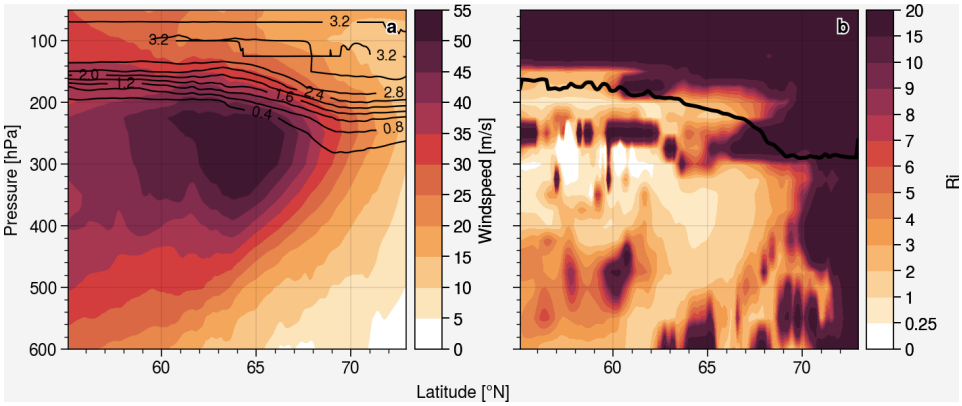

Figure 13. Case 2: **(a)** CM10 horizontal wind speed, the black contour line show the O_3-like tracer and **(b)** gradient Richardson number (*Ri*), the black line indicates the PV tropopause.

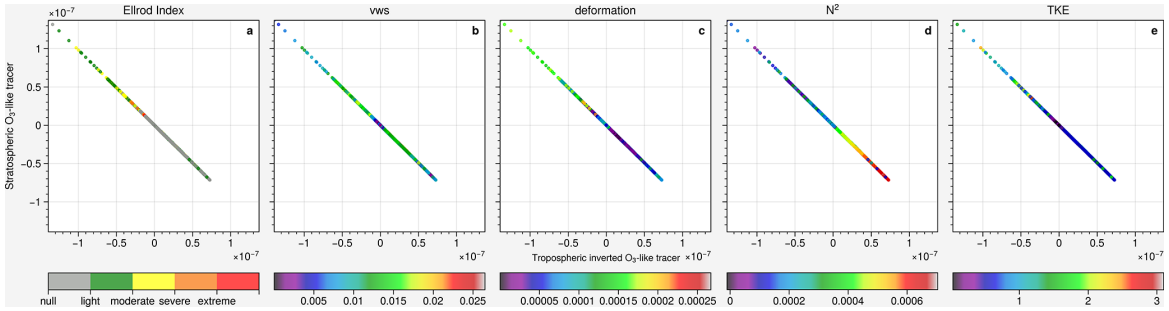

Figure 14. Case 2: delta tracer–tracer correlation of stratospheric O_3-like/inverted tropospheric O_3-like tracers (mol mol^{-1}) color-coded with **(a)** Ellrod index (s^{-2}), **(b)** vertical wind shear (s^{-1}), **(c)** deformation (s^{-1}), **(d)** Brunt–Väisälä frequency (s^{-2}) and **(e)** turbulence kinetic energy (m^2 s^{-2}) on 5 February 2016 at 05:00 UTC.

not play much role, proving that the vertical tracer gradient is responsible for the mixing in this case. Case 1 also becomes relatively weaker as expected since the downward mixing is attributed to the tracer gradient. The weakest case 2 turns out to be the strongest case without the impact of the tracer gradient.

To conclude, vertical turbulent mixing by CAT in the model simulations leads to an enhanced and significant tracer mixing in the UTLS region. The strength and direction of the mixing depends on the particular situation, whether the tracer gradient or the dynamic and thermodynamics of the atmosphere play a role. The tracer gradient plays the most important role since mixing will be meaningless if there is no tracer gradient. This confirms the findings of Kaluza et al. (2021) and Kunkel et al. (2019) that strong dynamical forcing like vertical wind shear could lead to mixing even in the stable atmosphere with a typical stratospheric N^2 value.

4 Conclusions

This study presents model simulations for vertical tracer mixing in the UTLS region. The simulation configuration with an enhanced vertical resolution in the UTLS allows a more detailed analysis of turbulent mixing in this region and provides a suitable tool in the future understanding and quantification of the bidirectional cross-tropopause transport with implications on Earth's radiation budget. In this work, a new enhanced vertical resolution model setup ($\sim$ 200 m vertical resolution in the UTLS) for the regional model COSMO, which is nested within the multi-scale climate chemistry model MECO(n), is presented. It performs similar to established configurations and the ERA5 reanalysis with respect to large-scale temperature and humidity fields in the UTLS, but allows a better representation and analysis of turbulent mixing events in this region. Within the relatively short simulation period, the simulations are able to capture several distinct turbulent mixing events in the UTLS with different characteristics including balanced and imbalanced bidirectional

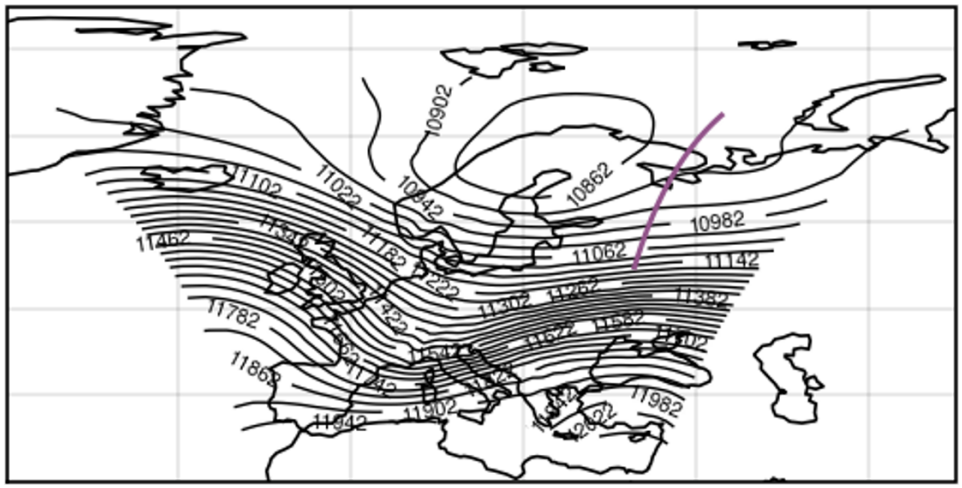

Figure 15. Case 3: geopotential height (gpm) at 200 hPa from CM40 on 3 February 2016 at 22:00 UTC. The purple line indicates the location of the selected cross section of case 3.

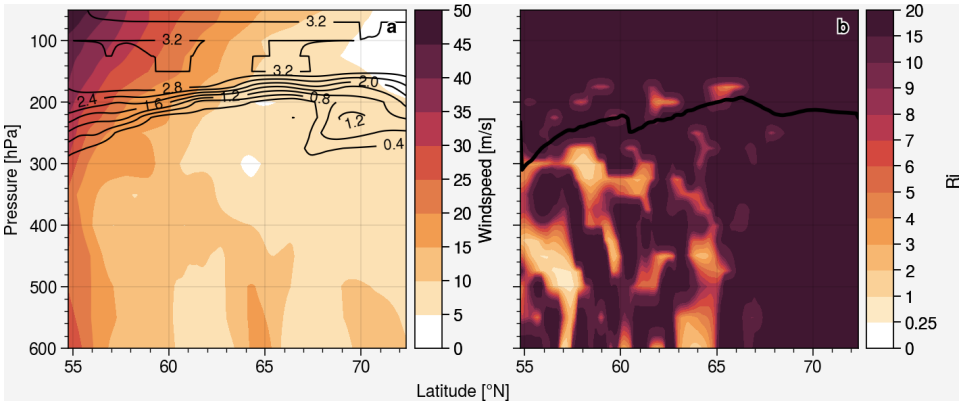

Figure 16. Case 3: **(a)** CM10 horizontal wind speed, the black contour line show the O_3-like tracer and **(b)** gradient Richardson number (*Ri*), the black line indicates the PV tropopause.

mixing induced by turbulence and strong vertical tracer gradient.

The simulated turbulent kinetic energy (TKE) is spatially and temporally well matched with the (post-simulation) diagnosed Ellrod index, showing the model is able to generate turbulence in the UTLS in agreement with the grid-scale wind field data from the model output. The derived turbulence signal from N_2O also shows a reasonable consistency with the simulated turbulence. However, further comparison with observation is needed considering both the modeled TKE and diagnosed Ellrod index are calculated from the COSMO wind field. This model turbulence is able to significantly mix trace species vertically, as analyzed from the changes in the vertical distribution of passive tracers. However, individual mixing events depend on the particular weather situation, for example, the vicinity of a jet stream which located near the tropopause experiencing the strongest mixing due to the high vertical wind shear and tracer gradient (case 1). However, it remains challenging to determine how well the model mixing strength is compared to the real world. Further analysis with measurement data is needed when a more comprehensive measurement dataset is available.

The diagnostic of a delta tracer–tracer correlation is used for the analysis of model simulations, in which the correlation of tracer differences between simulations with and without a representation of the turbulent mixing in the UTLS of stratospheric and tropospheric tracers are compared against each other. Both the vertical tracer gradient and the dynamic and thermodynamic forcing, i.e., the stability and stratification, play important roles in the strength of vertical species

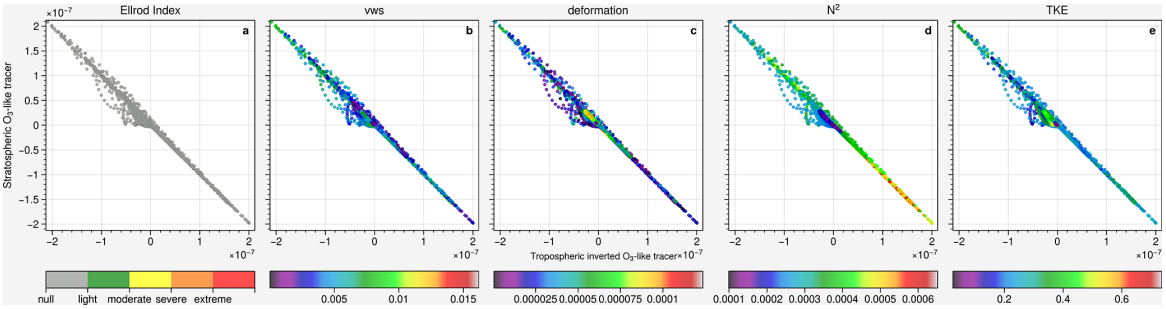

Figure 17. Case 3: delta tracer–tracer correlation of stratospheric O_3-like/inverted tropospheric O_3-like tracers (mol mol^{-1}) color-coded with **(a)** Ellrod index (s^{-2}), **(b)** vertical wind shear (s^{-1}), **(c)** deformation (s^{-1}), **(d)** Brunt–Väisälä frequency (s^{-2}) and **(e)** turbulence kinetic energy (m^2 s^{-2}) on 3 February 2016 at 22:00 UTC.

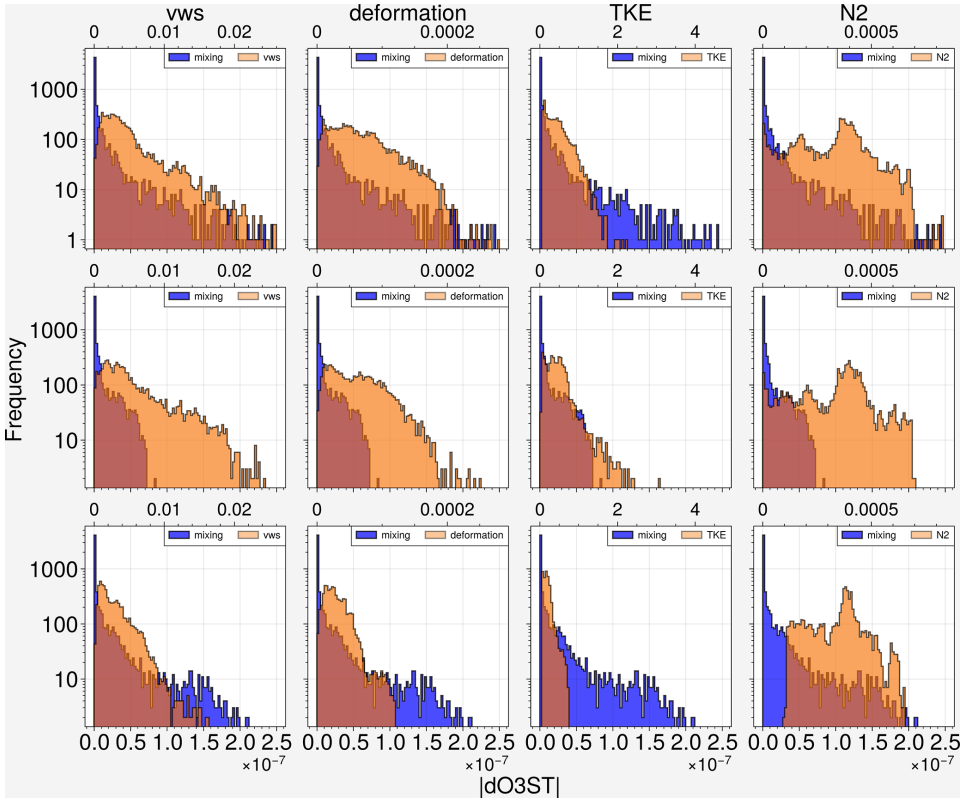

Figure 18. Frequency distribution of |dO$_3$ST| (mol mol^{-1}) of O_3-like tracers, vertical wind shear, deformation, TKE and N2 for case 1 (top), case 2 (middle), and case 3 (bottom).

exchange, especially when the vertical wind shear is strong enough to overcome the stable atmosphere. Depending on the individual situation, either the dynamical forcing or pre-existing tracer gradients (or both) can be the dominant drivers for the exchange events. The favorable combination of both factors can lead to an efficient mixing event, maximising tracer exchange fluxes. These events can be irreversible, i.e., the exchange of tracers happens along the diagonal of a delta tracer–tracer correlation, leading to a disturbance of typical stratospheric or tropospheric chemical compositions in the respective parts of the atmosphere with implications for climate, e.g., via the radiative impact of exchanged species.

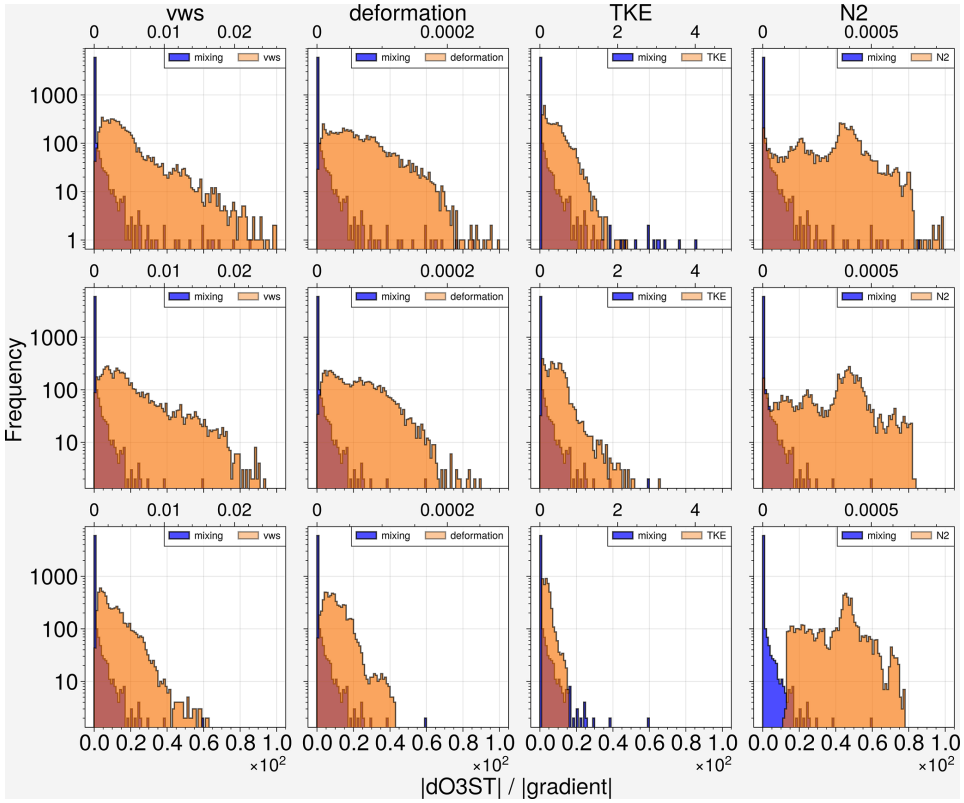

Figure 19. Frequency distribution of $|dO_3ST|/|gradient|$ of O_3-like tracers, vertical wind shear, deformation, TKE and N2 for case 1 (top), case 2 (middle), and case 3 (bottom).

Code availability. The model code of the MECO(n) system can be obtained by becoming a member of the EMAC consortium as described on the corresponding webpage at https://messy-interface.org (last access: 1 December 2024).

Data availability. Data from this work are available upon request.

Supplement. The supplement related to this article is available online at https://doi.org/10.5194/acp-25-13123-2025-supplement.

Author contributions. CHC and HT conceptualized the study with contributions from PH. CHC performed the simulations and analyzed the model results. The results were interpreted by CHC, HT and PH. CHC wrote the article with significant input from HT and PH.

Competing interests. The contact author has declared that none of the authors has any competing interests.

Disclaimer. Publisher's note: Copernicus Publications remains neutral with regard to jurisdictional claims made in the text, published maps, institutional affiliations, or any other geographical representation in this paper. While Copernicus Publications makes every effort to include appropriate place names, the final responsibility lies with the authors. Also, please note that this paper has not received English language copy-editing. Views expressed in the text are those of the authors and do not necessarily reflect the views of the publisher.

Special issue statement. This article is part of the special issue "The Modular Earth Submodel System (MESSy) (ACP/GMD inter-journal SI)". It is not associated with a conference.

Acknowledgements. This work has been funded by the Deutsche Forschungsgemeinschaft (DFG, German Research Foundation) – TRR 301 – Project-ID 428312742 (project B01). The simulations were conducted using the supercomputer MOGON II of Johannes Gutenberg University Mainz.

Financial support. This research has been supported by the Deutsche Forschungsgemeinschaft (grant no. 428312742).

This open-access publication was funded by Johannes Gutenberg University Mainz.

Review statement. This paper was edited by Petr Šácha and reviewed by three anonymous referees.

References

Baldauf, M., Seifert, A., Förstner, J., Majewski, D., Raschendorfer, M., and Reinhardt, T.: Operational convective-scale numerical weather prediction with the COSMO model: Description and sensitivities, Monthly Weather Review, 139, 3887–3905, https://doi.org/10.1175/MWR-D-10-05013.1, 2011.

Blackadar, A. K.: The vertical distribution of wind and turbulent exchange in a neutral atmosphere, Journal of Geophysical Research, 67, 3095–3102, https://doi.org/10.1029/JZ067i008p03095, 1962.

Butchart, N. and Scaife, A.: Removal of chlorofluorocarbons by increased mass exchange between the stratosphere and troposphere in a changing climate, Nature, 410, 799–802, https://doi.org/10.1038/35071047, 2001.

Dee, D. P., Uppala, S. M., Simmons, A. J., Berrisford, P., Poli, P., Kobayashi, S., Andrae, U., Balmaseda, M. A., Balsamo, G., Bauer, P., Bechtold, P., Beljaars, A. C. M., van de Berg, L., Bidlot, J., Bormann, N., Delsol, C., Dragani, R., Fuentes, M., Geer, A. J., Haimberger, L., Healy, S. B., Hersbach, H., Hólm, E. V., Isaksen, L., Kållberg, P., Köhler, M., Matricardi, M., McNally, A. P., Monge-Sanz, B. M., Morcrette, J.-J., Park, B.-K., Peubey, C., de Rosnay, P., Tavolato, C., Thépaut, J.-N., and Vitart, F.: The ERA-Interim reanalysis: configuration and performance of the data assimilation system, Quarterly Journal of the Royal Meteorological Society, 137, 553–597, https://doi.org/10.1002/qj.828, 2011.

Doms, G. and Baldauf, M.: A description of the nonhydrostatic regional model COSMO-Model, Part I: Dynamics and Numerics, Deutscher Wetterdienst, Offenbach, (Ed.) U. Schättler, https://doi.org/10.5676/DWD_pub/nwv/cosmo-doc_6.00_I, 2018.

Doms, G., Förstner, J., Heise, E., Herzog, H.-J., Mironov, D., Raschendorfer, M., Reinhardt, T., Ritter, B., Schrodin, R., Schulz, J.-P., and Vogel, G.: Consortium for small-scale modelling a description of the nonhydrostatic regional COSMO-model part II physical parameterizations, Deutscher Wetterdienst, https://doi.org/10.5676/DWD_pub/nwv/cosmo-doc_5.05_II, 2018.

Dutton, J. A. and Panofsky, H. A.: Clear air turbulence: a mystery may be unfolding, Science, 167, 937–944, https://doi.org/10.1126/science.167.3920.937, 1970.

Eckstein, J., Schmitz, S., and Ruhnke, R.: Reaching the lower stratosphere: validating an extended vertical grid for COSMO, Geosci. Model Dev., 8, 1839–1855, https://doi.org/10.5194/gmd-8-1839-2015, 2015.

Ellrod, G., Lester, P., and Ehernberger, L.: Clear air turbulence, in: Encyclopedia of Atmospheric Sciences, 393–403, ISBN 978-0-12-227090-1, https://doi.org/10.1016/B0-12-227090-8/00104-4, 2003.

Ellrod, G. P. and Knapp, D. I.: An objective clear-air turbulence forecasting technique: Verification and operational use, Weather and Forecasting, 7, 150–165, https://doi.org/10.1175/1520-0434(1992)007<0150:AOCATF>2.0.CO;2, 1992.

Ellrod, G. P. and Knox, J. A.: Improvements to an operational clear-air turbulence diagnostic index by addition of a divergence trend term, Weather and Forecasting, 25, 789–798, https://doi.org/10.1175/2009WAF2222290.1, 2010.

Esler, J. G. and Polvani, L. M.: Kelvin–helmholtz instability of potential vorticity layers: a route to mixing, Journal of the Atmospheric Sciences, 61, 1392–1405, https://doi.org/10.1175/1520-0469(2004)061<1392:KIOPVL>2.0.CO;2, 2004.

Forster, P., Storelvmo, T., Armour, K., Collins, W., Dufresne, J.-L., Frame, D., Lunt, D., Mauritsen, T., Palmer, M., Watanabe, M., Wild, M., and Zhang, H.: Chapter 7: The Earth's energy budget, climate feedbacks, and climate sensitivity, Climate Change 2021: The Physical Science Basis. Contribution of Working Group I to the Sixth Assessment Report of the Intergovernmental Panel on Climate Change, https://doi.org/10.25455/wgtn.16869671.v1, 2021.

Forster, P. M. and Shine, K. P.: Radiative forcing and temperature trends from stratospheric ozone changes, Journal of Geophysical Research-Atmospheres, 102, 10841–10855, https://doi.org/10.1029/96JD03510, 1997.

Forster, P. M. and Shine, K. P.: Stratospheric water vapour changes as a possible contributor to observed stratospheric cooling, Geophysical Research Letters, 26, 3309–3312, https://doi.org/10.1029/1999GL010487, 1999.

Forster, P. M. d. F. and Shine, K. P.: Assessing the climate impact of trends in stratospheric water vapor, Geophysical Research Letters, 29, 10-1–10-4, https://doi.org/10.1029/2001GL013909, 2002.

Gettelman, A., Hoor, P., Pan, L. L., Randel, W. J., Hegglin, M. I., and Birner, T.: The extratropical upper troposphere and lower stratosphere, Reviews of Geophysics, 49, https://doi.org/10.1029/2011RG000355, 2011.

Giorgetta, M. A., Manzini, E., Roeckner, E., Esch, M., and Bengtsson, L.: Climatology and forcing of the quasi-biennial oscillation in the MAECHAM5 model, Journal of Climate, 19, 3882–3901, https://doi.org/10.1175/JCLI3830.1, 2006.

Holton, J. R., Haynes, P. H., McIntyre, M. E., Douglass, A. R., Rood, R. B., and Pfister, L.: Stratosphere-troposphere exchange, Reviews of Geophysics, 33, 403–439, https://doi.org/10.1029/95RG02097, 1995.

Hu, B., Tang, J., Ding, J., and Liu, G.: Regional downscaled future change of clear-air turbulence over East Asia under RCP8.5 scenario within the CORDEX-EA-II project, International Journal of Climatology, 41, 5022–5035, https://doi.org/10.1002/joc.7114, 2021.

Jaeger, E. B. and Sprenger, M.: A Northern Hemispheric climatology of indices for clear air turbulence in the tropopause region derived from ERA40 reanalysis data, Journal of Geophysical Research-Atmospheres, 112, https://doi.org/10.1029/2006JD008189, 2007.

Jeuken, A. B. M., Siegmund, P. C., Heijboer, L. C., Feichter, J., and Bengtsson, L.: On the potential of assimilating meteorological analyses in a global climate model for the purpose of model

validation, Journal of Geophysical Research-Atmospheres, 101, 16939–16950, https://doi.org/10.1029/96JD01218, 1996.

Jöckel, P., Sander, R., Kerkweg, A., Tost, H., and Lelieveld, J.: Technical Note: The Modular Earth Submodel System (MESSy) - a new approach towards Earth System Modeling, Atmos. Chem. Phys., 5, 433–444, https://doi.org/10.5194/acp-5-433-2005, 2005.

Jöckel, P., Tost, H., Pozzer, A., Brühl, C., Buchholz, J., Ganzeveld, L., Hoor, P., Kerkweg, A., Lawrence, M. G., Sander, R., Steil, B., Stiller, G., Tanarhte, M., Taraborrelli, D., van Aardenne, J., and Lelieveld, J.: The atmospheric chemistry general circulation model ECHAM5/MESSy1: consistent simulation of ozone from the surface to the mesosphere, Atmos. Chem. Phys., 6, 5067–5104, https://doi.org/10.5194/acp-6-5067-2006, 2006.

Jöckel, P., Kerkweg, A., Buchholz-Dietsch, J., Tost, H., Sander, R., and Pozzer, A.: Technical Note: Coupling of chemical processes with the Modular Earth Submodel System (MESSy) submodel TRACER, Atmos. Chem. Phys., 8, 1677–1687, https://doi.org/10.5194/acp-8-1677-2008, 2008.

Jöckel, P., Kerkweg, A., Pozzer, A., Sander, R., Tost, H., Riede, H., Baumgaertner, A., Gromov, S., and Kern, B.: Development cycle 2 of the Modular Earth Submodel System (MESSy2), Geosci. Model Dev., 3, 717–752, https://doi.org/10.5194/gmd-3-717-2010, 2010.

Kaluza, T., Kunkel, D., and Hoor, P.: On the occurrence of strong vertical wind shear in the tropopause region: a 10-year ERA5 northern hemispheric study, Weather Clim. Dynam., 2, 631–651, https://doi.org/10.5194/wcd-2-631-2021, 2021.

Keller, J. L.: Clear air turbulence as a response to meso- and synoptic-scale dynamic processes, Monthly Weather Review, 118, 2228–2243, https://doi.org/10.1175/1520-0493(1990)118<2228:CATAAR>2.0.CO;2, 1990.

Kerkweg, A. and Jöckel, P.: The 1-way on-line coupled atmospheric chemistry model system MECO(n) – Part 2: On-line coupling with the Multi-Model-Driver (MMD), Geosci. Model Dev., 5, 111–128, https://doi.org/10.5194/gmd-5-111-2012, 2012a.

Kerkweg, A. and Jöckel, P.: The 1-way on-line coupled atmospheric chemistry model system MECO(n) – Part 1: Description of the limited-area atmospheric chemistry model COSMO/MESSy, Geosci. Model Dev., 5, 87–110, https://doi.org/10.5194/gmd-5-87-2012, 2012b.

Kerkweg, A., Hofmann, C., Jöckel, P., Mertens, M., and Pante, G.: The on-line coupled atmospheric chemistry model system MECO(n) – Part 5: Expanding the Multi-Model-Driver (MMD v2.0) for 2-way data exchange including data interpolation via GRID (v1.0), Geosci. Model Dev., 11, 1059–1076, https://doi.org/10.5194/gmd-11-1059-2018, 2018.

Kunkel, D., Hoor, P., Kaluza, T., Ungermann, J., Kluschat, B., Giez, A., Lachnitt, H.-C., Kaufmann, M., and Riese, M.: Evidence of small-scale quasi-isentropic mixing in ridges of extratropical baroclinic waves, Atmos. Chem. Phys., 19, 12607–12630, https://doi.org/10.5194/acp-19-12607-2019, 2019.

Lachnitt, H.-C., Hoor, P., Kunkel, D., Bramberger, M., Dörnbrack, A., Müller, S., Reutter, P., Giez, A., Kaluza, T., and Rapp, M.: Gravity-wave-induced cross-isentropic mixing: a DEEPWAVE case study, Atmos. Chem. Phys., 23, 355–373, https://doi.org/10.5194/acp-23-355-2023, 2023.

Lacis, A. A., Wuebbles, D. J., and Logan, J. A.: Radiative forcing of climate by changes in the vertical distribution of ozone, Journal of Geophysical Research-Atmospheres, 95, 9971–9981, https://doi.org/10.1029/JD095iD07p09971, 1990.

Lelieveld, J. and Dentener, F. J.: What controls tropospheric ozone?, Journal of Geophysical Research-Atmospheres, 105, 3531–3551, https://doi.org/10.1029/1999JD901011, 2000.

Meloen, J., Siegmund, P., van Velthoven, P., Kelder, H., Sprenger, M., Wernli, H., Kentarchos, A., Roelofs, G., Feichter, J., Land, C., Forster, C., James, P., Stohl, A., Collins, W., and Cristofanelli, P.: Stratosphere-troposphere exchange: A model and method intercomparison, Journal of Geophysical Research-Atmospheres, 108, https://doi.org/10.1029/2002JD002274, 2003.

Mertens, M., Kerkweg, A., Jöckel, P., Tost, H., and Hofmann, C.: The 1-way on-line coupled model system MECO(n) – Part 4: Chemical evaluation (based on MESSy v2.52), Geosci. Model Dev., 9, 3545–3567, https://doi.org/10.5194/gmd-9-3545-2016, 2016.

Miyazaki, K., Watanabe, S., Kawatani, Y., Tomikawa, Y., Takahashi, M., and Sato, K.: Transport and mixing in the extratropical tropopause region in a high-vertical-resolution GCM. Part I: Potential vorticity and heat budget analysis, Journal of the Atmospheric Sciences, 67, 1293–1314, https://doi.org/10.1175/2009JAS3221.1, 2010.

Muller, E.: Turbulent flux parameterization in a regional-scale model, phd, ECMWF, Shinfield Park, Reading, 193–220, 1981.

Muñoz-Esparza, D., Sharman, R. D., and Trier, S. B.: On the consequences of PBL scheme diffusion on UTLS wave and turbulence representation in high-resolution NWP models, Monthly Weather Review, 148, 4247–4265, https://doi.org/10.1175/MWR-D-20-0102.1, 2020.

Overeem, A.: Verification of clear-air turbulence forecasts, Citeseer, https://cdn.knmi.nl/knmi/pdf/bibliotheek/knmipubTR/TR244.pdf, 2002.

Randel, W. J., Wu, F., and Forster, P.: The extratropical tropopause inversion layer: Global observations with GPS data, and a radiative forcing mechanism, Journal of the Atmospheric Sciences, 64, 4489–4496, https://doi.org/10.1175/2007JAS2412.1, 2007.

Riese, M., Ploeger, F., Rap, A., Vogel, B., Konopka, P., Dameris, M., and Forster, P.: Impact of uncertainties in atmospheric mixing on simulated UTLS composition and related radiative effects, Journal of Geophysical Research-Atmospheres, 117, https://doi.org/10.1029/2012JD017751, 2012.

Roeckner, E., Bäuml, G., Bonaventura, L., Brokopf, R., Esch, M., Giorgetta, M., Hagemann, S., Kirchner, I., Kornblueh, L., Manzini, E., Schlese, U., and Schulzweida, U.: The atmospheric general circulation model ECHAM 5. PART I: Model description, Max-Planck-Institut für Meteorologie, https://pure.mpg.de/pubman/faces/ViewItemOverviewPage.jsp?itemId=item_995269, 2003.

Schättler, U., Doms, G., and Schraff, C.: Consortium for small-scale modelling a description of the nonhydrostatic regional COSMO-model part VII: User's guide, Deutscher Wetterdienst, Offenbach, https://doi.org/10.5676/DWD_pub/nwv/cosmo-doc_6.00_VII, 2021.

Shapiro, M. A.: Turbulent mixing within tropopause folds as a mechanism for the exchange of chemical constituents between the stratosphere and troposphere, Journal of Atmospheric Sciences, 37, 994–1004, https://doi.org/10.1175/1520-0469(1980)037<0994:TMWTFA>2.0.CO;2, 1980.

Sharman, R., Tebaldi, C., Wiener, G., and Wolff, J.: An integrated approach to mid- and upper-level turbulence forecasting, Weather and Forecasting, 21, 268–287, https://doi.org/10.1175/WAF924.1, 2006.

Smith, I. H., Williams, P. D., and Schiemann, R.: Clear-air turbulence trends over the North Atlantic in high-resolution climate models, Climate Dynamics, 61, 1–17, 2023.

Sprenger, M. and Wernli, H.: A northern hemispheric climatology of cross-tropopause exchange for the ERA15 time period (1979–1993), Journal of Geophysical Research-Atmospheres, 108, https://doi.org/10.1029/2002JD002636, 2003.

Stohl, A., Bonasoni, P., Cristofanelli, P., Collins, W., Feichter, J., Frank, A., Forster, C., Gerasopoulos, E., Gäggeler, H., James, P., Kentarchos, T., Kromp-Kolb, H., Krüger, B., Land, C., Meloen, J., Papayannis, A., Priller, A., Seibert, P., Sprenger, M., Roelofs, G. J., Scheel, H. E., Schnabel, C., Siegmund, P., Tobler, L., Trickl, T., Wernli, H., Wirth, V., Zanis, P., and Zerefos, C.: Stratosphere-troposphere exchange: A review, and what we have learned from STACCATO, Journal of Geophysical Research-Atmospheres, 108, https://doi.org/10.1029/2002JD002490, 2003a.

Stohl, A., Wernli, H., James, P., Bourqui, M., Forster, C., Liniger, M. A., Seibert, P., and Sprenger, M.: A new perspective of stratosphere–troposphere exchange, Bulletin of the American Meteorological Society, 84, 1565–1574, https://doi.org/10.1175/BAMS-84-11-1565, 2003b.

Storer, L. N., Williams, P. D., and Joshi, M. M.: Global response of clear-air turbulence to climate change, Geophysical Research Letters, 44, 9976–9984, https://doi.org/10.1002/2017GL074618, 2017.

Traub, M. and Lelieveld, J.: Cross-tropopause transport over the eastern Mediterranean, Journal of Geophysical Research-Atmospheres, 108, https://doi.org/10.1029/2003JD003754, 2003.

van Velthoven, P. F. J. and Kelder, H.: Estimates of stratosphere-troposphere exchange: Sensitivity to model formulation and horizontal resolution, Journal of Geophysical Research-Atmospheres, 101, 1429–1434, https://doi.org/10.1029/95JD03407, 1996.

Watkins, C. and Browning, K.: The detection of clear air turbulence by radar, Physics in Technology, 4, 28, https://doi.org/10.1088/0305-4624/4/1/I01, 1973.

Williams, P. D.: Increased light, moderate, and severe clear-air turbulence in response to climate change, Advances in Atmospheric Sciences, 34, 576–586, 2017.

Williams, P. D. and Joshi, M. M.: Intensification of winter transatlantic aviation turbulence in response to climate change, Nature Climate Change, 3, 644–648, 2013.

Witschas, B., Gisinger, S., Rahm, S., Dörnbrack, A., Fritts, D. C., and Rapp, M.: Airborne coherent wind lidar measurements of the momentum flux profile from orographically induced gravity waves, Atmos. Meas. Tech., 16, 1087–1101, https://doi.org/10.5194/amt-16-1087-2023, 2023.

Wolff, J. K. and Sharman, R. D.: Climatology of upper-level turbulence over the contiguous united states, Journal of Applied Meteorology and Climatology, 47, 2198–2214, https://doi.org/10.1175/2008JAMC1799.1, 2008.

Supplement of Atmos. Chem. Phys., 25, 13123–13140, 2025
https://doi.org/10.5194/acp-25-13123-2025-supplement

Atmospheric Chemistry and Physics Open Access

Supplement of

Simulated mixing in the UTLS by small-scale turbulence using multi-scale chemistry-climate model MECO(n)

Chun Hang Chau et al.

Correspondence to: Chun Hang Chau (cchau@uni-mainz.de) and Holger Tost (tosth@uni-mainz.de)

This supplement presents the evaluation of the newly introduced enhanced vertical grid EH-84 and discusses whether EH-84 performs comparably well to EX-60. In order to evaluate EH-84, we validate the CM10 output from EH-84 with ERA-5 reanalysis data (Hersbach et al., 2020) and also intercompare the EH-84 CM10 output with EX-60. In addition, we performed a sensitivity test of the model TKE on both horizontal and vertical resolution.

S1 Basic meteorology

S1.1 Comparison with ERA-5

In this section, the temperature and specific humidity of the CM10 output from EH-84 are compared with the ERA-5 reanalysis data. Since the model outputs from COSMO are height-based and the ERA-5 data are pressure-based, the COSMO output is interpolated to the corresponding pressure level that matches with the ERA-5 data (i.e. 100 hPa, 125 hPa, 150 hPa, 200 hPa, 225 hPa, 250 hPa, 300 hPa, 350 hPa, 400 hPa, 450 hPa and 500 hPa). Figure 1 shows the temperature of the selected pressure levels from COSMO, ERA-5 and the difference (COSMO− ERA-5) for 1st Feb 2016 which is the first day of the simulation. The model results generally agree with the reanalysis data, the patterns of the temperature distribution are generally reproduced in different pressure levels. Although there are some discrepancies between COSMO and ERA5, they are most likely because of the slightly shifted distribution of temperature, the general patterns with the cooler and warmer air mass are able to reproduce distinctly. Figure 2 shows the same plots as Figure S1 but for the last day of the simulation (7th Feb 2016). The model results are still able to reproduce a similar pattern compared to the ERA-5 data. However, the COSMO temperature is generally cooler than the reanalysis data, there is a systematic cold bias for the whole domain with at most more than 4 k cooler. Figure S3 shows the specific humidity of the selected pressure levels for 1st Feb 2016. It can be seen that there is a generally good agreement between the COSMO and ERA-5 data for most of the pressure levels except for the 100 hPa where COSMO is significantly drier than ERA-5. Figure S4 shows the specific humidity for 7th Feb 2016. The specific humidity was still able to produce similar patterns below 200 hPa. For the higher levels, the distribution starts to vary from the ERA-5 data, but most of them remain in the same order of magnitude. Considering the large uncertainty for the UTLS water vapour in reanalysis data (Fujiwara et al., 2022), the variation of the specific humidity is still within an acceptable margin.

S1.2 Discussion on the cold bias

In order to investigate whether the discrepancy (especially the cold bias) between the model and ERA-5 data corresponds to the enhancing vertical resolution, the EH-84 output is further compared with the tested EX-60 output. The model setup for EX-60 is mostly consistent with the setup of EH-84 except for the vertical grid in order to investigate the effect of increasing vertical resolution in EH-84. Both temperature and specific humidity show good agreement with only some slight differences in the order of magnitudes (Figure S5, S6). To elucidate what is responsible for the cold bias, we then compared both the ERA-Interim reanalysis data which initialized the simulation, the EMAC and CM40 output with ERA-5 data. Figure S7 shows the temperature for the last day, ERA-I has no distinct difference when compared with the ERA-5 data. However, the EMAC and CM40 output show a similar cold bias as the CM10 output, which suggests that the cold bias from CM10 originates from EMAC rather than the COSMO model dynamics or the enhanced vertical grid of COSMO.

S1.3 Conclusion

To conclude, the enhanced vertical grid EH-84 for COSMO is able to simulate the atmosphere reasonably. Although there is some discrepancy, the temperature pattern from ERA-5 is generally well produced by the model as well as the relative humidity. The systematic cold bias that occurs in EH-84 is also found in EX-60, indicating that the occurrence of the cold bias is not a result of the constantly increased vertical resolution in the UTLS. Considering the strong alignment between the EH-84 and EX-60 output and the latter is well-tested and well-matched with the observation. The model output from the enhanced vertical grid EH-84 can be seen as reliable and suitable to the needs of this study.

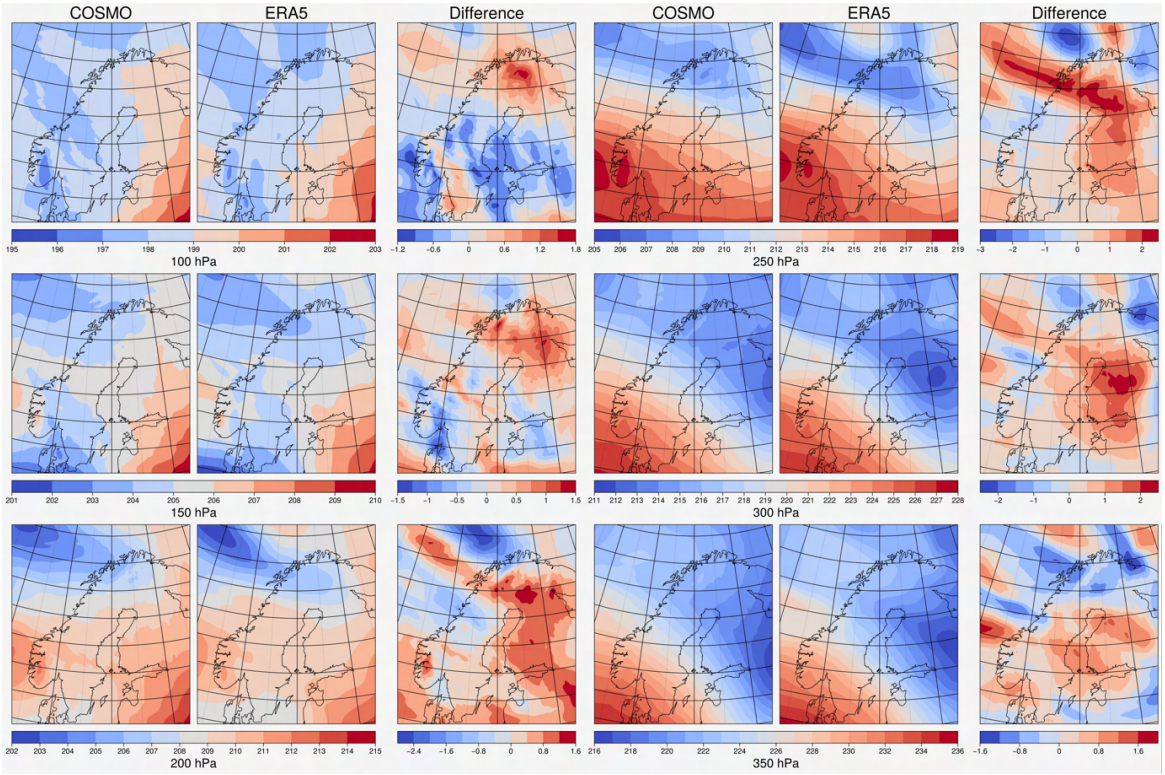

Figure S1. Daily average temperature(K) of 100, 150, 200, 250, 300, 350 hPa at 2016-02-01 for COSMO, ERA5 and the difference.

S2 Sensitivity test

We performed sensitivity tests of the model TKE on both the horizontal and vertical resolution. Results show that TKE is sensitive to the vertical resolution but not the horizontal resolution. The occurrence of high TKE values is more frequent in EH84 than in EX60 (figure S9). The higher vertical resolution results in a more frequent high TKE occurrence. However the occurrence of high TKE values in CM10 and CM40 have no distinct difference as discovered in EH84 and EX60 (figure S10), the finer horizontal resolution does not result in a significant change on TKE. We further investigate the sensitivity of mixing on different resolutions. The EH84 setup results in significantly stronger mixing than EX60 (figure S11) which is as expected considering TKE is a crucial parameter in the turbulence scheme in COSMO. However, the mixing in CM10 is also significantly stronger than in CM40 (figure S12) even though there is no significant difference in TKE, such differences could be attributed to the finer horizontal resolution providing a more detail tropopause which creates a stronger gradient that strengthens the mixing.

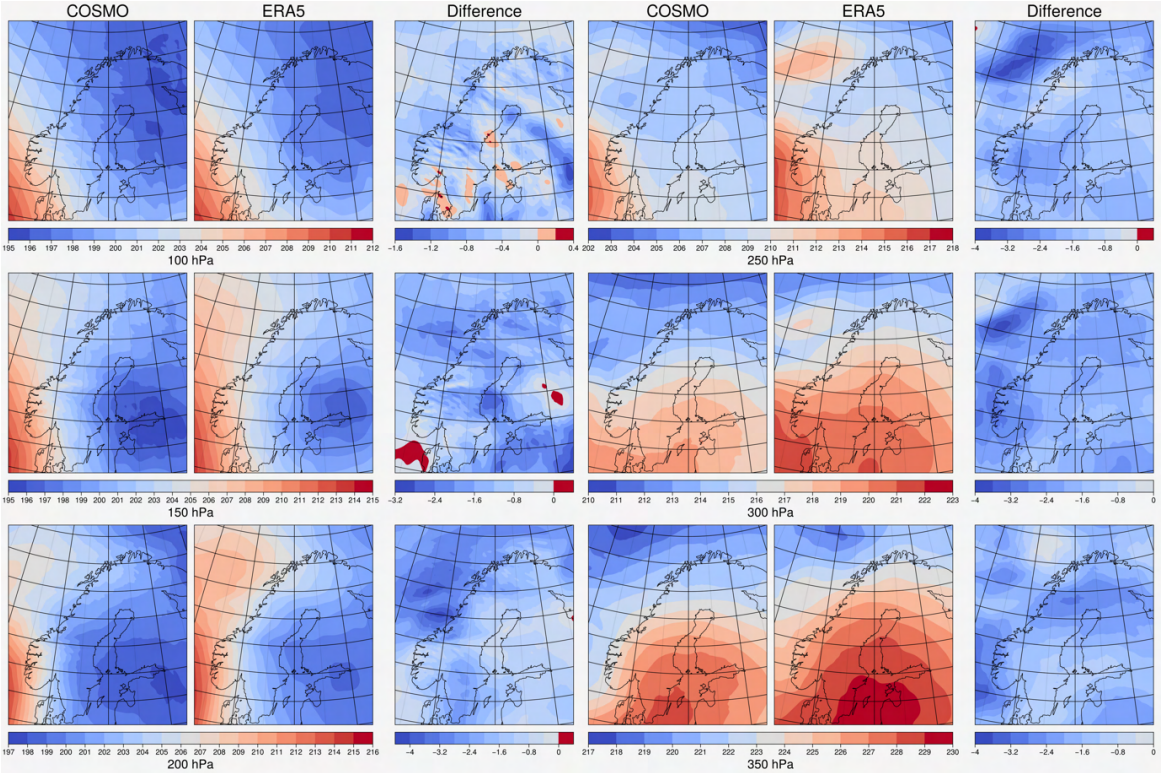

Figure S2. Daily average temperature(K) of 100, 150, 200, 250, 300, 350 hPa at 2016-02-07 for COSMO, ERA5 and the difference.

References

Fujiwara, M., Manney, G., Gray, L., and Wright, J.: SPARC Report No. 10, WCRP Report 6/2021, 2022.

Hersbach, H., Bell, B., Berrisford, P., Hirahara, S., Horányi, A., Muñoz-Sabater, J., Nicolas, J., Peubey, C., Radu, R., Schepers, D., Simmons, A., Soci, C., Abdalla, S., Abellan, X., Balsamo, G., Bechtold, P., Biavati, G., Bidlot, J., Bonavita, M., De Chiara, G., Dahlgren, P., Dee, D., Diamantakis, M., Dragani, R., Flemming, J., Forbes, R., Fuentes, M., Geer, A., Haimberger, L., Healy, S., Hogan, R. J., Hólm, E., Janisková, M., Keeley, S., Laloyaux, P., Lopez, P., Lupu, C., Radnoti, G., de Rosnay, P., Rozum, I., Vamborg, F., Villaume, S., and Thépaut, J.-N.: The ERA5 global reanalysis, Quarterly Journal of the Royal Meteorological Society, 146, 1999–2049, https://doi.org/https://doi.org/10.1002/qj.3803, 2020.

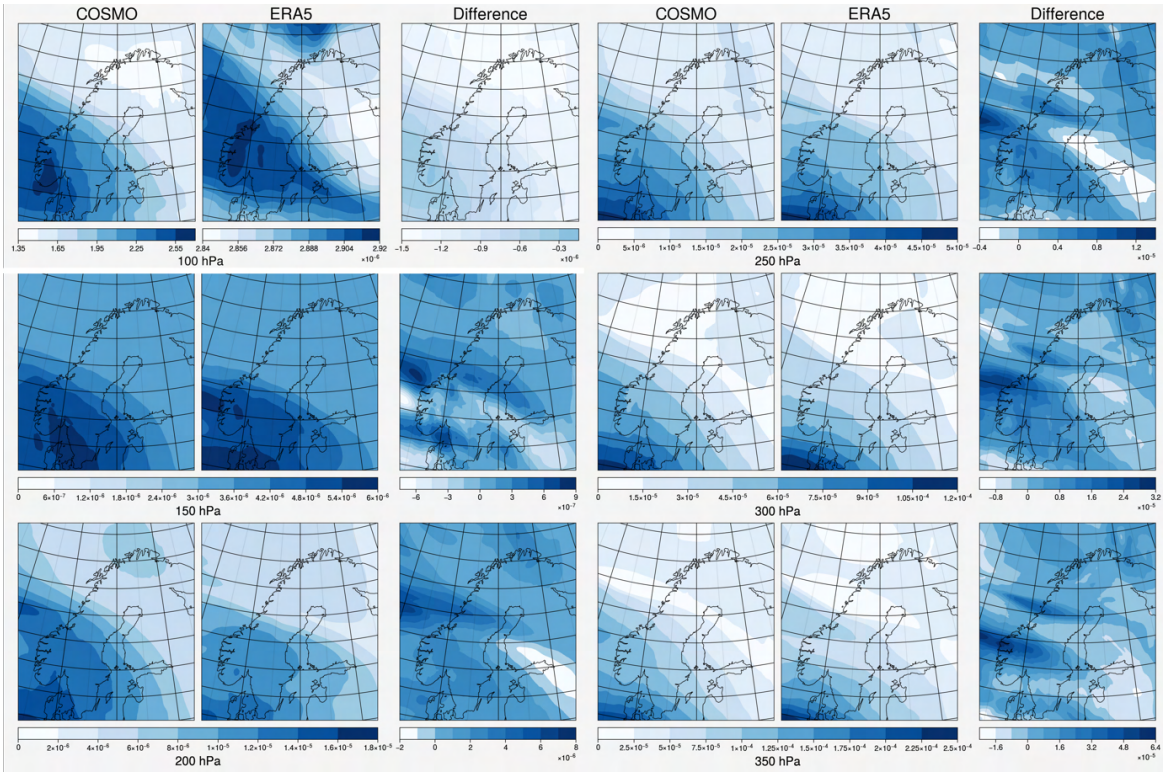

Figure S3. Daily average specific humidity(kg/kg) of 100, 150, 200, 250, 300, 350 hPa at 2016-02-01 for COSMO, ERA5 and the difference.

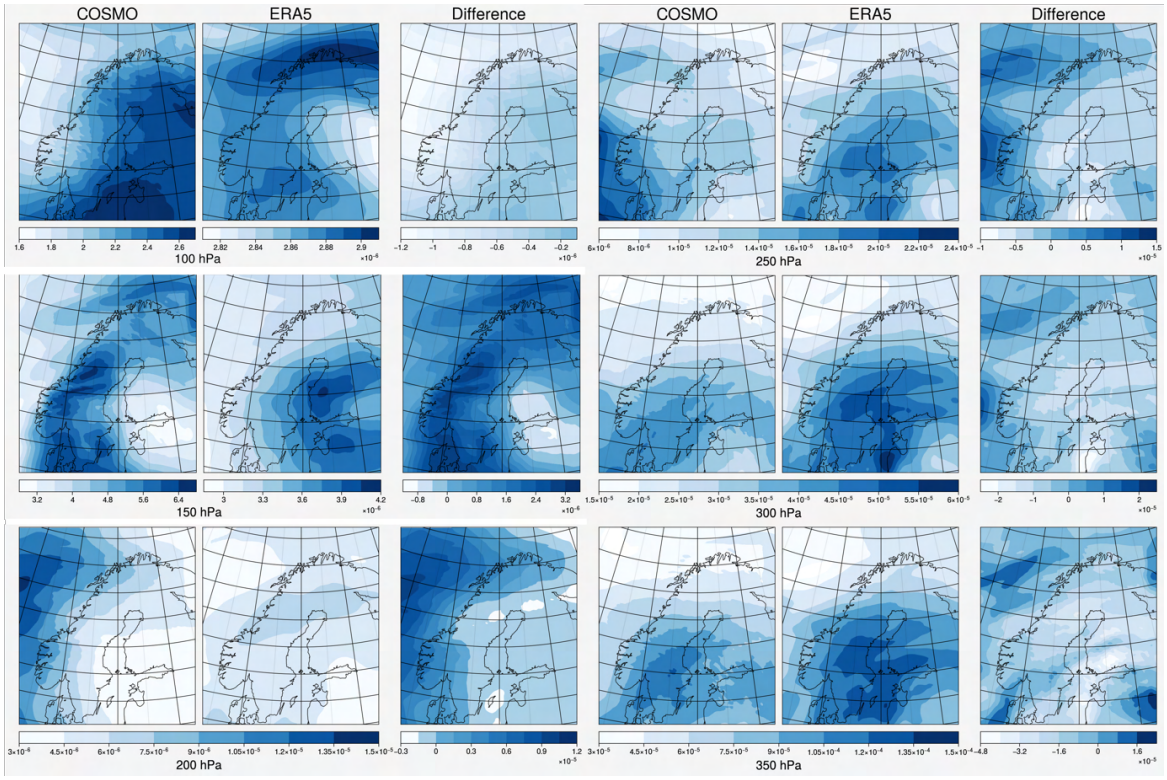

Figure S4. Daily average specific humidity(kg/kg) of 100, 150, 200, 250, 300, 350 hPa at 2016-02-07 for COSMO, ERA5 and the difference.

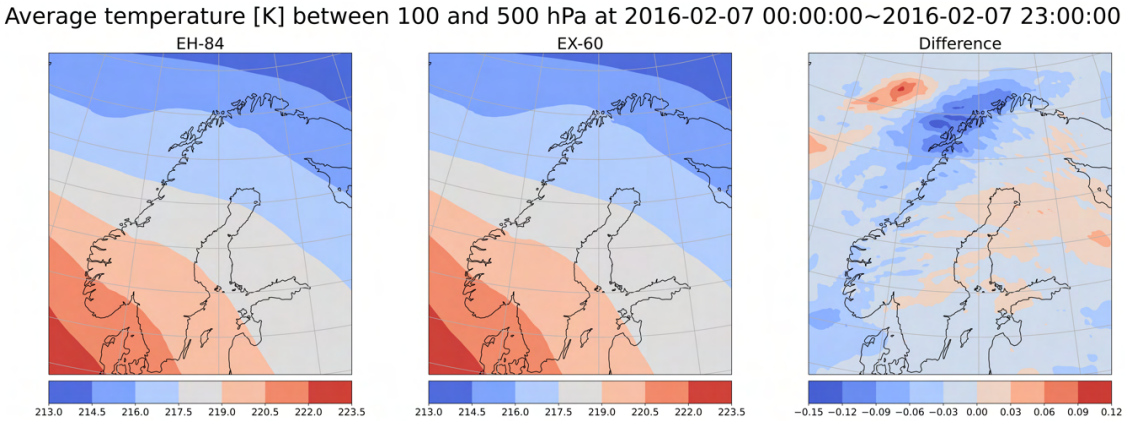

Figure S5. Daily average temperature between 100 and 500 hPa at 2016-02-07 for EH-84 (left), EX-60 (middle) and the difference (right).

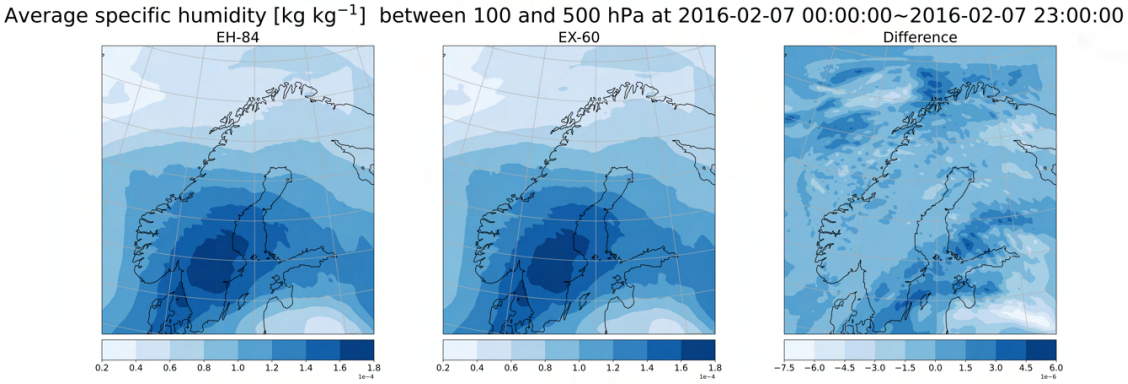

Figure S6. The daily average specific humidity between 100 and 500 hPa at 2016-02-07 for EH-84 (left), EX-60 (middle) and the difference (right).

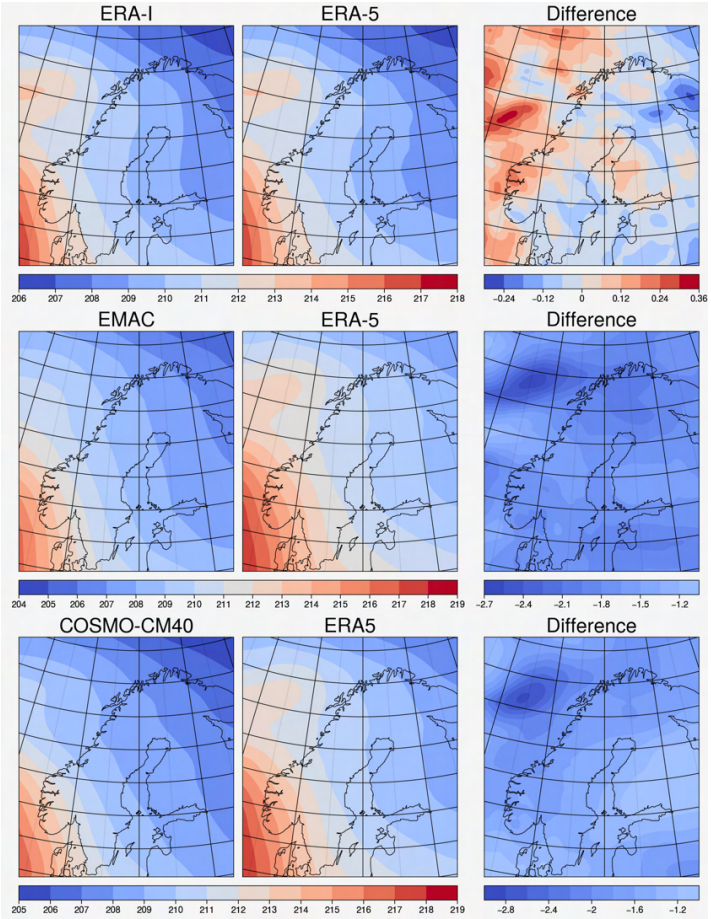

Figure S7. The comparison with ERA-5 of the daily average temperature (K) between 100 and 350 hPa at 2016-02-07 for ERA-I (top), EMAC (middle) and COSMO-CM40 (bottom).

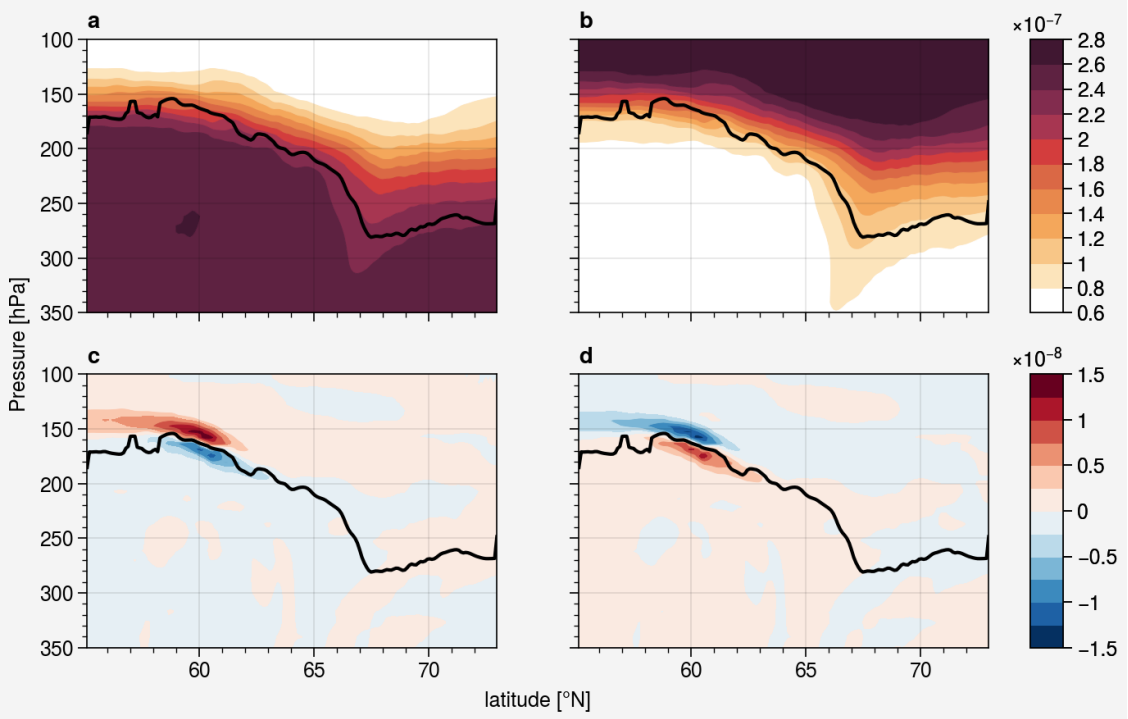

Figure S8. Cross section of distribution (a) N2O-like tracers (mol/mol), (b) Inverted N2O-like tracers (mol/mol); difference (vdiff on - off) (c) N2O-like tracers (mol/mol), (d)Inverted N2O-like tracers (mol/mol) at 2016-02-05 18:00.

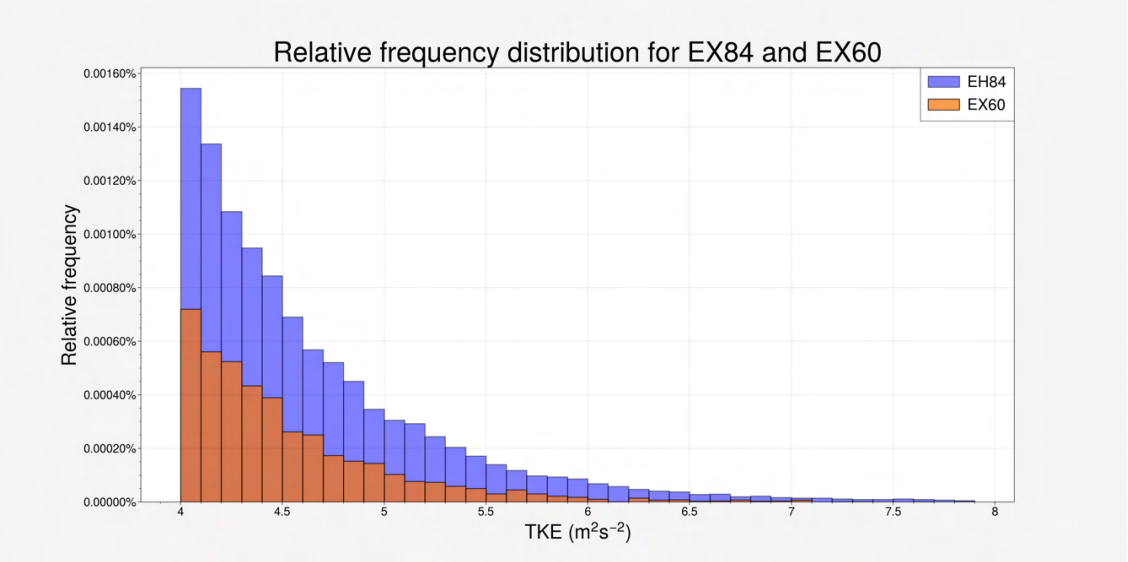

Figure S9. Relative frequency distribution of high TKE value for EH84 (blue) and EX60 (orange)

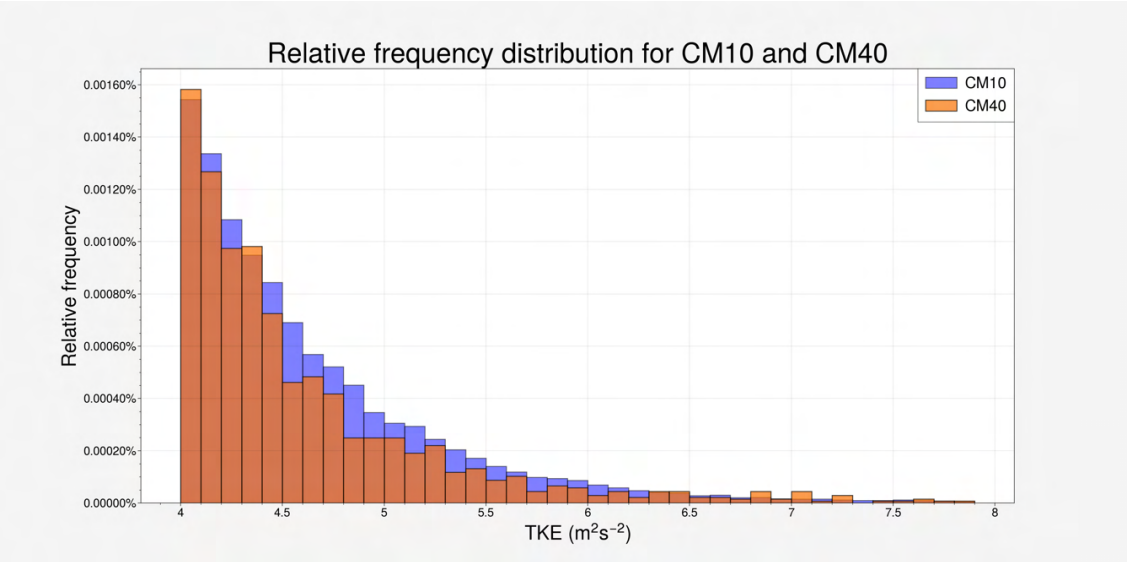

Figure S10. Relative frequency distribution of high TKE value for CM10 (blue) and CM40 (orange).

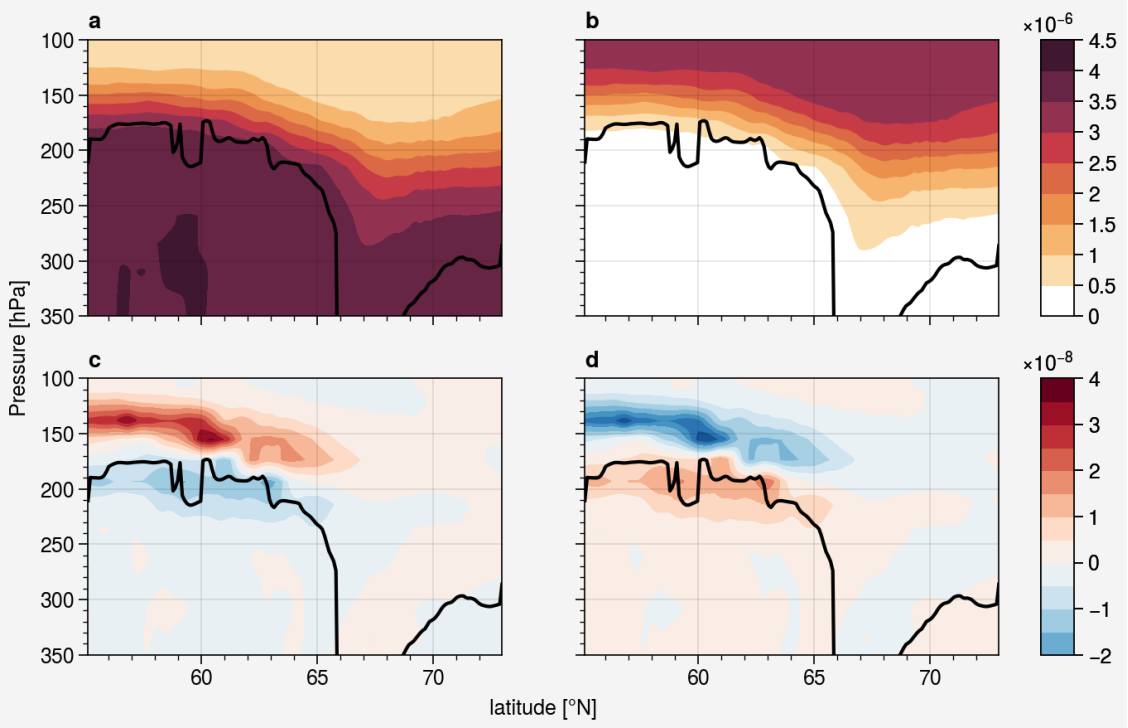

Figure S11. Cross section of distribution for EX60 (a) Inverted O3-like tracers (mol/mol), (b) O3-like tracers (mol/mol); the difference (vdiff on - off) (c) Inverted O3-like tracers (mol/mol), (d)O3-like tracers (mol/mol) at 2016-02-05 18:00.

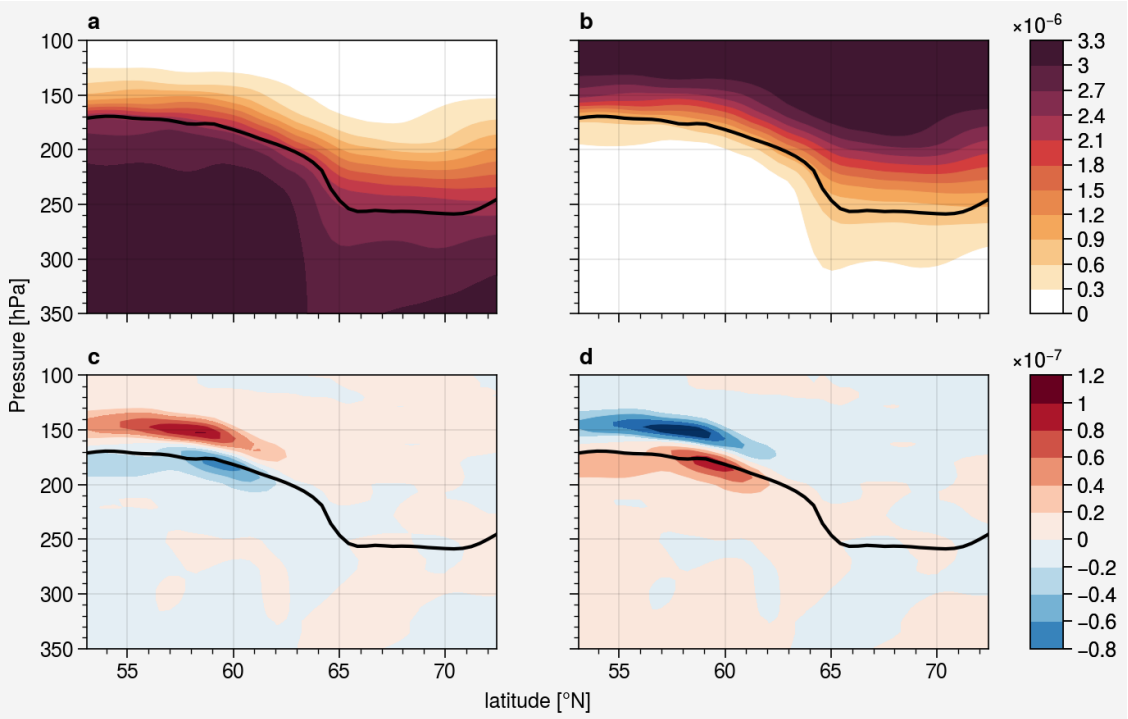

Figure S12. Cross section of distribution for CM40 (a) Inverted O3-like tracers (mol/mol), (b) O3-like tracers (mol/mol); the difference (vdiff on - off) (c) Inverted O3-like tracers (mol/mol), (d)O3-like tracers (mol/mol) at 2016-02-05 18:00.

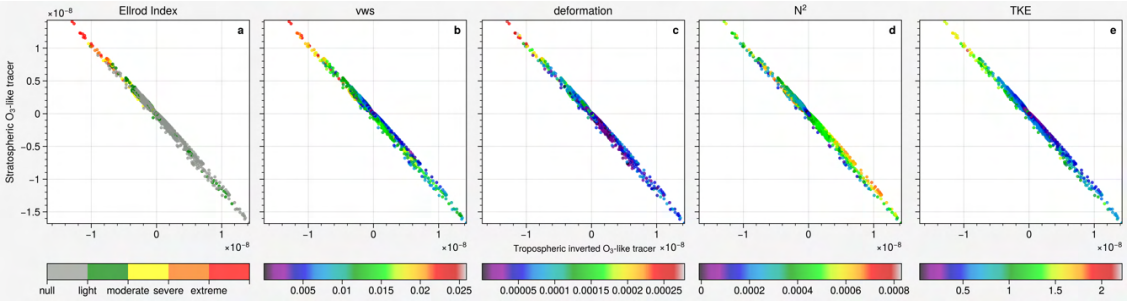

Figure S13. Delta tracer-tracer correlation of stratospheric inverted N2O-like/tropospheric N2O-like tracers (mol/mol) color-coded with (a) Ellrod Index(s^{-2}), (b) vertical wind shear (s^{-1}), (c) deformation (s^{-1}), (d) Brunt–Väisälä frequency (s^{-2}) and (e) turbulence kinetic energy $(m^2 s^{-2})$ at 2016-02-05 18:00.

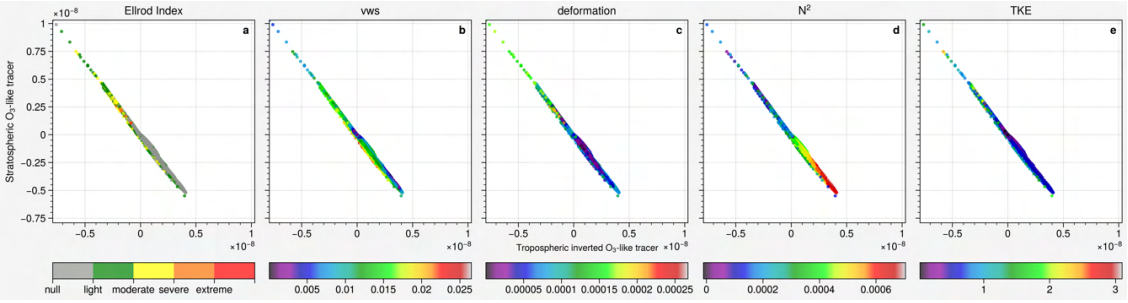

Figure S14. Delta tracer-tracer correlation of stratospheric inverted N2O-like/tropospheric N2O-like tracers (mol/mol) color-coded with (a) Ellrod Index(s^{-2}), (b) vertical wind shear (s^{-1}), (c) deformation (s^{-1}), (d) Brunt–Väisälä frequency (s^{-2}) and (e) turbulence kinetic energy $(m^2\,s^{-2})$ at 2016-02-05 05:00.

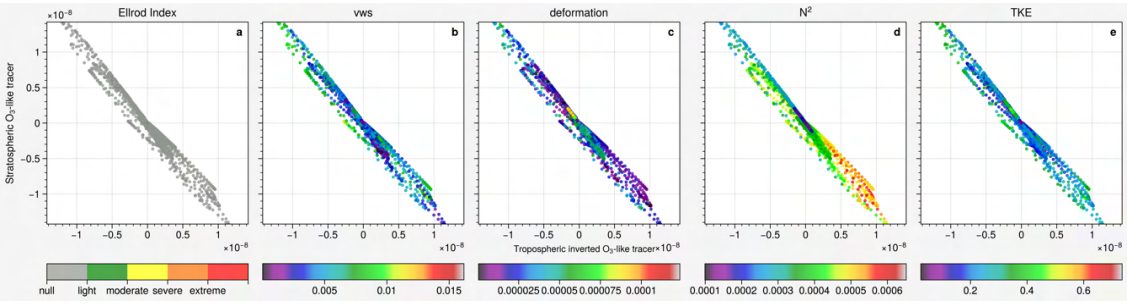

Figure S15. Delta tracer-tracer correlation of stratospheric inverted N2O-like/tropospheric N2O-like tracers (mol/mol) color-coded with (a) Ellrod Index(s^{-2}), (b) vertical wind shear (s^{-1}), (c) deformation (s^{-1}), (d) Brunt–Väisälä frequency (s^{-2}) and (e) turbulence kinetic energy $(m^2\,s^{-2})$ at 2016-02-03 22:00.

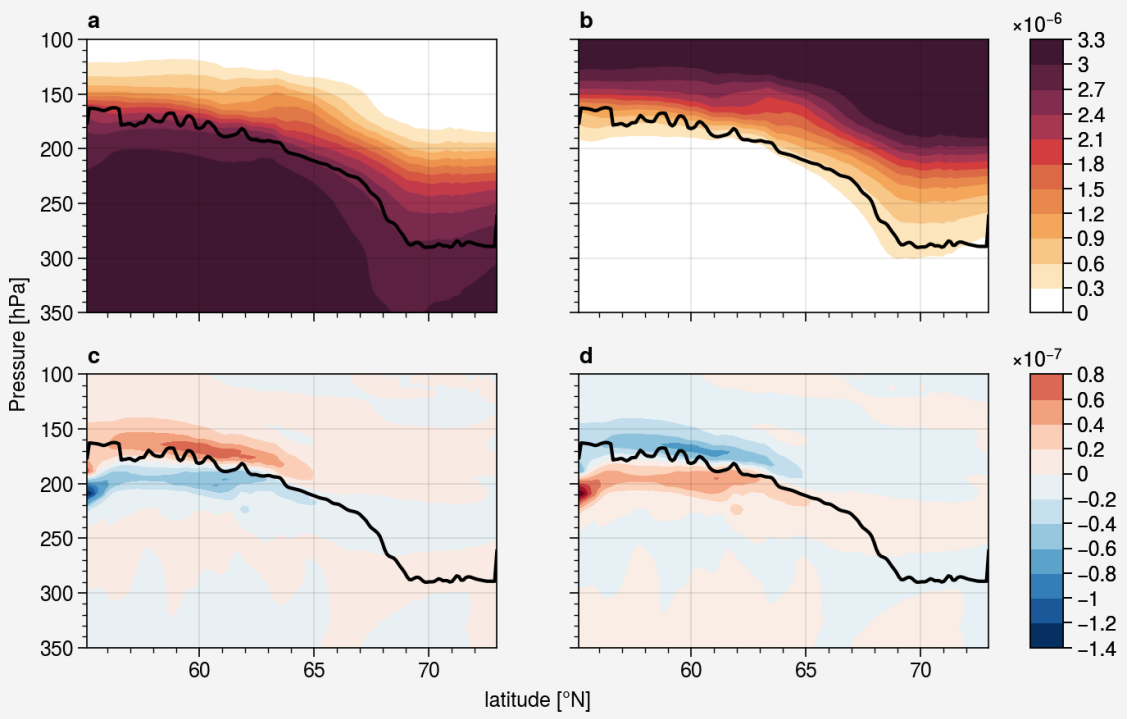

Figure S16. Cross section of distribution for Case 2 (a) Inverted O3-like tracers (mol/mol), (b) O3-like tracers (mol/mol); the difference (vdiff on - off) (c) Inverted O3-like tracers (mol/mol), (d)O3-like tracers (mol/mol).

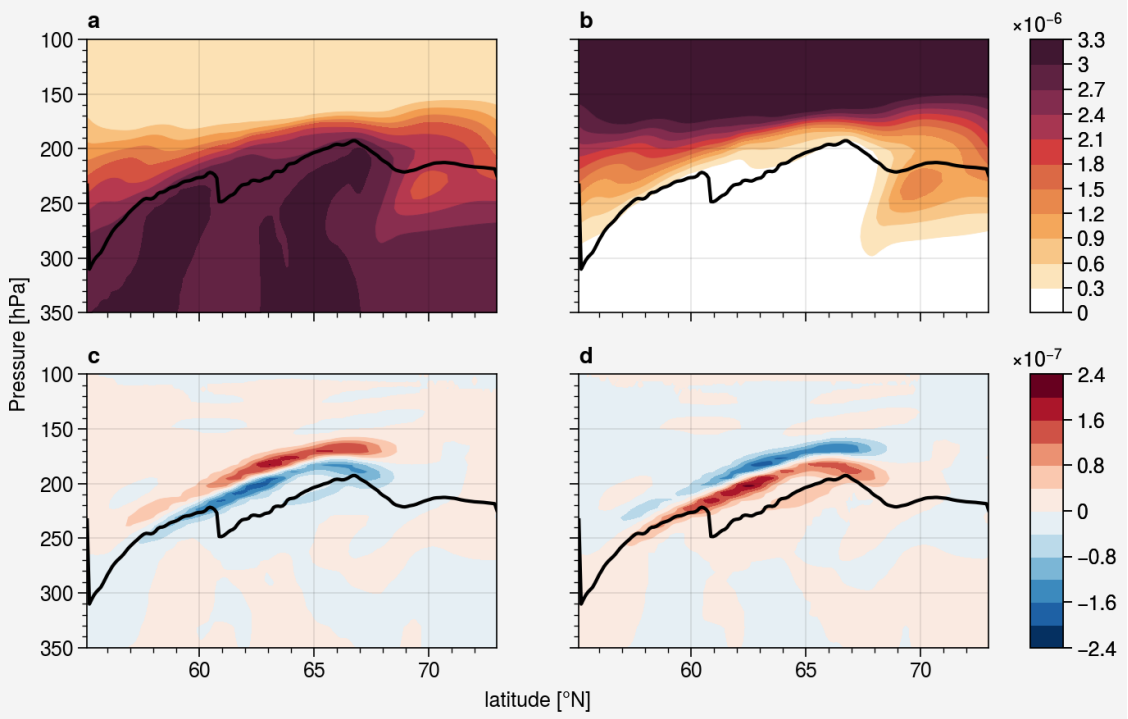

Figure S17. Cross section of distribution for Case 3 (a) Inverted O3-like tracers (mol/mol), (b) O3-like tracers (mol/mol); the difference (vdiff on - off) (c) Inverted O3-like tracers (mol/mol), (d)O3-like tracers (mol/mol).

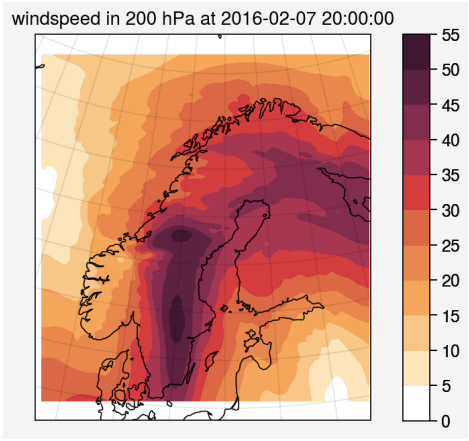

Figure S18. Horizontal wind speed (m/s) at 200 hPa at 2016-02-07 20:00 for CM10.

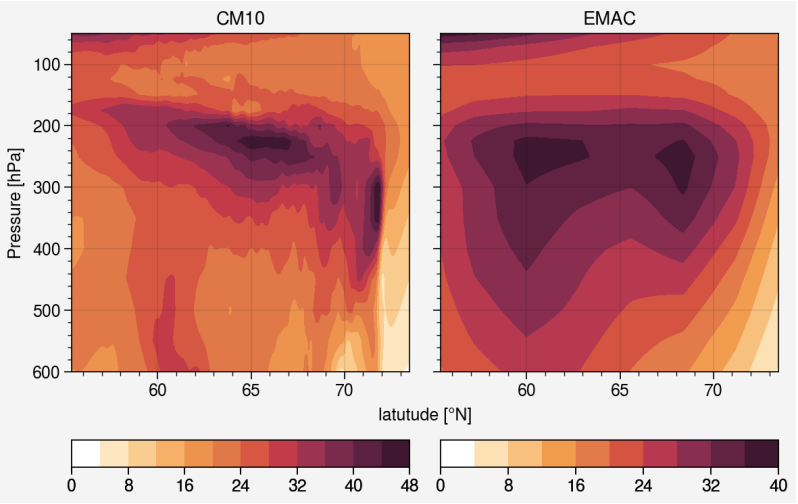

Figure S19. Cross section of horizontal wind (m/s) at 2016-02-07 20:00 for (a) CM10, (b) EMAC

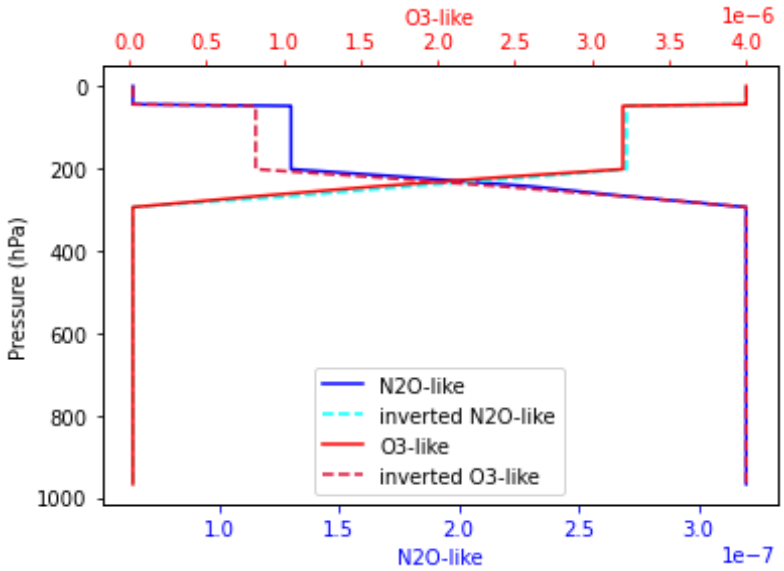

Figure S20. Vertical profile of the tracer N2O-like (mol/mol), inverted N2O-like (mol/mol), O3-like (mol/mol) and inverted O3-like tracer (mol/mol).

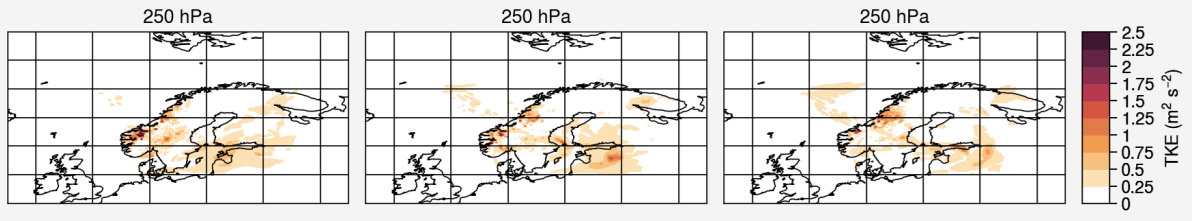

Figure S21. Modeled TKE at 250 hPa for CM10 at 2016-02-03 11:00(left), 18:00 (middle) and 22:00 (right).

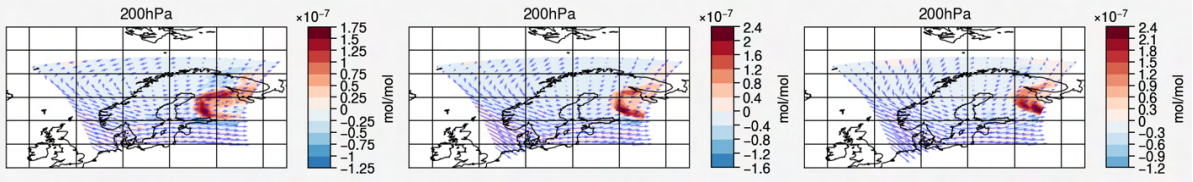

Figure S22. O3-like tracers difference(vdiff on - off) at 200 hPa at 2016-02-03 11:00(left), 18:00 (middle) and 22:00 (right), the blue arrow indicates the wind direction and wind speed.

3.2 Parametrizing Clear Air Turbulence in Climate Chemistry model EMAC and its potential impacts on modifying UTLS composition and corresponding radiative impact

This chapter has been submitted to the journal Atmospheric Chemistry and Physics as a research article and is under review. I am the first author of this paper, where I designed and performed the simulations, analysed the data, generated the figures, contributed to the code development and wrote the manuscript. The co-authors contributed to discussing the results, proofreading the manuscript, and developing the original code. Detailed author contributions can be found at the end of the paper in the section Author contributions.

How to cite: Chau, C. H., Hoor, P., Kaiser, K., and Tost, H.: Parametrizing the mixing by clear air turbulence in the chemistry climate model EMAC and its respective radiative impact, EGUsphere [preprint], https://doi.org/10.5194/egusphere-2025-5382, 2025a.

Submitted: 30 October 2025

https://doi.org/10.5194/egusphere-2025-5382
Preprint. Discussion started: 12 November 2025

Parametrizing the mixing by clear air turbulence in the chemistry climate model EMAC and its respective radiative impact

Chun Hang Chau[1], Peter Hoor[1], Katharina Kaiser[2], and Holger Tost[1]

[1]Institute for Atmospheric Physics, Johannes Gutenberg University Mainz, Mainz, Germany
[2]Aerosol Chemistry Department, Max Planck Institute for Chemistry, Mainz, Germany

Correspondence: Chun Hang Chau (cchau@uni-mainz.de)

Abstract. The Earth's radiation budget is found to be sensitive to changes in the upper troposphere and lower stratosphere (UTLS) chemical composition. Stratosphere-troposphere exchange is the major process that influences the UTLS chemical composition with remaining uncertainties in current climate-chemistry models. This exchange could be e.g., facilitated by clear air turbulence (CAT), as it leads to diabatic mixing of chemical tracers between stratosphere and troposphere. In this work, we examine the sensitivity of vertical mixing by CAT on the UTLS chemical composition and its corresponding radiative impact by implementing a newly developed submodel parametrizing turbulent mixing in the free troposphere and stratosphere within the climate chemistry model EMAC. This submodel parametrizes the vertical mixing by CAT based on a newly introduced turbulence diagnostic MoCATI. MoCATI shows a comparable performance with the well-established Ellrod-Knox index. Simulations are conducted with EMAC-QCTM to examine the sole impact of mixing, without taking the potential feedback into account. Results show that the radiatively active ozone in the UTLS is most sensitive to the vertical mixing of CAT and is significantly reduced by 10 to 20% by the CAT submodel. This modification is not a pure result of the physical mixing but also the chemical feedback of other modified tracers. The tracer mixing through CAT also changes the atmospheric chemistry by shortening the CH_4 lifetime and changing the O_3 becoming relatively sensitive to NO_x. It also leads to potential surface radiative heating and radiative cooling at the top of the atmosphere. The global average radiative effect is about -0.2 W/m^2.

1 Introduction

The upper troposphere and lower stratosphere (UTLS) plays a crucial role on the Earth's radiation budget (Forster et al., 2021). Changes in the chemical composition in the UTLS could lead to changes via the radiation locally as well as at the surface. Ozone and water vapour near the tropopause are found to have more radiative influence on the surface compared to other well-mixed greenhouse gases (Riese et al., 2012; Lacis et al., 1990). Removal of ozone above the tropopause could lead to local cooling (Randel et al., 2007). The surface temperature is also highly sensitive to changing ozone concentration in the UTLS, increasing ozone in this region could increase the surface temperature (Forster and Shine, 1997; Lacis et al., 1990). Water vapour also has complex impacts on the Earth's radiation. Increasing stratospheric water vapour could lead to local cooling (Forster and Shine, 1999; Randel et al., 2007) and surface warming (Solomon et al., 2010).

https://doi.org/10.5194/egusphere-2025-5382
Preprint. Discussion started: 12 November 2025

Since stratosphere-troposphere exchange (STE) is one of the major processes that influence the UTLS chemical composition (Holton et al., 1995; Stohl et al., 2003), it is crucial to improve the representation of STE in the model. Previous studies show that the simulated upper tropospheric ozone budget depends on the model representation of STE (Stevenson et al., 2006). A key feature for STE is the occurrence of vertical shear, which has been recently identified constituting a layer of high probability of shear occurrence around the local tropopause (Kaluza et al., 2021). Vertical shear is a key mechanism to initiate turbulence and thus mixing. Turbulent mixing in the UTLS is one of the pathways of the STE (Holton et al., 1995) and it is not represented in several state-of-the-art chemistry climate models, such as EMAC (Jöckel et al., 2016). In ECHAM5, the base model of EMAC, the turbulence scheme was designed for the surface boundary layer only; it sets a constant asymptotic mixing length in the boundary layer and simply assumes it decreases exponentially with height, approaching 1 m in the lower stratosphere (Roeckner et al., 2003), resulting in a dampening effect on the turbulence in the UTLS, which normally does not mix tracers significantly. Therefore, this study presents a parametrization of tracer mixing by clear air turbulence (CAT), which is commonly found in the UTLS and could lead to rapid mixing of the chemical composition between the troposphere and stratosphere (Dutton and Panofsky, 1970; Esler and Polvani, 2004; Traub and Lelieveld, 2003), for EMAC.

CAT represents the turbulence in the free atmosphere that occurs in a cloud-free region (Ellrod et al., 2003). Kelvin-Helmholtz instability, which is a result of vertical wind shear (Kunkel et al., 2019), is the major mechanism that leads to CAT formation (Watkins and Browning, 1973; Ellrod and Knapp, 1992). Considering turbulence is not explicitly represented by global scale numerical models, CAT is usually forecast using diagnostics that are based on related larger-scale mechanisms. A previous study has shown that turbulence diagnostics are reliable for forecasting CAT operationally in NWP models (Sharman et al., 2006). However, each of the turbulence diagnostics has its own advantages and disadvantages. Ellrod index (TI) is one of the most commonly used CAT diagnostics in the aviation sector. It is based on the meso-scale condition that leads to CAT including vertical wind shear and deformation of the horizontal wind (Ellrod and Knapp, 1992). The Ellrod-Knox index is the improved version of the TI by introducing an additional divergence trend term (Ellrod and Knox, 2010). Williams and Storer (2022) confirmed that turbulence diagnostics are capable of diagnosing CAT and its response to climate change in climate models with coarser resolution. Another recent study from Chau et al. (2025) shows that the turbulence diagnostic calculated from the grid scale wind field matches well with a detailed sub-grid scale turbulence scheme in the UTLS for a regional forecast model.

CAT is expected to become more frequent and intense under climate change because of the more sheared atmosphere (Williams, 2017). The vertical wind shear in the North Atlantic region has increased by 15% between 1979 and 2017 (Lee et al., 2019). Several studies show that the strength of CAT will be stronger in the North Atlantic and East Asia under different climate change scenarios (Williams and Joshi, 2013; Smith et al., 2023; Hu et al., 2021). Therefore, there is a necessity to study how CAT could potentially change the atmosphere. Previous studies have examined the sensitivity of the vertical mixing in a Lagrangian approach, concluding that water vapour and ozone are most sensitive to vertical mixing and lead to a significant impact on the radiation budget (Riese et al., 2012). The main objective of this study is to examine the sensitivity of vertical turbulent mixing on the UTLS chemistry and radiation in an Eulerian approach. For this purpose, we introduce a new MESSy submodel to parametrize the CAT-induced vertical mixing of tracers in the UTLS. We demonstrate the possibility

https://doi.org/10.5194/egusphere-2025-5382
Preprint. Discussion started: 12 November 2025

of parametrizing CAT mixing based on turbulence indices. In order to examine the sole impact of CAT but not its feedback, the simulations are conducted in a QCTM mode (Deckert et al., 2011) to ensure identical model dynamics independent of the chemical composition.

This paper consists of three further sections after the introduction: Section 2 introduces the EMAC model configuration and the newly developed CAT submodel. Section 3 presents the results and discusses the CAT submodel in terms of redistributing chemical composition and radiative impact. Section 4 summarises the findings and draws conclusions with a future outlook.

2 Method

2.1 EMAC Model Description

EMAC (ECHAM/MESSy Atmospheric Chemistry; Jöckel et al., 2006; Jöckel et al., 2010) is a state-of-the-art chemistry climate model that allows flexible model configuration via different submodels. It combines the general circulation model ECHAM5 (Roeckner et al., 2003) with the Modular Earth Submodel System (MESSy; Jöckel et al.,2005) which allows users to include different physical and chemical processes via a namelist interface. EMAC is also able to operate in quasi chemistry-transport model mode (QCTM; Deckert et al.,2011), which allows decoupling between chemistry and dynamics in the model, suppressing the feedback between chemistry and dynamics to better quantify the signal from a particular process. For our study, EMAC is operated in T42L90MA resolution (Giorgetta et al., 2006). It is a configuration designed for the middle atmosphere with a horizontal resolution of T42 (approximately 2.8°× 2.8°) and 90 vertical hybrid pressure levels up to 0.01 hPa.

2.2 Experimental setup

Two simulations: QCTM-MIX and QCTM-NOMIX are performed in this work. Two decadal simulations with gas-phase chemistry are performed using the EMAC-QCTM to examine the long-term impact of the CAT submodel without the dynamical feedback from chemistry. Both simulations are performed with the perpetual year of 2014 for 10 years, prescribing the emission, sea surface temperature and sea ice concentration of 2014 repetitively. The chemistry setup is adapted from the RC1-base-07 of Jöckel et al. (2016), which is the Ref-C1 of the CCMI (Eyring et al., 2013). The emissions are prescribed by the CCMI-2022 Ref-D1 (Plummer et al., 2021), which is a historical hindcast. The sea surface temperature and sea ice concentration are prescribed by the AMIP-II data set (Taylor et al., 2000). Both simulations are initialized with the ERA-Interim reanalysis data (Dee et al., 2011).

QCTM-NOMIX with the CAT submodel disabled is used as a reference simulation, while the QCTM-MIX enables the CAT submodel to examine the impact of the CAT tracer mixing. The details for the CAT submodel are discussed in Section 2.3.

2.2.1 Radiation (RAD) submodel of EMAC

In EMAC, the radiation scheme (RAD) is a re-implementation of the ECHAM5/ECHAM6 radiation codes with more flexibility (Dietmüller et al., 2016). It calculates the radiation depending on radiatively active tracers, including CO_2, CH_4, O_3, N_2O,

https://doi.org/10.5194/egusphere-2025-5382
Preprint. Discussion started: 12 November 2025

CFC-11 and CFC-12. It also requires input parameters like water vapour, cloud cover, clear-sky index, cloud optical properties, aerosol optical properties, and orbital parameters provided by the model. RAD allows for both online and offline radiation calculations, i.e., using either prognostic variables (tracers) or external data sources for the radiatively active species. To run EMAC in the QCTM mode, climatological values or distributions of the radiatively active gases are utilised for the radiation calculation to decouple the feedback between the gases and the radiation scheme. Water vapour also needs to be decoupled from the chemistry to prevent inconsistency in model dynamics. Therefore, the mixing scheme of the new submodel CAT (Section 2.3) does not include water vapour at this stage. RAD also provides an option to calculate the radiative disturbances from different sets of radiatively active gases by calling the radiation routine multiple times within one model time step. The temperature feedback will be provided by the first call. This option provides an opportunity to examine the pure radiative impact of the CAT mixing without dynamical feedback within EMAC-QCTM. In both simulations, a total of six calls are set. For the first call, which provides the temperature feedback of the model, prescribed values for the radiatively active gases are used. For the second call, the radiation calculation uses all the online interactive chemistry output provided by EMAC. To isolate the individual contribution of each gas, four additional radiation calls are set. In each call, only the specified gas uses the online output from the model, the other gases remain unchanged using the prescribed values. Detailed information about the applied values and the dataset is given in Table1. The prescribed values for CO_2, CH_4, N_2O , CFC-11 and CFC-12 are provided by the Global Monitoring Laboratory of NOAA. The prescribed O_3 is taken from the climatology of Paul et al. (1998).

Table 1. Summary of the performed radiation calls and the applied values [mol/mol] for the active tracers

Call no.	CO_2	O_3	CH_4	N_2O	CFC-11	CFC-12
RAD01	397.34e-6	(Paul et al., 1998)	1.82254e-6	327.09e-9	230e-12	520e-12
RAD02	interactive	interactive	interactive	interactive	interactive	interactive
RAD03 (O_3)	397.34e-6	interactive	1.82254e-6	327.09e-9	230e-12	520e-12
RAD04 (CO_2)	interactive	(Paul et al., 1998)	1.82254e-6	327.09e-9	230e-12	520e-12
RAD05 (CH_4)	397.34e-6	(Paul et al., 1998)	interactive	327.09e-9	230e-12	520e-12
RAD06 (N_2O)	397.34e-6	(Paul et al., 1998)	1.82254e-6	interactive	230e-12	520e-12

2.3 New MESSy submodel CAT for clear air turbulence mixing

This section introduces the newly developed submodel CAT of MESSy. The new CAT submodel is developed to parametrize the vertical mixing of tracers caused by clear air turbulence in the UTLS. It allows vertical mixing of tracers based on a 2-layer mixing algorithm between 500 hPa to 70 hPa, considering that CAT occurs most frequently in the UTLS (Dutton and Panofsky, 1970). The mixing scheme of CAT uses a turbulence diagnostic (CAT Index) to serve as a mixing coefficient and provides two options for now: the Ellrod-Knox index (Ellrod and Knox, 2010) and a newly introduced Modified CAT Index (MoCATI). The Ellrod-Knox index is a widely tested and used turbulence diagnostic, which is based on the grid scale wind field data including

https://doi.org/10.5194/egusphere-2025-5382
Preprint. Discussion started: 12 November 2025

deformation (DEF), vertical wind shear (VWS), and divergence trend (DVT):

$$\text{Ellrod-Knox index} = \underbrace{\left[\left(\frac{\partial u}{\partial x}-\frac{\partial v}{\partial y}\right)^2+\left(\frac{\partial v}{\partial x}+\frac{\partial u}{\partial y}\right)^2\right]^{\frac{1}{2}}}_{\text{DEF}} \cdot \underbrace{\left(\left|\frac{\partial u}{\partial z}\right|^2+\left|\frac{\partial v}{\partial z}\right|^2\right)^{\frac{1}{2}}}_{\text{VWS}} + \underbrace{C\left[\left(\frac{\partial u}{\partial x}+\frac{\partial v}{\partial y}\right)_{h2}-\left(\frac{\partial u}{\partial x}+\frac{\partial v}{\partial y}\right)_{h1}\right]}_{\text{DVT}} \quad (1)$$

The subscripts h1 and h2 represent the selected time interval for the divergence trend. C is a weighting constant to prevent the divergence trend term from dominating the whole Ellord-Knox index.

MoCATI is developed on top of the Ellrod-Knox index. It is a modification of the Ellrod-Knox index including static stability:

$$\text{MoCATI} = \frac{N_{lim}^2 - N^2}{N_{lim}^2} \cdot \text{Ellrod-Knox index} \quad (2)$$

The N^2 is the Brunt-Väisälä frequency and N_{lim}^2 is a limitation threshold to modify the whole stability term, considering that a stable environment will suppress the formation of turbulence. In addition, the mixing will be switched off above the N_{lim}^2.

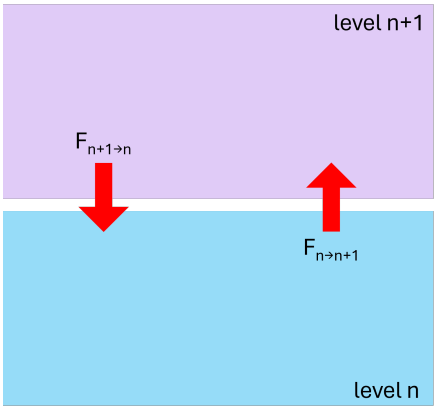

Figure 1. Schematic of the tracer mixing algorithm of the CAT submodel. F represents the flux of mixing and n represents the model vertical level.

A schematic of the tracer mixing algorithm is shown in Figure 1. The flux of the mixing between level n and level $n+1$ depends on the mixing ratio (χ) and the CAT index at the boundary of both layers. The flux from level n to $n+1$ can be express as:

$$F_{n \to n+1} = \chi \cdot \text{CAT Index}_{boundary} \quad (3)$$

https://doi.org/10.5194/egusphere-2025-5382
Preprint. Discussion started: 12 November 2025

The CAT index at the boundary can be calculated by:

$$\text{CAT Index}_{boundary} = \frac{\text{CAT Index}_n + \text{CAT Index}_{n+1}}{2} \cdot \frac{\Delta t}{t_{norm}} \tag{4}$$

The Δt is the time step length and the t_{norm} is a time normalization factor. The whole term is used to moderate the strength of mixing.

The CAT submodel allows changes in different parameters via a simple namelist, for which an example and the detailed explanation of the respective parameters can be found in the electronic supplement.

3 Results and Discussion

3.1 Evaluation of the newly introduced MoCATI

In order to examine the validity of the MoCATI, we performed statistical tests and calculated the relative frequency distribution of the turbulence diagnostics following the approch of Kaluza et al. (2022), using the ERA5 data for three boreal winters (DJF) from December 2016 to February 2019 over the North Atlantic to calculate and compare the distribution between the well-established Ellrod-Knox index and the MoCATI, but instead of just covering the flight tracks as in Kaluza et al. (2022), we perform calculations on the whole North Atlantic. The North Atlantic winter is found to have the most vertical wind shear (Kaluza et al., 2021). Figure 2 shows a map of the domain from 60° W to 0° W and 35° N to 60° N for the Ellrod-Knox index and MoCATI at the lapse rate tropopause on 01 December 2016. Both indices show a similar distribution, although the magnitude of MoCATI is weaker considering it is constrained by the additional stability term. Figure 3 shows the Taylor diagram using the Ellrod-Knox index as a reference. It shows the correlation coefficient, normalized standard deviation and the normalized root-mean squared difference (both normalized with the reference standard deviation from the Ellrod-Knox index). As expected, the MoCATI shows a similar behaviour on these statistical metrics since it is a modification of the Ellrod-Knox index. The MoCATI is highly correlated, with a similar normalized standard deviation close to the perfect 1.0 line, and a small RMSD of half of the reference standard deviation. Figure 3 also includes the Ellrod index (TI), vertical wind shear (VWS) and deformation (DEF). Although the TI, VWS and DEF are included as part of the Ellrod-Knox index, since an additional divergence trend term is added, they show a lower correlation with the Ellrod-Knox index compared to the MoCATI. Figure 4 shows the relative frequency distribution of the ln(MoCATI) and ln(Ellrod-knox index) by geometric height and distance relative to the lapse rate tropopause. Both indices show a similar distribution, with a rightward shift (i.e., stronger turbulence) at lower altitudes and a leftward shift at higher altitudes. MoCATI has a more prominent leftward shift at higher altitudes considering the additional static stability term which constrains the index. We also perform a ROC (Receiver operating characteristic) analysis (Fawcett, 2006) to examine the performance of the Ellrod-Knox index and MoCATI using TI as the classification threshold (Sharman et al., 2006). Both indices show a similar performance under different thresholds (Figure 5). To conclude, the newly introduced MoCATI shows a comparable performance with the well-established Ellrod-Knox index, but takes the static stability into account, modifying the effective mixing under specific temperature profile conditions.

https://doi.org/10.5194/egusphere-2025-5382
Preprint. Discussion started: 12 November 2025

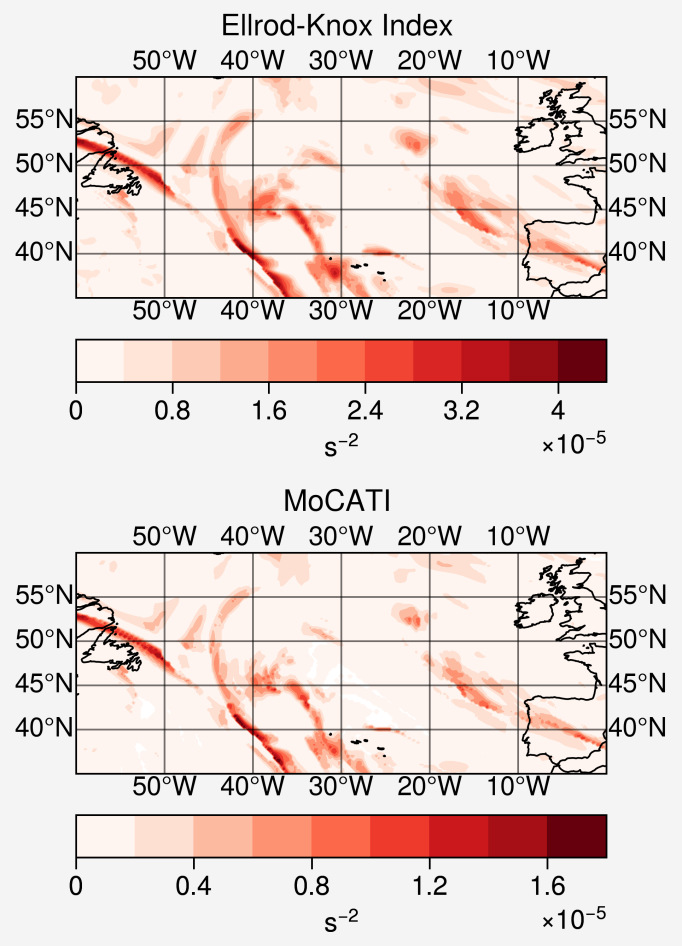

Figure 2. Map of the Ellrod-Knox index and MoCaTI at the lapse rate tropopause on 01 Dec 2016 1600 UTC.

https://doi.org/10.5194/egusphere-2025-5382
Preprint. Discussion started: 12 November 2025

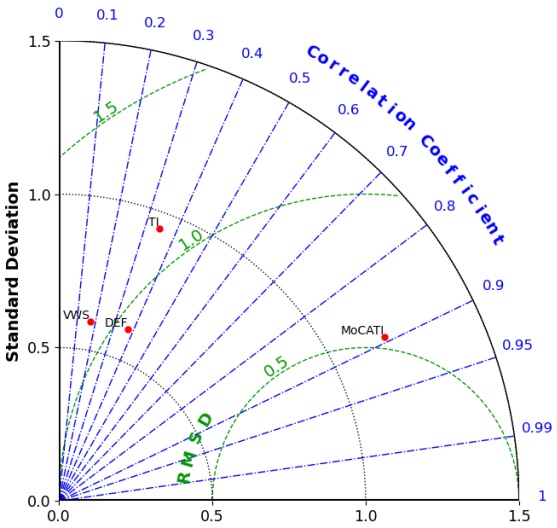

Figure 3. Taylor diagram showing the correlation coefficient, normalized standard deviation and normalized root mean square difference (RMSD) using the Ellrod-Knox index as reference.

https://doi.org/10.5194/egusphere-2025-5382
Preprint. Discussion started: 12 November 2025

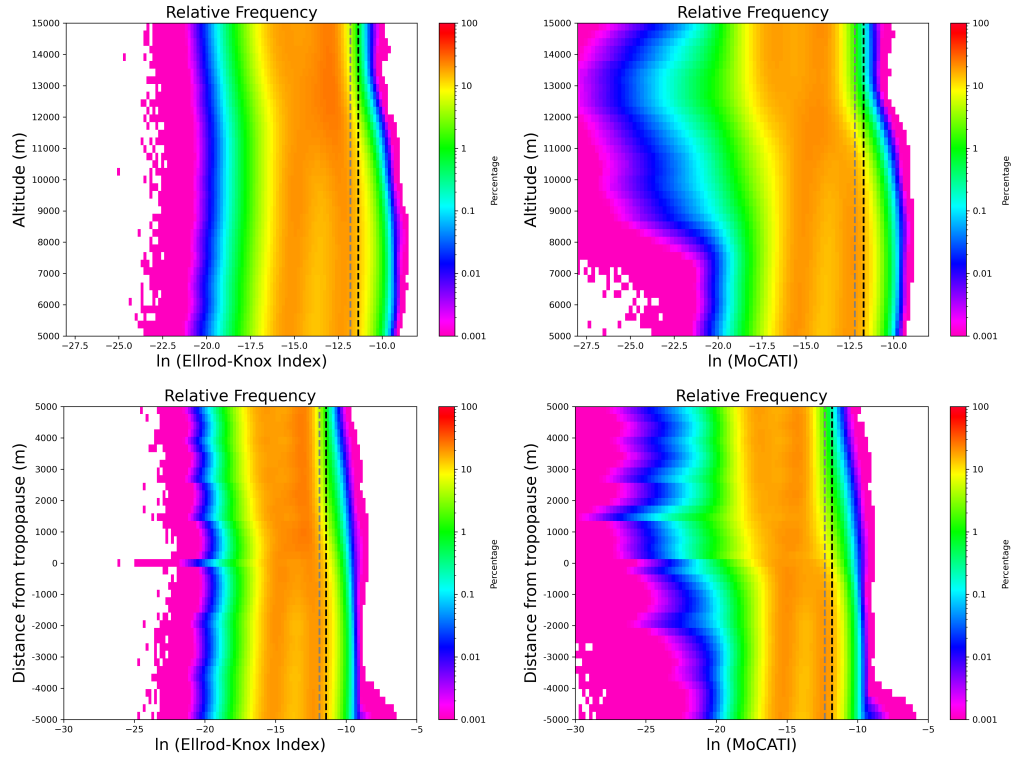

Figure 4. Relative frequency distribution for MoCATI (left) and Ellrod-Knox index (right) in geometric height (top) and relative to the lapse rate tropopause (bottom). Dashed lines indicate the 95th percentile (black) and 90th percentile (grey).

https://doi.org/10.5194/egusphere-2025-5382
Preprint. Discussion started: 12 November 2025

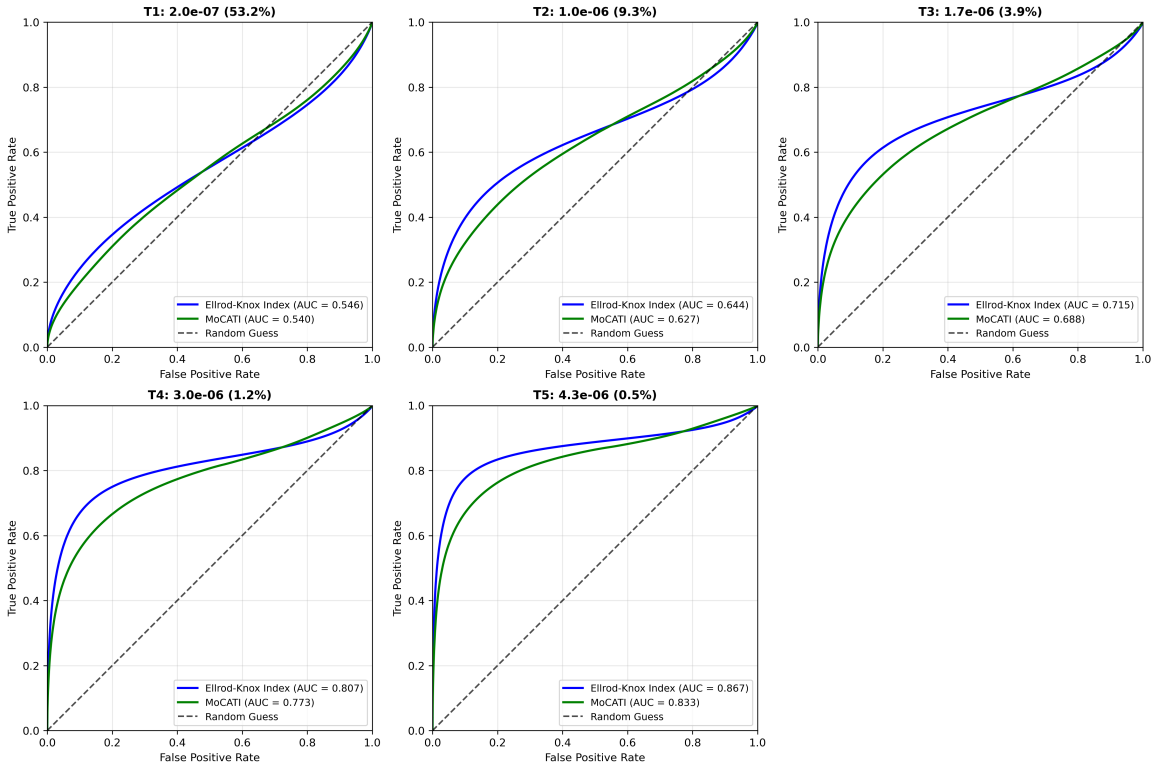

Figure 5. ROC curves showing the probability of false detection and true detection for Ellrod-Knox index and MoCATI using different TI as threshold: T1 = null, T2 = light, T3 = moderate, T4 = severe and T5 = extreme. The brackets represent the percentage of data that reaches the corresponding threshold. AUC represents the area under the curve.

https://doi.org/10.5194/egusphere-2025-5382
Preprint. Discussion started: 12 November 2025

3.2 Simulation results

3.2.1 Comparison of simulated O_3 with SWOOSH observations

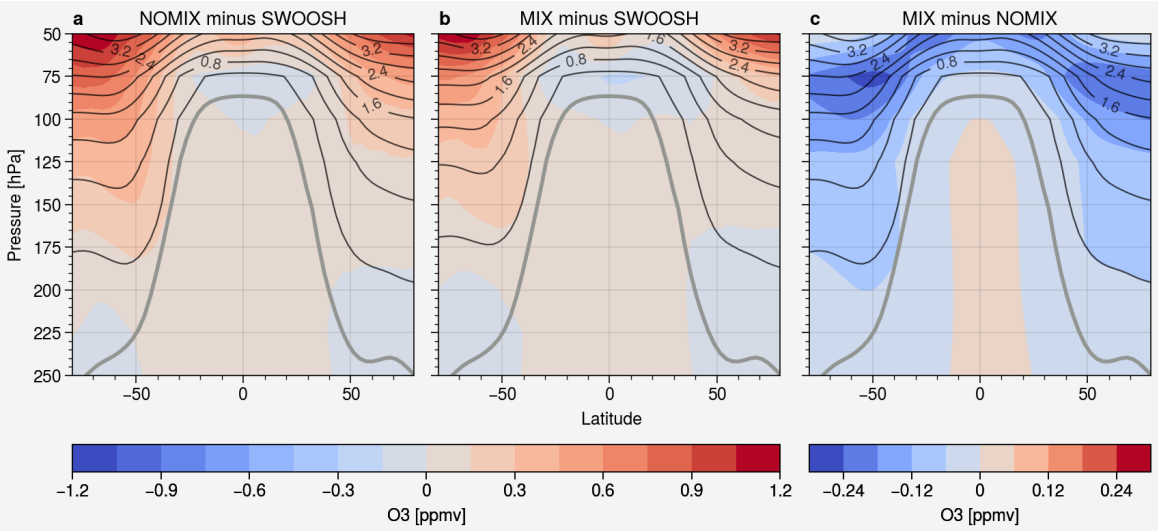

Figure 6. Cross section of the annual ozone zonal mean difference for (a) QCTM-NOMIX minus SWOOSH, (b) QCTM-MIX minus SWOOSH, and (c) QCTM-NOMIX minus QCTM-MIX. The contour lines represent the mixing ratio of O_3 in ppmv of the respective QCTM simulation.

Figure 6a and b show the annual mean difference of ozone between both simulations and the satellite-based database SWOOSH (Davis et al., 2016). By applying the CAT submodel, the overestimated ozone over the polar regions in the stratosphere is significantly reduced. Figure 6c shows the annual mean difference between both simulations. The vertical mixing by CAT in QCTM-MIX reduces the ozone significantly between 50 to 100 hPa compared to QCTM-NOMIX, the details are discussed further in Section 3.2.2. A previous study from Righi et al. (2015) shows that EMAC underestimates the ozone hole in Antarctica, causing a warm bias in the southern hemispheric stratosphere. QCTM-MIX shows a better consistency with SWOOSH in this region for ozone. As will be described later, Fig. 12 shows the annual mean difference in the net radiation between both simulations. The local cooling caused by the changes in ozone in this region might partly resolve the warm bias in this region. In order to clarify whether CAT could improve the representation of ozone in EMAC, a detailed investigation is needed. However, it is beyond the scope of this study.

https://doi.org/10.5194/egusphere-2025-5382
Preprint. Discussion started: 12 November 2025

3.2.2 Difference in tracer distributions

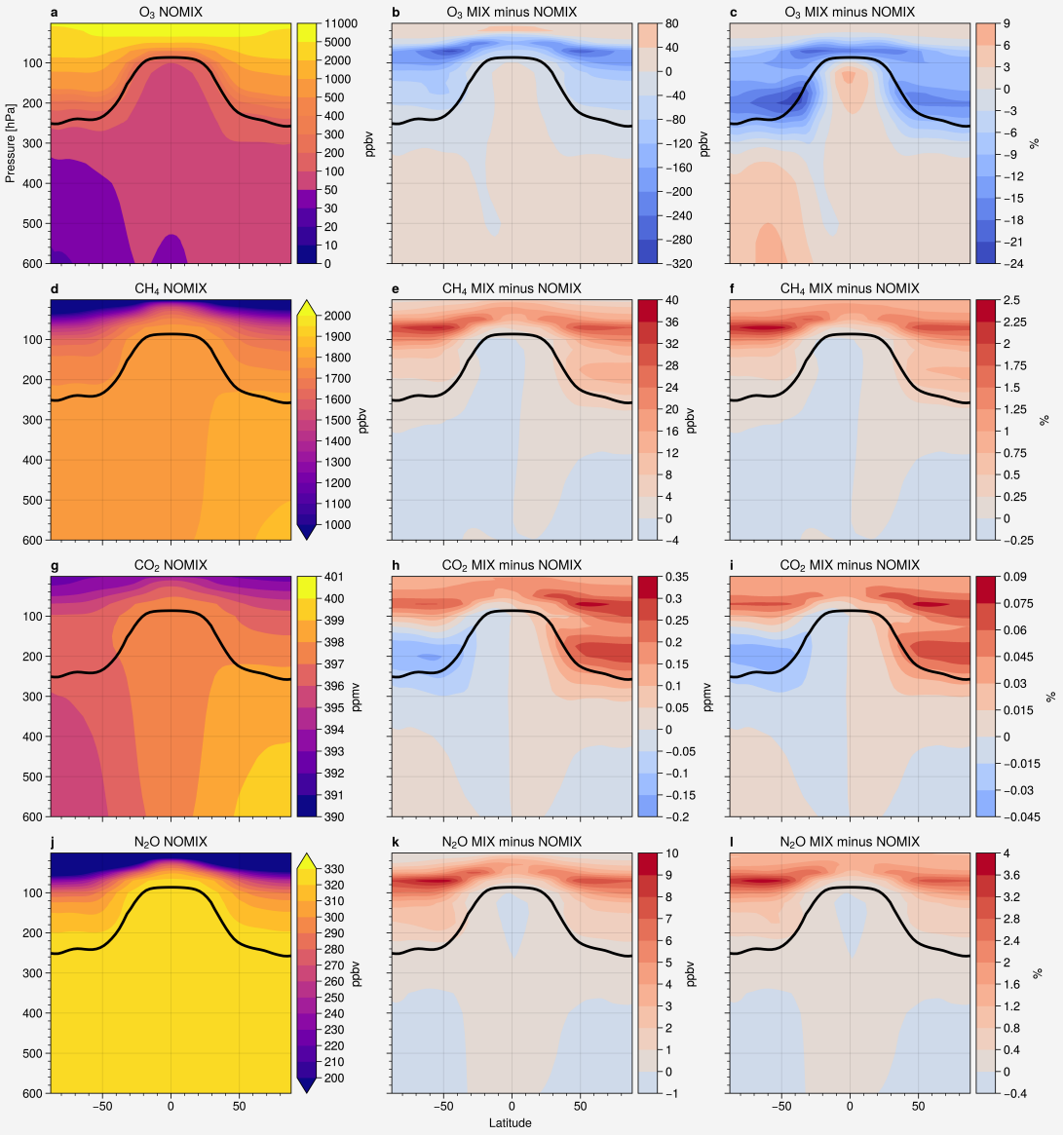

Figure 7. Annual zonal mean O_3, CH_4, CO_2 and N_2O profile of QCTM-NOMIX (first column), absolute difference between both simulations(centre column), and relative percentage difference (right column). The black line indicates the tropopause.

https://doi.org/10.5194/egusphere-2025-5382
Preprint. Discussion started: 12 November 2025

Figure 7 shows the annual zonal mean mixing ratio and difference of O_3, CH_4, CO_2 and N_2O between QCTM-MIX and QCTM-NOMIX to assess the sensitivity of tracers to the mixing algorithm of CAT. These major radiatively active gases were selected for the analysis to illustrate the different responses to CAT between spatially variable gases and well-mixed gases. As a result of enabling CAT, the O_3 in the UTLS is significantly reduced, especially in the vicinity of the tropopause with a 10 to 20% decrease (except below the tropical tropopause). The changes between 100 to 50 hPa at the extratropics could also be attributed to changes of the gradient by the enhanced vertical mixing at the tropics which leads to enhanced horizontal advection through the shallow branch of the Brewer-Dobson circulation. CAT also changed the O_3 by changing the chemistry (Figure 8a & b) in the upper stratosphere (above 50 hPa), causing up to 3% increase, and transport downward across the tropopause to the troposphere with maximum of 9% increase in the tropical upper troposphere and southern hemisphere. In terms of the mixing ratio, the largest absolute difference is located at around 75 hPa in the extratropical region, with up to 320 ppbv reduction of O_3. For CH_4, CAT leads to a significant increase in the UTLS up to 2.5% or 40 ppbv and a slight loss in the troposphere. The two gases exhibit an opposite behaviour with O_3 decreasing and CH_4 increasing in the UTLS since the O_3 mixing ratio is higher in the UTLS than in the troposphere whereas the CH_4 mixing ratio is higher in the troposphere. O_3 also has a more significant change compared to CH4 due to the steeper gradient. The changes in both gases are stronger in the southern hemisphere, potentially due to the stronger jet streams and fewer mountains, leading to a stronger vertical wind gradient. For CO_2, since it is well-mixed with a long atmospheric lifetime, the effect of mixing is comparatively weak, given the resulting low vertical gradient. In contrast to this, the effect of CAT mixing on the N_2O mixing ratio is slightly stronger, similar to CH_4, but with a more homogeneous effect on both hemispheres.

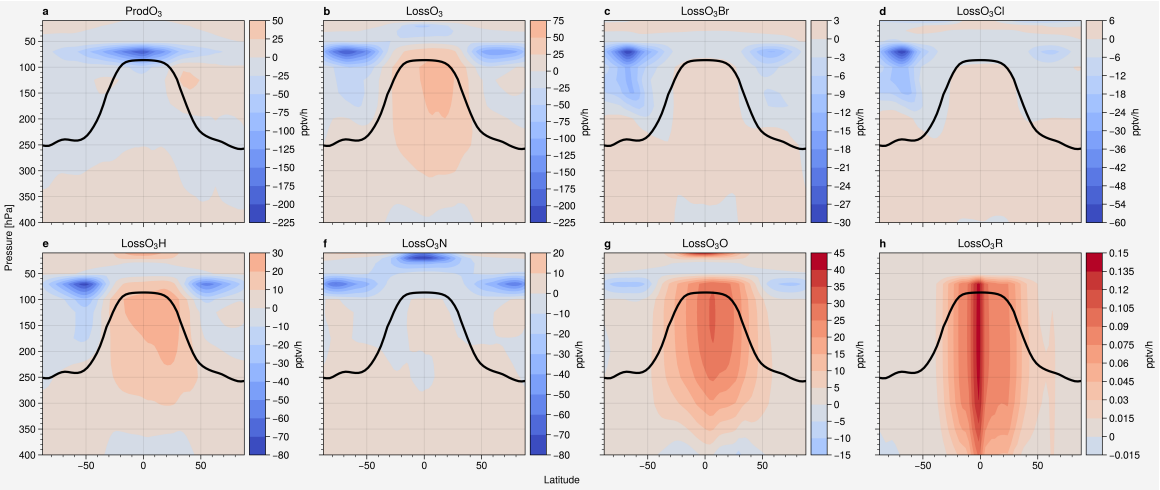

Figure 8. Annual zonal mean difference (MIX - NOMIX) of O_3 chemical production and chemical loss: (a) total production, (b) total loss, (c) loss by bromine, (d) loss by chlorine, (e) loss by hydrogen species, (f) loss by nitrogen species, (g) loss by atomic oxygen and (h) loss by peroxy radicals. The black line indicates the tropopause.

https://doi.org/10.5194/egusphere-2025-5382
Preprint. Discussion started: 12 November 2025

To examine whether the differences in the tracer distribution are attributed solely to the mixing of CAT or also influenced by the chemical feedback of other mixed tracers, we analyzed the chemical production and loss terms of ozone as well. The chemistry submodel MECCA (Sander et al., 2011) used in EMAC provided diagnostic output for some of the chemical species. Figure 8 shows the difference (MIX minus NOMIX) in ozone production, total loss and loss by species. With CAT mixing, the production of ozone (Figure 8a) is reduced and the loss is enhanced (Figure 8b) at the tropical tropopause, whereas the extra-tropical lower stratosphere (LS) shows an inverse behaviour. These results indicate that the reduction of ozone (Figure 7) at the tropical tropopause is enhanced by the chemical feedback, whereas the physical mixing is offset by the chemical feedback in the extra-tropical LS.

The chemical loss of ozone (Figure 8b) is enhanced below the tropical tropopause after including the CAT mixing parametrization. It is mainly contributed by HO_x (Figure 8e) and $O(^1D)$ (Figure 8g). Figure 8g shows the difference in the chemical loss by atomic oxygen. This shows the loss of ozone by removing $O(^1D)$ from the odd oxygen: ozone is photolysed to form $O(^1D)$ via Equation R1, $O(^1D)$ is then consumed with H_2O to form OH (R2). This also partly explains the increase of OH in Figure S2c in the supplement.

$$O_3 \xrightarrow{h\nu} O(^1D) + O_2 \tag{R1}$$

$$O(^1D) + H_2O \longrightarrow 2\,OH \tag{R2}$$

Figure 8e shows the changes in the chemical loss by HO_x. This illustrates the increasing loss of ozone at the tropical tropopause due to the OH/HO_x catalytic cycle. Ozone is destroyed by Equations R3 and R4 with OH/HO_x as a catalyst. This cycle is enhanced due to the increasing HO_x concentration (Figure S2f in the supplement).

$$OH + O_3 \longrightarrow HO_2 + 2\,O_2 \tag{R3}$$

$$HO_2 + O_3 \longrightarrow OH + O_2 \tag{R4}$$

$$\overline{\text{Net: } 2\,O_3 \longrightarrow 2\,O_2}$$

Mixing by CAT also reduces the chemical loss of ozone (Figure 8b) at the extra-tropical LS (∼100 to 50 hPa). Around half of the reduction is due to the reduction of HO_x (Figure S2f) and NO_x (Figure S2l and S2o) in the corresponding region. The reduction of HO_x in the extra-tropics LS and NO_x reduction in the UTLS decelerate the HO_x cycle and NO_x-related cycle. Halogens are responsible for the remaining reduction, especially in the Southern Hemisphere. The vertical mixing evened out the high concentrations at the poles, decelerating the catalytic cycle.

In addition, the change of the chemical regime of ozone is analyzed using the $HCHO/NO_2$ ratio (Formaldehyde to NO_2 ratio; FNR) and a novel diagnostic $\alpha_{CH_3O_2}$ developed by Nussbaumer et al. (2022). FNR is a commonly used indicator that develops from the principle that formation of tropospheric ozone requires volatile organic compounds (VOCs) and NO_x as its precursors (Acdan et al., 2023; Jin et al., 2020; Jiang et al., 2025). HCHO and NO_2 serve as the proxies of the VOCs and NO_x respectively, considering their similar chemical lifetime could better show competition between species (Tonnesen and Dennis, 2000). The lower FNR indicates VOC sensitivity, while the higher FNR indicates NO_x sensitivity. The $\alpha_{CH_3O_2}$ represents the fraction of CH_3O_2 forming HCHO via NO and OH relative to the competing pathway that forms CH_3OOH via HO_2 which could be used to

https://doi.org/10.5194/egusphere-2025-5382
Preprint. Discussion started: 12 November 2025

identify the HCHO production pathways. It could also be used to study ozone sensitivity (Nussbaumer et al., 2024). It is based on the concept that the formation of HCHO from CH_3O_2 with NO leads to O_3 production, while the formation of CH_3OOH from CH_3O_2 with HO_2 leads to termination of the HO_x cycle which decelerates the ozone production. The reaction of CH_3O_2 with OH that forms HCHO, which generally only plays a minor role, will not contribute to O_3 formation and therefore will be neglected when studying ozone sensitivity. It can therefore be calculated as shown in Equation. 5:

$$\alpha_{\mathrm{CH_3O_2}} = \frac{\mathrm{k_{CH_3O_2+NO}} \times [\mathrm{NO}]}{\mathrm{k_{CH_3O_2+NO}} \times [\mathrm{NO}] + \mathrm{k_{CH_3O_2+HO_2}} \times [\mathrm{HO_2}]} \tag{5}$$

Nussbaumer et al. (2023) shows that both the FNR and α_{CH3O2} are good indicators for the ozone chemical regime in the upper troposphere. Figure 9 shows the 10-year climatology of the α_{CH3O2}. CAT leads to slight changes in α_{CH3O2} in different altitudes. The difference of α_{CH3O2} (Figure 9a) shows a bi-modal distribution at the upper troposphere (∼200 hPa) and the lower troposphere (∼800 hPa). The Southern hemisphere exhibits a larger decrease with a maximum of 3%. The difference even reaches up to 6% during the JJA season in the southern polar region (not shown). The decreasing α_{CH3O2} indicates the decrease of NO and increase of HO_2, which is consistent with Figure S2l and S2f and the O_3 is relatively more sensitive to NO_x (less sensitive to VOCs) than without the CAT mixing. Figure 10 shows the 10-year climatology for the FNR. The Southern hemisphere depicts a more substantial absolute increase in FNR in the lower troposphere(∼800 hPa), while the upper troposphere (∼200 hPa) shows a percentage increase up to 26%. The changes above 200 hPa are neglected since the stratospheric ozone chemistry is significantly different than the troposphere. It shows consistent results with the α_{CH3O2}, the increasing FNR indicates the O_3 chemical regime is becoming relatively more NO_x sensitive (less VOCs sensitive). Both the FNR and α_{CH3O2} show that the CAT mixing in the UTLS also affects the tropospheric chemistry.

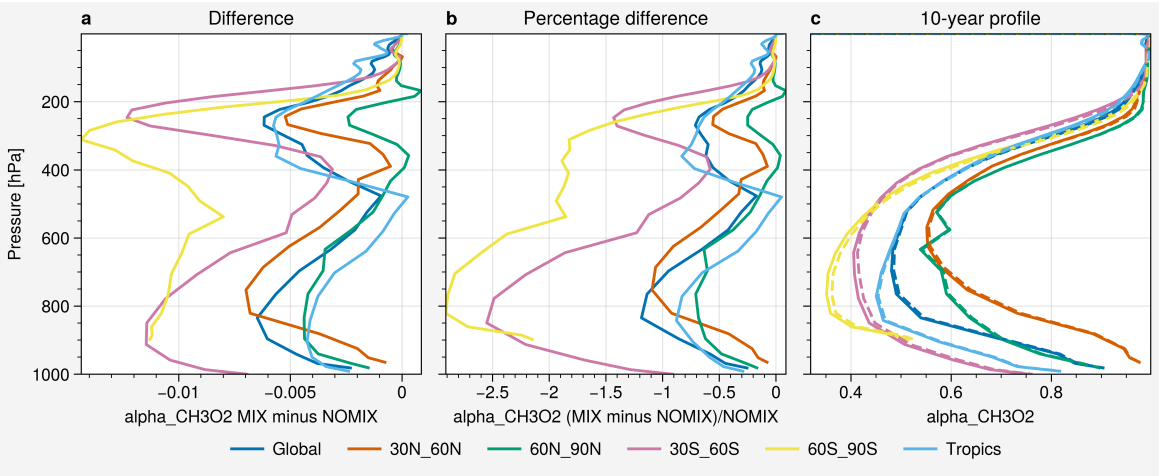

Figure 9. Vertical profile of the 10-year climatology of $\alpha_{\mathrm{CH_3O_2}}$ in different regions: (a) absolute difference (MIX - NOMIX), (b) percentage difference, (c) profiles. The solid lines indicates profiles of MIX, the dashed lines indicate profiles of NOMIX. The different colors denote respective latitude bands.

https://doi.org/10.5194/egusphere-2025-5382
Preprint. Discussion started: 12 November 2025

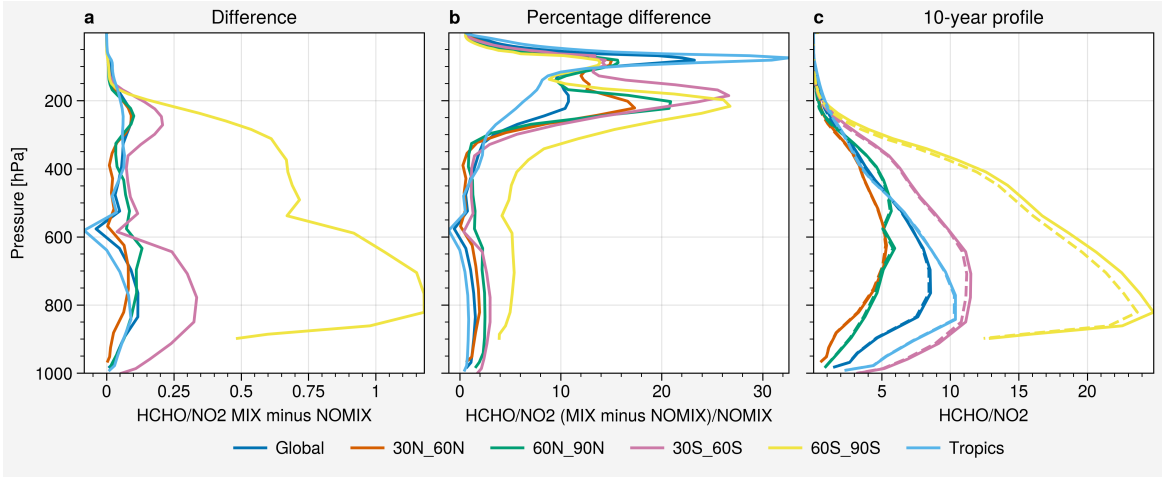

Figure 10. Vertical profile of the 10-year climatology of the $HCHO/NO_2$ ratio (FNR) in different regions: (a) absolute difference (MIX - NOMIX), (b) percentage difference, (c) profiles. The solid lines indicate profiles of MIX, the dashed lines indicate profiles of NOMIX. The different colors denote respective latitude bands.

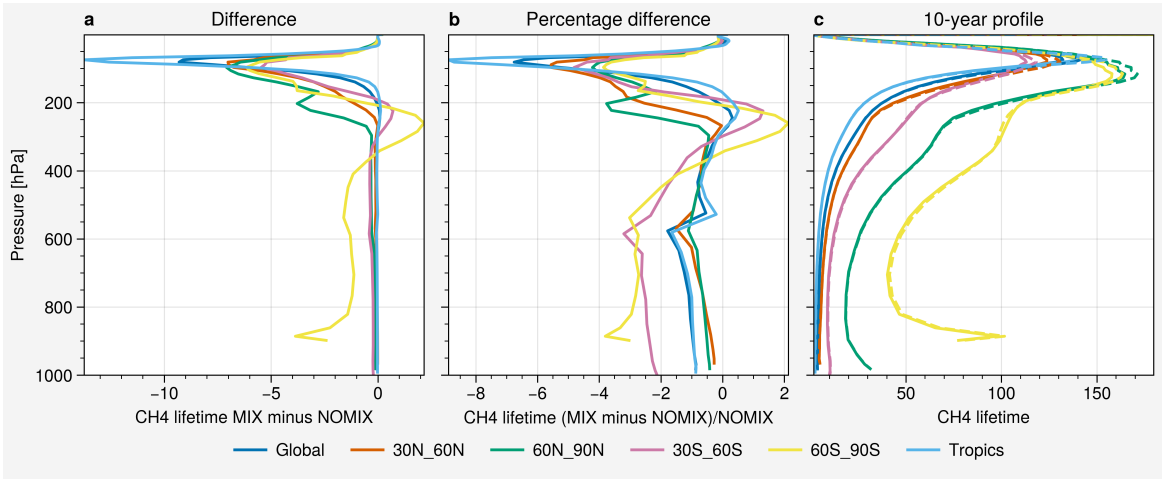

Figure 11. Vertical profile of the 10-year climatology of CH_4 lifetime (year) in different regions: (a) absolute difference (MIX - NOMIX), (b) percentage difference, (c) profiles. The solid lines indicate profiles of MIX, the dashed lines indicate profiles of NOMIX. The different colors denote respective latitude bands.

240 Furthermore, the chemical lifetime of CH_4 has been analyzed as well. Figure 11 shows the climatology of the methane lifetime. CAT mixing leads to a significant reduction of the CH_4 lifetime in the UTLS region, the tropics experienced a 15-year

https://doi.org/10.5194/egusphere-2025-5382
Preprint. Discussion started: 12 November 2025

(∼8%) decrease. The global atmospheric lifetime of CH_4 also shortened from 7.31 years to 7.24 years. It is mainly due to the change in OH distribution by CAT. Figure S2c shows that the OH increases mainly in the lower stratosphere with 10% of increase at the tropical tropopause which coincides with the lifetime profile in Figure 11. Considering the extremely short atmospheric lifetime of OH, the changes are unlikely to be a direct result of the CAT mixing on OH. It must be a result of either the changes in the OH precursors or sinks. One of the possible pathways is that the increasing OH by $O(^1D)$ leads to a more efficient CH_4 oxidation, which produces more HCHO and HO_2 (based on the lower $\alpha_{CH_3O_2}$). Photolysis of HCHO and HO_2 recycling then generates OH, establishing a HO_x–CH_4–HCHO feedback cycle.

To conclude, the CAT mixing clearly modifies the chemical regime of the O_3 budget, shifting the O_3 to become relatively sensitive to NO_x, as well as reducing the atmospheric lifetime of CH_4 by increasing OH.

3.2.3 Impact on radiation

The simulation results show that the CAT mixing of tracers leads to a radiative cooling on the global mean radiation fluxes at the top-of-the-atmosphere (TOA) of about 208.9 mW/m^2. It is mainly induced by the change in ozone (-210.5 mW/m^2). The other major greenhouse gases like CO_2, CH_4 and N_2O have a comparably small impact which either leads to a radiative cooling or heating effect at the TOA. The changes of the annual mean net radiation fluxes of different radiation calls are shown in Figure 12 and Figure 13. Each radiation call represents a different greenhouse gas scenario; a summary of the radiation calls is given in Table 1. Figure 12 illustrates the annual zonal mean difference of the net radiation fluxes. In general, CAT mixing leads to cooling above the tropopause and heating in the troposphere (Figure 12a). It is mainly contributed by ozone (Figure 12b), with almost identical behaviour as in Figure 12a. The loss of ozone in the UTLS shown in Figure 7a, leads to local and TOA radiative cooling as well as heating in the troposphere. CO_2 and CH_4 show mainly an opposite response compared to ozone, while CO_2 has a stronger radiative heating in the northern hemisphere, potentially because of anthropogenic activities. N_2O shows a heating effect in almost all altitudes, except for the tropical lower troposphere. Figure 13 shows the annual mean difference of the net radiation fluxes at the TOA and surface. CAT leads to radiative cooling at the TOA and heating at the surface, mainly contributed by ozone. It is more pronounced along the storm tracks, where strong jet stream and associated wind shear favour turbulent mixing in the UTLS. At the TOA, CO_2 leads to cooling in the Southern Hemisphere and heating in the Northern Hemisphere, while the surface shows an inverse behaviour. CH_4 warms the tropics at the TOA, but cools at the surface. Changes in N_2O result in heating at the TOA and the surface, except for the tropics.

Overall, CAT mixing leads to cooling in the Earth's radiation budget, mainly contributed by O_3, which is a greenhouse gas with spatial variability and also strongly active in the shortwave spectrum. In contrast, well-mixed greenhouse gases like CO_2, CH_4 and N_2O are rather insensitive to CAT mixing, with global mean TOA radiative effects of -0.2 mW/m^2, 0.13 mW/m^2 and 1.62 mW/m^2 respectively.

We examined the impact of CAT on tracers and their associated radiative effects. Overall, CAT leads to an increase in outgoing LW radiation at the TOA, corresponding to a cooling effect. It is mainly driven by ozone. The other major greenhouse gases, such as CO_2, CH_4, and N_2O which lead to changes in radiation of TOA are comparatively insensitive to CAT considering

https://doi.org/10.5194/egusphere-2025-5382
Preprint. Discussion started: 12 November 2025

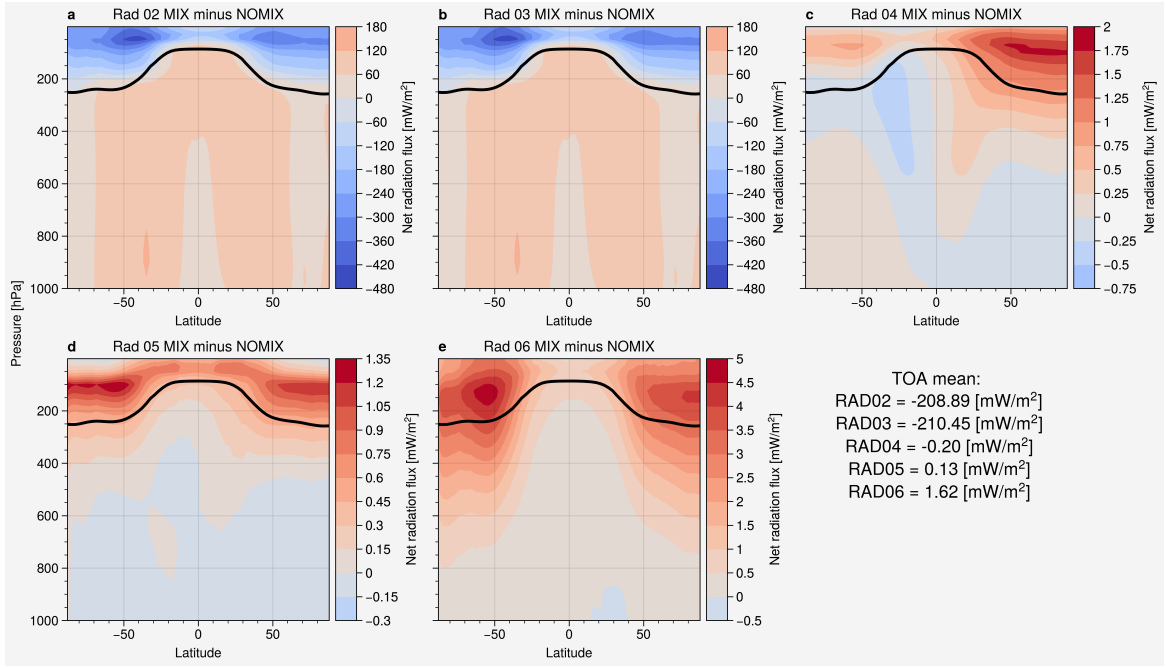

Figure 12. Annual zonal mean difference of net radiation fluxes for different radiation calls between two simulatioins: (a) RAD02, (b) RAD03 (O_3), (c) RAD04 (CO_2), (d) RAD05 (CH_4), and (e) RAD06 (N_2O). The numerical values given are differences of the global mean TOA radiation. The black line indicates the tropopause

https://doi.org/10.5194/egusphere-2025-5382
Preprint. Discussion started: 12 November 2025

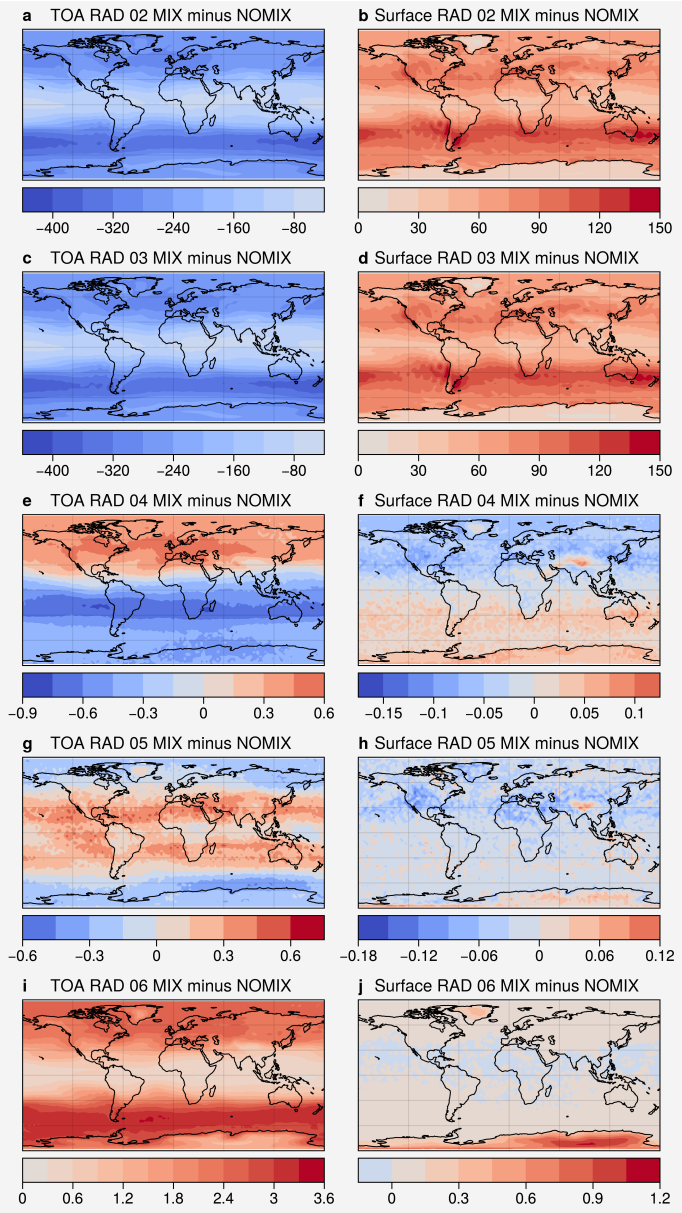

Figure 13. Annual mean difference of net radiation fluxes [mW/m^2] at the TOA for (a) RAD02, (c) RAD03, (e) RAD04, (g) RAD05, and (i) RAD06; and at the surface for (b) RAD02, (d) RAD03, (f) RAD04, (h) RAD05, and (j) RAD06.

https://doi.org/10.5194/egusphere-2025-5382
Preprint. Discussion started: 12 November 2025

4 Conclusion and Outlook

This study presents a new submodel for parametrizing vertical tracer mixing in the UTLS by Clear Air Turbulence (CAT), developed for the climate chemistry model EMAC, considering the dampening characteristics of the ECHAM5 turbulence scheme above the planetary boundary layer. The CAT mixing scheme is based on a two-layer mixing algorithm and the newly developed turbulence diagnostic MoCATI, which is a modification of the well-known Ellrod-Knox index by introducing static stability into the calculation. We conducted statistical tests and the relative frequency distribution of MoCATI and Ellrod-Knox index. The new index shows a comparable performance as the Ellrod-Knox index.

We performed two simulations (MIX and NOMIX) using the EMAC model in a QCTM configuration to examine the impact of CAT mixing parametrization on tracer distribution and its corresponding radiative impact. CAT leads to significant impacts on the non well-mixed gases like ozone in the UTLS. The changes are contributed by both the physical mixing and the chemical feedback from other tracers. ceO3 is significantly reduced in the UTLS and increases in the free troposphere as well as in the mid-stratosphere. The reduction in the tropics is a result of both the physical mixing and chemical feedback from other mixed tracers like odd oxygen and HO_x while the extra-tropics physical mixing is offset by the chemical feedback not only from odd oxygen and HO_x, but also from halogen species. Other major greenhouse gases including CO_2, CH_4 and N_2O are relatively insensitive to CAT considering their well-mixed characteristics and weak gradients particularly in the UTLS. It also shows that the CAT in the UTLS can change the chemical regime of O_3 not only in the UTLS region, but also in the lower troposphere, by shifting to a relatively more NO_x sensitive (less VOCs sensitive) environment. Methane lifetimes are also found to be shortened from 7.31 years to 7.24 years (especially at the stratosphere with a 15-year difference) because of the more effective HO_x catalytic cycle. CAT mixing also reduces the ozone bias at the polar mid-stratosphere by comparing the results with SWOOSH.

Simulations show that CAT could lead to surface radiative heating and radiative cooling at the TOA. The TOA is expected to be 0.2W/m^2 cooler. It is mostly contributed by ozone since water vapour is not taken into account in the QCTM mode. Other major greenhouse gases show negligible impacts on the radiation budget. Considering the strengthening trend of CAT under climate change, the cooling effect of CAT mixing on tracers could potentially partially offset the warmer climate.

Even though water vapour is not taken into account in the current version of CAT to obtain consistent dynamics in the QCTM mode, it is planned to also consider the potential radiative impact of water vapour by extending the CAT submodel and include the mixing of water vapour and temperature. The water vapour is expected to increase in the UTLS considering its gradient. The CAT submodel is also expected to be extended to include and combine more turbulence diagnostics in the future, considering the pros and cons of each diagnostic.

Code availability. The model code of the EMAC climate chemistry model can be obtained by becoming a member of the MESSy consortium as described on the corresponding webpage https://messy-interface.org/ .

https://doi.org/10.5194/egusphere-2025-5382
Preprint. Discussion started: 12 November 2025

Author contributions. CHC and HT conceptualized the study. HT and KK developed the CAT submodel with modifications from CHC. CHC and KK contributed to the submodel evaluation. CHC performed the simulations and analyzed the model results. CHC drafted the manuscript. CHC, HT, and PH discussed the results. All co-authors contributed to the review and final editing of the manuscript.

Competing interests. The contact author has declared that none of the authors has any competing interests

325

Acknowledgements. This work has been funded by the Deutsche Forschungsgemeinschaft (DFG, German Research Foundation) – TRR 301 – Project-ID 428312742 (project B01). The simulations were conducted using the supercomputer MOGON-NHR of Johannes Gutenberg University Mainz (https://hpc.uni-mainz.de/, last access: 15 September 2025).

https://doi.org/10.5194/egusphere-2025-5382
Preprint. Discussion started: 12 November 2025

References

330 Acdan, J. J. M., Pierce, R. B., Dickens, A. F., Adelman, Z., and Nergui, T.: Examining TROPOMI formaldehyde to nitrogen dioxide ratios in the Lake Michigan region: implications for ozone exceedances, Atmospheric Chemistry and Physics, 23, 7867–7885, https://doi.org/10.5194/acp-23-7867-2023, 2023.

Chau, C. H., Hoor, P., and Tost, H.: Simulated mixing in the UTLS by small-scale turbulence using multi-scale chemistry-climate model MECO(n), Atmospheric Chemistry and Physics, 25, 13 123–13 140, https://doi.org/10.5194/acp-25-13123-2025, 2025.

335 Davis, S. M., Rosenlof, K. H., Hassler, B., Hurst, D. F., Read, W. G., Vömel, H., Selkirk, H., Fujiwara, M., and Damadeo, R.: The Stratospheric Water and Ozone Satellite Homogenized (SWOOSH) database: a long-term database for climate studies, Earth System Science Data, 8, 461–490, https://doi.org/10.5194/essd-8-461-2016, 2016.

Deckert, R., Jöckel, P., Grewe, V., Gottschaldt, K.-D., and Hoor, P.: A quasi chemistry-transport model mode for EMAC, Geoscientific Model Development, 4, 195–206, https://doi.org/10.5194/gmd-4-195-2011, 2011.

340 Dee, D. P., Uppala, S. M., Simmons, A. J., Berrisford, P., Poli, P., Kobayashi, S., Andrae, U., Balmaseda, M. A., Balsamo, G., Bauer, P., Bechtold, P., Beljaars, A. C. M., van de Berg, L., Bidlot, J., Bormann, N., Delsol, C., Dragani, R., Fuentes, M., Geer, A. J., Haimberger, L., Healy, S. B., Hersbach, H., Hólm, E. V., Isaksen, L., Kållberg, P., Köhler, M., Matricardi, M., McNally, A. P., Monge-Sanz, B. M., Morcrette, J.-J., Park, B.-K., Peubey, C., de Rosnay, P., Tavolato, C., Thépaut, J.-N., and Vitart, F.: The ERA-Interim reanalysis: configuration and performance of the data assimilation system, Quarterly Journal of the Royal Meteorological Society, 137, 553–597,
345 https://doi.org/https://doi.org/10.1002/qj.828, 2011.

Dietmüller, S., Jöckel, P., Tost, H., Kunze, M., Gellhorn, C., Brinkop, S., Frömming, C., Ponater, M., Steil, B., Lauer, A., and Hendricks, J.: A new radiation infrastructure for the Modular Earth Submodel System (MESSy, based on version 2.51), Geoscientific Model Development, 9, 2209–2222, https://doi.org/10.5194/gmd-9-2209-2016, 2016.

Dutton, J. A. and Panofsky, H. A.: Clear Air Turbulence: A Mystery May Be Unfolding, Science, 167, 937–944,
350 https://doi.org/10.1126/science.167.3920.937, 1970.

Ellrod, G., Lester, P., and Ehernberger, L.: CLEAR AIR TURBULENCE, in: Encyclopedia of Atmospheric Sciences, edited by Holton, J. R., pp. 393–403, Academic Press, Oxford, ISBN 978-0-12-227090-1, https://doi.org/https://doi.org/10.1016/B0-12-227090-8/00104-4, 2003.

Ellrod, G. P. and Knapp, D. I.: An Objective Clear-Air Turbulence Forecasting Technique: Verification and Operational Use, Weather and Forecasting, 7, 150 – 165, https://doi.org/10.1175/1520-0434(1992)007<0150:AOCATF>2.0.CO;2, 1992.

355 Ellrod, G. P. and Knox, J. A.: Improvements to an Operational Clear-Air Turbulence Diagnostic Index by Addition of a Divergence Trend Term, Weather and Forecasting, 25, 789 – 798, https://doi.org/10.1175/2009WAF2222290.1, 2010.

Esler, J. G. and Polvani, L. M.: Kelvin–Helmholtz Instability of Potential Vorticity Layers: A Route to Mixing, Journal of the Atmospheric Sciences, 61, 1392 – 1405, https://doi.org/10.1175/1520-0469(2004)061<1392:KIOPVL>2.0.CO;2, 2004.

Eyring, V., Lamarque, J.-F., Hess, P., Arfeuille, F., Bowman, K., Chipperfiel, M. P., Duncan, B., Fiore, A., Gettelman, A., Giorgetta, M. A.,
360 et al.: Overview of IGAC/SPARC Chemistry-Climate Model Initiative (CCMI) community simulations in support of upcoming ozone and climate assessments, SPARC newsletter, 40, 48–66, 2013.

Fawcett, T.: An introduction to ROC analysis, Pattern Recognition Letters, 27, 861–874, https://doi.org/https://doi.org/10.1016/j.patrec.2005.10.010, rOC Analysis in Pattern Recognition, 2006.

https://doi.org/10.5194/egusphere-2025-5382
Preprint. Discussion started: 12 November 2025

Forster, P., Storelvmo, T., Armour, K., Collins, W., Dufresne, J.-L., Frame, D., Lunt, D., Mauritsen, T., Palmer, M., Watanabe, M., Wild, M., and Zhang, H.: Chapter 7: The Earth's energy budget, climate feedbacks, and climate sensitivity, https://doi.org/10.25455/wgtn.16869671.v1, 2021.

Forster, P. M. and Shine, K. P.: Radiative forcing and temperature trends from stratospheric ozone changes, Journal of Geophysical Research: Atmospheres, 102, 10 841–10 855, https://doi.org/https://doi.org/10.1029/96JD03510, 1997.

Forster, P. M. and Shine, K. P.: Stratospheric water vapour changes as a possible contributor to observed stratospheric cooling, Geophysical Research Letters, 26, 3309–3312, https://doi.org/https://doi.org/10.1029/1999GL010487, 1999.

Giorgetta, M. A., Manzini, E., Roeckner, E., Esch, M., and Bengtsson, L.: Climatology and Forcing of the Quasi-Biennial Oscillation in the MAECHAM5 Model, Journal of Climate, 19, 3882 – 3901, https://doi.org/10.1175/JCLI3830.1, 2006.

Holton, J. R., Haynes, P. H., McIntyre, M. E., Douglass, A. R., Rood, R. B., and Pfister, L.: Stratosphere-troposphere exchange, Reviews of Geophysics, 33, 403–439, https://doi.org/https://doi.org/10.1029/95RG02097, 1995.

Hu, B., Tang, J., Ding, J., and Liu, G.: Regional downscaled future change of clear-air turbulence over East Asia under RCP8.5 scenario within the CORDEX-EA-II project, International Journal of Climatology, 41, 5022–5035, https://doi.org/https://doi.org/10.1002/joc.7114, 2021.

Jiang, Z., Wang, S., Yan, Y., Zhang, S., Xue, R., Gu, C., Zhu, J., Liu, J., and Zhou, B.: Constructing the 3D Spatial Distribution of the HCHO/NO2 Ratio via Satellite Observation and Machine Learning Model, Environmental Science & Technology, 59, 4047–4058, https://doi.org/10.1021/acs.est.4c12362, pMID: 39977671, 2025.

Jin, X., Fiore, A., Boersma, K. F., Smedt, I. D., and Valin, L.: Inferring Changes in Summertime Surface Ozone–NOx–VOC Chemistry over U.S. Urban Areas from Two Decades of Satellite and Ground-Based Observations, Environmental Science & Technology, 54, 6518–6529, https://doi.org/10.1021/acs.est.9b07785, pMID: 32348127, 2020.

Jöckel, P., Sander, R., Kerkweg, A., Tost, H., and Lelieveld, J.: Technical Note: The Modular Earth Submodel System (MESSy) - a new approach towards Earth System Modeling, Atmospheric Chemistry and Physics, 5, 433–444, https://doi.org/10.5194/acp-5-433-2005, 2005.

Jöckel, P., Tost, H., Pozzer, A., Brühl, C., Buchholz, J., Ganzeveld, L., Hoor, P., Kerkweg, A., Lawrence, M. G., Sander, R., Steil, B., Stiller, G., Tanarhte, M., Taraborrelli, D., van Aardenne, J., and Lelieveld, J.: The atmospheric chemistry general circulation model ECHAM5/MESSy1: consistent simulation of ozone from the surface to the mesosphere, Atmospheric Chemistry and Physics, 6, 5067–5104, https://doi.org/10.5194/acp-6-5067-2006, 2006.

Jöckel, P., Kerkweg, A., Pozzer, A., Sander, R., Tost, H., Riede, H., Baumgaertner, A., Gromov, S., and Kern, B.: Development cycle 2 of the Modular Earth Submodel System (MESSy2), Geoscientific Model Development, 3, 717–752, https://doi.org/10.5194/gmd-3-717-2010, 2010.

Jöckel, P., Tost, H., Pozzer, A., Kunze, M., Kirner, O., Brenninkmeijer, C. A. M., Brinkop, S., Cai, D. S., Dyroff, C., Eckstein, J., Frank, F., Garny, H., Gottschaldt, K.-D., Graf, P., Grewe, V., Kerkweg, A., Kern, B., Matthes, S., Mertens, M., Meul, S., Neumaier, M., Nützel, M., Oberländer-Hayn, S., Ruhnke, R., Runde, T., Sander, R., Scharffe, D., and Zahn, A.: Earth System Chemistry integrated Modelling (ESCiMo) with the Modular Earth Submodel System (MESSy) version 2.51, Geoscientific Model Development, 9, 1153–1200, https://doi.org/10.5194/gmd-9-1153-2016, 2016.

Kaluza, T., Kunkel, D., and Hoor, P.: On the occurrence of strong vertical wind shear in the tropopause region: a 10-year ERA5 northern hemispheric study, Weather and Climate Dynamics, 2, 631–651, https://doi.org/10.5194/wcd-2-631-2021, 2021.

https://doi.org/10.5194/egusphere-2025-5382
Preprint. Discussion started: 12 November 2025

Kaluza, T., Kunkel, D., and Hoor, P.: Analysis of Turbulence Reports and ERA5 Turbulence Diagnostics in a Tropopause-Based Vertical Framework, Geophysical Research Letters, 49, e2022GL100 036, https://doi.org/https://doi.org/10.1029/2022GL100036, e2022GL100036 2022GL100036, 2022.

Konopka, P., Steinhorst, H.-M., Grooß, J.-U., Günther, G., Müller, R., Elkins, J. W., Jost, H.-J., Richard, E., Schmidt, U., Toon, G., and McKenna, D. S.: Mixing and ozone loss in the 1999–2000 Arctic vortex: Simulations with the three-dimensional Chemical Lagrangian Model of the Stratosphere (CLaMS), Journal of Geophysical Research: Atmospheres, 109, https://doi.org/https://doi.org/10.1029/2003JD003792, 2004.

Konopka, P., Tao, M., Ploeger, F., Diallo, M., and Riese, M.: Tropospheric mixing and parametrization of unresolved convective updrafts as implemented in the Chemical Lagrangian Model of the Stratosphere (CLaMS v2.0), Geoscientific Model Development, 12, 2441–2462, https://doi.org/10.5194/gmd-12-2441-2019, 2019.

Kunkel, D., Hoor, P., Kaluza, T., Ungermann, J., Kluschat, B., Giez, A., Lachnitt, H.-C., Kaufmann, M., and Riese, M.: Evidence of small-scale quasi-isentropic mixing in ridges of extratropical baroclinic waves, Atmospheric Chemistry and Physics, 19, 12 607–12 630, https://doi.org/10.5194/acp-19-12607-2019, 2019.

Lacis, A. A., Wuebbles, D. J., and Logan, J. A.: Radiative forcing of climate by changes in the vertical distribution of ozone, Journal of Geophysical Research: Atmospheres, 95, 9971–9981, https://doi.org/https://doi.org/10.1029/JD095iD07p09971, 1990.

Lee, S. H., Williams, P. D., and Frame, T. H.: Increased shear in the North Atlantic upper-level jet stream over the past four decades, Nature, 572, 639–642, 2019.

McKenna, D. S., Grooß, J.-U., Günther, G., Konopka, P., Müller, R., Carver, G., and Sasano, Y.: A new Chemical Lagrangian Model of the Stratosphere (CLaMS) 2. Formulation of chemistry scheme and initialization, Journal of Geophysical Research: Atmospheres, 107, ACH 4–1–ACH 4–14, https://doi.org/https://doi.org/10.1029/2000JD000113, 2002a.

McKenna, D. S., Konopka, P., Grooß, J.-U., Günther, G., Müller, R., Spang, R., Offermann, D., and Orsolini, Y.: A new Chemical Lagrangian Model of the Stratosphere (CLaMS) 1. Formulation of advection and mixing, Journal of Geophysical Research: Atmospheres, 107, ACH 15–1–ACH 15–15, https://doi.org/https://doi.org/10.1029/2000JD000114, 2002b.

Nussbaumer, C. M., Pozzer, A., Tadic, I., Röder, L., Obersteiner, F., Harder, H., Lelieveld, J., and Fischer, H.: Tropospheric ozone production and chemical regime analysis during the COVID-19 lockdown over Europe, Atmospheric Chemistry and Physics, 22, 6151–6165, https://doi.org/10.5194/acp-22-6151-2022, 2022.

Nussbaumer, C. M., Fischer, H., Lelieveld, J., and Pozzer, A.: What controls ozone sensitivity in the upper tropical troposphere?, Atmospheric Chemistry and Physics, 23, 12 651–12 669, https://doi.org/10.5194/acp-23-12651-2023, 2023.

Nussbaumer, C. M., Kohl, M., Pozzer, A., Tadic, I., Rohloff, R., Marno, D., Harder, H., Ziereis, H., Zahn, A., Obersteiner, F., Hofzumahaus, A., Fuchs, H., Künstler, C., Brune, W. H., Ryerson, T. B., Peischl, J., Thompson, C. R., Bourgeois, I., Lelieveld, J., and Fischer, H.: Ozone Formation Sensitivity to Precursors and Lightning in the Tropical Troposphere Based on Airborne Observations, Journal of Geophysical Research: Atmospheres, 129, e2024JD041 168, https://doi.org/https://doi.org/10.1029/2024JD041168, e2024JD041168 2024JD041168, 2024.

Paul, J., Fortuin, F., and Kelder, H.: An ozone climatology based on ozonesonde and satellite measurements, Journal of Geophysical Research: Atmospheres, 103, 31 709–31 734, https://doi.org/https://doi.org/10.1029/1998JD200008, 1998.

Plummer, D., Nagashima, T., Tilmes, S., Archibald, A., Chiodo, G., Fadnavis, S., Garny, H., Josse, B., Kim, J., Lamarque, J.-F., et al.: CCMI-2022: A new set of Chemistry-Climate Model Initiative (CCMI) community simulations to update the assessment of models and support upcoming Ozone Assessment activities, SPARC Newsletter, 57, 22–30, 2021.

https://doi.org/10.5194/egusphere-2025-5382
Preprint. Discussion started: 12 November 2025

Pommrich, R., Müller, R., Grooß, J.-U., Konopka, P., Ploeger, F., Vogel, B., Tao, M., Hoppe, C. M., Günther, G., Spelten, N., Hoffmann, L., Pumphrey, H.-C., Viciani, S., D'Amato, F., Volk, C. M., Hoor, P., Schlager, H., and Riese, M.: Tropical troposphere to stratosphere transport of carbon monoxide and long-lived trace species in the Chemical Lagrangian Model of the Stratosphere (CLaMS), Geoscientific Model Development, 7, 2895–2916, https://doi.org/10.5194/gmd-7-2895-2014, 2014.

Randel, W. J., Wu, F., and Forster, P.: The Extratropical Tropopause Inversion Layer: Global Observations with GPS Data, and a Radiative Forcing Mechanism, Journal of the Atmospheric Sciences, 64, 4489 – 4496, https://doi.org/10.1175/2007JAS2412.1, 2007.

Riese, M., Ploeger, F., Rap, A., Vogel, B., Konopka, P., Dameris, M., and Forster, P.: Impact of uncertainties in atmospheric mixing on simulated UTLS composition and related radiative effects, Journal of Geophysical Research: Atmospheres, 117, https://doi.org/https://doi.org/10.1029/2012JD017751, 2012.

Righi, M., Eyring, V., Gottschaldt, K.-D., Klinger, C., Frank, F., Jöckel, P., and Cionni, I.: Quantitative evaluation of ozone and selected climate parameters in a set of EMAC simulations, Geoscientific Model Development, 8, 733–768, https://doi.org/10.5194/gmd-8-733-2015, 2015.

Roeckner, E., Bäuml, G., Bonaventura, L., Brokopf, R., Esch, M., Giorgetta, M., Hagemann, S., Kirchner, I., Kornblueh, L., Manzini, E., et al.: The atmospheric general circulation model ECHAM 5. PART I: Model description, 2003.

Sander, R., Baumgaertner, A., Gromov, S., Harder, H., Jöckel, P., Kerkweg, A., Kubistin, D., Regelin, E., Riede, H., Sandu, A., Taraborrelli, D., Tost, H., and Xie, Z.-Q.: The atmospheric chemistry box model CAABA/MECCA-3.0, Geoscientific Model Development, 4, 373–380, https://doi.org/10.5194/gmd-4-373-2011, 2011.

Sharman, R., Tebaldi, C., Wiener, G., and Wolff, J.: An Integrated Approach to Mid- and Upper-Level Turbulence Forecasting, Weather and Forecasting, 21, 268 – 287, https://doi.org/10.1175/WAF924.1, 2006.

Smith, I. H., Williams, P. D., and Schiemann, R.: Clear-air turbulence trends over the North Atlantic in high-resolution climate models, Climate Dynamics, 61, 3063–3079, 2023.

Solomon, S., Rosenlof, K. H., Portmann, R. W., Daniel, J. S., Davis, S. M., Sanford, T. J., and Plattner, G.-K.: Contributions of Stratospheric Water Vapor to Decadal Changes in the Rate of Global Warming, Science, 327, 1219–1223, https://doi.org/10.1126/science.1182488, 2010.

Stevenson, D. S., Dentener, F. J., Schultz, M. G., Ellingsen, K., van Noije, T. P. C., Wild, O., Zeng, G., Amann, M., Atherton, C. S., Bell, N., Bergmann, D. J., Bey, I., Butler, T., Cofala, J., Collins, W. J., Derwent, R. G., Doherty, R. M., Drevet, J., Eskes, H. J., Fiore, A. M., Gauss, M., Hauglustaine, D. A., Horowitz, L. W., Isaksen, I. S. A., Krol, M. C., Lamarque, J.-F., Lawrence, M. G., Montanaro, V., Müller, J.-F., Pitari, G., Prather, M. J., Pyle, J. A., Rast, S., Rodriguez, J. M., Sanderson, M. G., Savage, N. H., Shindell, D. T., Strahan, S. E., Sudo, K., and Szopa, S.: Multimodel ensemble simulations of present-day and near-future tropospheric ozone, Journal of Geophysical Research: Atmospheres, 111, https://doi.org/https://doi.org/10.1029/2005JD006338, 2006.

Stohl, A., Bonasoni, P., Cristofanelli, P., Collins, W., Feichter, J., Frank, A., Forster, C., Gerasopoulos, E., Gäggeler, H., James, P., Kentarchos, T., Kromp-Kolb, H., Krüger, B., Land, C., Meloen, J., Papayannis, A., Priller, A., Seibert, P., Sprenger, M., Roelofs, G. J., Scheel, H. E., Schnabel, C., Siegmund, P., Tobler, L., Trickl, T., Wernli, H., Wirth, V., Zanis, P., and Zerefos, C.: Stratosphere-troposphere exchange: A review, and what we have learned from STACCATO, Journal of Geophysical Research: Atmospheres, 108, https://doi.org/https://doi.org/10.1029/2002JD002490, 2003.

Taylor, K., Williamson, D., and Zwiers, F.: AMIP II Sea Surface Temperature and Sea Ice Concentration Boundary Conditions, PCMDI Rep., 60, 2000.

https://doi.org/10.5194/egusphere-2025-5382
Preprint. Discussion started: 12 November 2025

Tonnesen, G. S. and Dennis, R. L.: Analysis of radical propagation efficiency to assess ozone sensitivity to hydrocarbons and NO x : 2. Long-lived species as indicators of ozone concentration sensitivity, Journal of Geophysical Research: Atmospheres, 105, 9227–9241, https://doi.org/https://doi.org/10.1029/1999JD900372, 2000.

Traub, M. and Lelieveld, J.: Cross-tropopause transport over the eastern Mediterranean, Journal of Geophysical Research: Atmospheres, 108, https://doi.org/https://doi.org/10.1029/2003JD003754, 2003.

Watkins, C. and Browning, K.: The detection of clear air turbulence by radar, Physics in Technology, 4, 28, https://doi.org/10.1088/0305-4624/4/1/I01, 1973.

Williams, P. D.: Increased light, moderate, and severe clear-air turbulence in response to climate change, Advances in atmospheric sciences, 34, 576–586, 2017.

Williams, P. D. and Joshi, M. M.: Intensification of winter transatlantic aviation turbulence in response to climate change, Nature Climate Change, 3, 644–648, 2013.

Williams, P. D. and Storer, L. N.: Can a climate model successfully diagnose clear-air turbulence and its response to climate change?, Quarterly Journal of the Royal Meteorological Society, 148, 1424–1438, https://doi.org/https://doi.org/10.1002/qj.4270, 2022.

```
&CTRL

! cat_param describes the approach how to calculate turbulence
!           1 = Ellrod + Knox (DVSI + DVT)
cat_param = 1

! nhours describes the length of the interval for which the divergence
                                      trend term should be calculated, e.g. 6 hours
nhours = 6.

! DIV_C is a weighting constant to limit the amplitude of the divergence trend term
DIV_C  = 0.1

! N2_lim is the limitation threshold for modifying the stability term, mixing will
                          be switched off at the grid box that N2 is  below N2_lim
N2_lim = 6.e-4

! t_norm1 & t_norm2 is the time normalization factor to moderate the strength
                                                              of the whole mixing term
t_norm_1 = 86400
t_norm_2 = 4.e6

! logical switch for performing tracer mixing by CAT
l_tracmix = .TRUE.

!use original Ellrod + Knox index for mixing, else use an index modified with N2
USE_DDVSI = .FALSE.
```

Figure S1. Example Fortran90 namelist for the new submodel CAT.

An example of the Fortran90 namelist of the CAT submodel is shown in Figure **??**. The namelist including 8 parameters:

- cat_param
- nhours
- DIV_C
- N2_lim
- t_norm1
- t_norm2
- l_tracmix
- USE_DDVSI

The cat_param determines the approach of how to calculate turbulence, currently the Ellrod-Knox index is the only option, but it provides the possibility to extend the submodel to other turbulence diagnostics. The nhours represents the length of the interval (h2 and h1 in equation 1) for which the divergence trend term should be calculated. DIV_C is the constant C in equation 1 and $N2\_lim$ is the N^2_{lim} in equation 2. t_norm_1 and t_norm_2 are used to calculate the t_norm in equation 4, where the former is the seconds of a day and later is the time scaling factor. $l\_tracmix$ is a logical switch for enabling the tracer mixing by CAT. It could be switched to false as a diagnostic submodel for calculating the turbulence diagnostics. The USE_DDVSI could switch between the Ellrod-Knox index and the MoCATI.

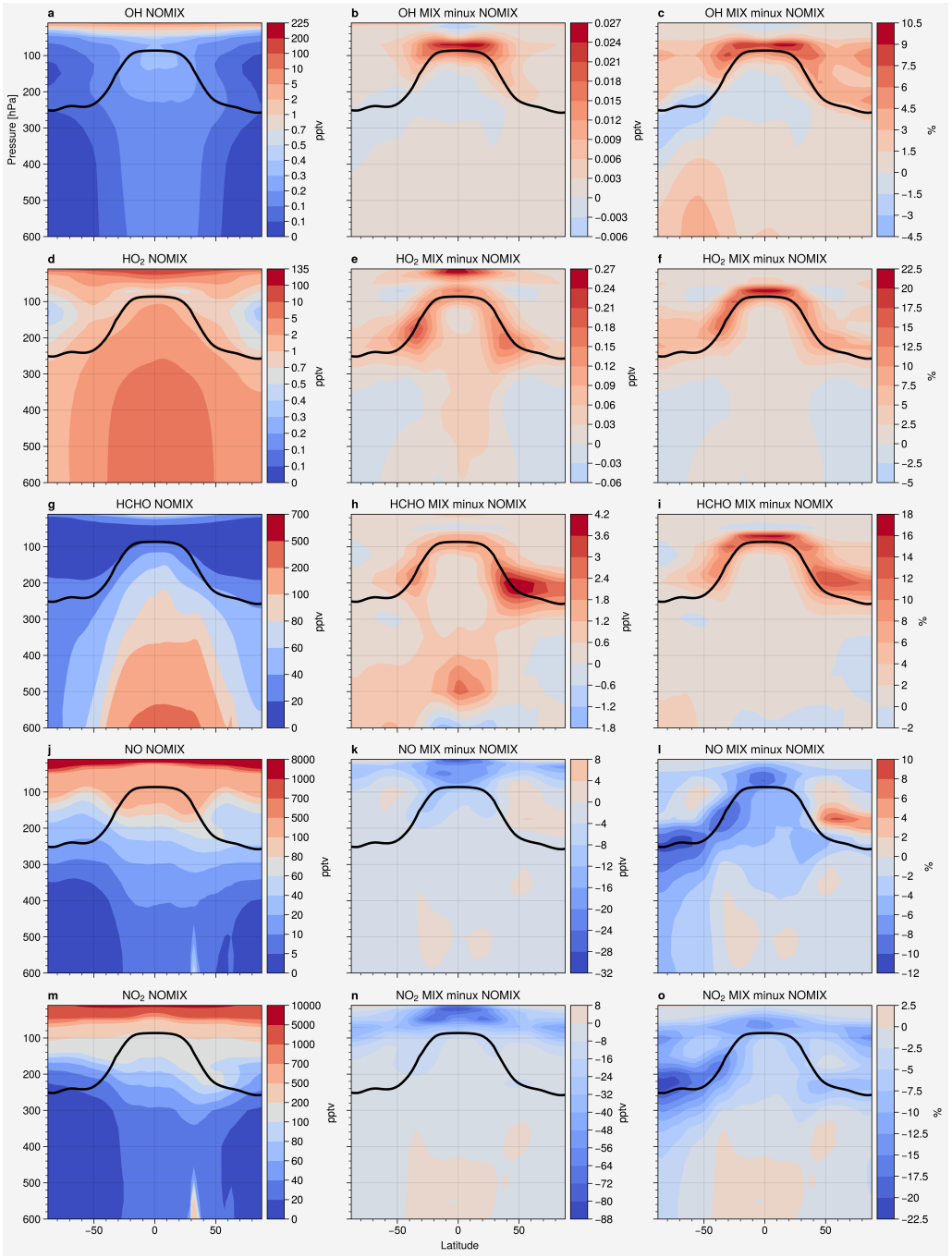

Figure S2. Annual zonal mean OH, HO2, HCHO,NO, NO2 (a,d,g,j,m) profile of QCTM-NOMIX, (b,e,h,k,n) difference, (c,f,i,l,o) percentage difference. The black line indicates the tropopause.

3.3 Potential impacts of mixing by Clear Air turbulence in water vapour

This chapter presents the potential impact of clear air turbulence on changing water vapour distribution in the UTLS and its radiative impact. In this chapter, the extension of the mixing scheme of CAT is presented. Its impact on the water vapour distribution and radiative impact is also discussed.

3.3.1 Extension of CAT submodel of EMAC

The CAT submodel has already been introduced in Chapter 3.2. In the previous version, the CAT mixing scheme was only applied to tracers. Since ECHAM5 does not handle water vapour as a tracer, it is not included by the CAT mixing scheme. However, considering the great potential on the radiative impact, water vapour should be considered. Water vapour, ice water content, liquid water content and temperature are now included in the CAT mixing scheme to represent the mixing of an air mass by CAT. Two extra logical switches l_water_mix and l_temp_mix are added to the namelist as namelist parameters to enable mixing on water and temperature respectively. By setting l_water_mix to $.TRUE.$, the CAT mixing will perform on water vapour, ice water content and liquid water content. The mixing of temperature is controlled by l_temp_mix. An example namelist with the new parameters is shown in Figure 3.1.

```
&CTRL

! cat_param describes the approach how to calculate turbulence
!           1 = Ellrod + Knox (DVSI + DVT)
cat_param = 1

! nhours describes the length of the interval for which the
  divergence trend term should be calculated, e.g. 6 hours
nhours = 6.

! DIV_C is a weighting constant to limit the amplitude of the
                                          divergence trend term
DIV_C  = 0.1

! N2_lim is the limitation threshold for modifying the stability
  term, mixing will be switched off at the grid box that
                                      N2 is below N2_lim
N2_lim = 6.e-4

! t_norm1 & t_norm2 is the time normalization factor to moderate
  the strength of the whole mixing term
t_norm_1 = 86400
t_norm_2 = 4.e6

! logical switch for performing tracer mixing by CAT
l_tracmix = .FALSE.

! logical switch for performing mixing by CAT on the water cycle
l_water_mix = .TRUE.

! logical switch for performing mixing by CAT on temperature
l_temp_mix  = .FALSE.

!use original Ellrod + Knox index for mixing, else use an index
 modified with N2
USE_DDVSI = .FALSE.
```

Figure 3.1: Example Fortran90 namelist for the CAT submodel with extension to water and temperature.

3.3.2 Experimental design

Two decadal simulations, DYN-MIX and DYN-NOMIX, are conducted using EMAC to investigate the impact of mixing by clear air turbulence on water vapour. Both simulations are run with pure dynamics, without enabling any chemistry-related submodels; the remaining model setups are identical with Chapter 3.2. Since the water vapour is the key component in changing the model dynamics, to investigate the sole impact of CAT mixing on water vapour, the feedback from the changing dynamics is suppressed by nudging the model dynamics towards the ERA5 reanalysis (Hersbach et al., 2020) up to 1 hPa in the atmosphere. The simulations are initialized by the ERAI reanalysis data (Dee et al., 2011). DYN-NOMIX with the CAT submodel disabled is used as a reference simulation, and DYN-MIX enables the CAT submodel to examine the impact of the CAT mixing on water vapour.

3.3.3 Results

Comparison on the model dynamics

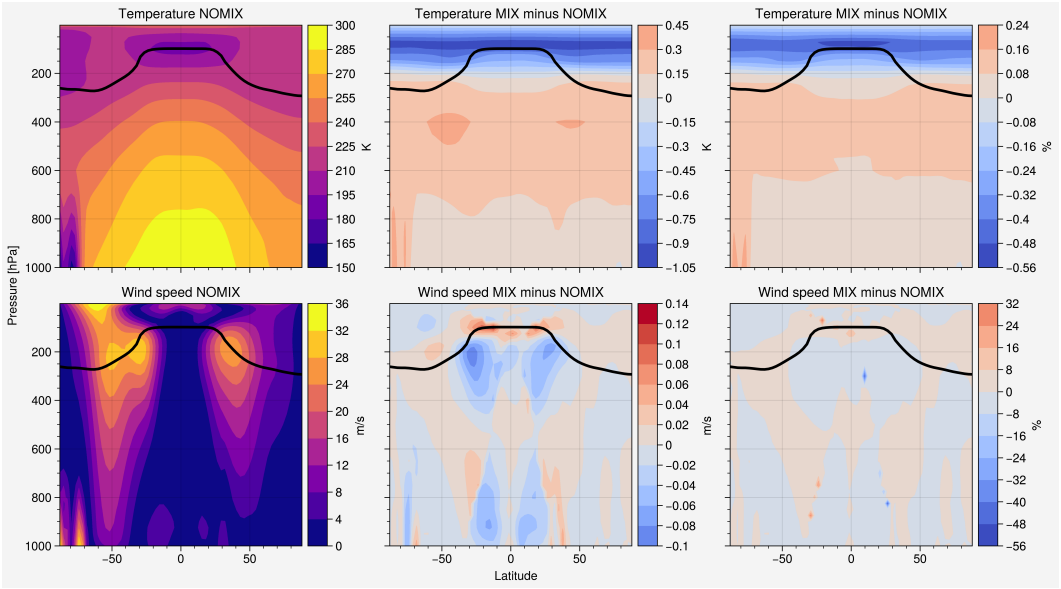

Figure 3.2: Annual zonal mean temperature (top) and wind speed (bottom) profile of DYN-NOMIX (left), difference (middle) and percentage difference (right). The black line indicates the tropopause.

Since the modification of water vapour changes the model dynamics, assessing changes in water vapour cannot be conducted under the QCTM mode. But in order to suppress the potential feedback, the model dynamics are nudged. This section examines the model dynamics in both simulations to ensure similar climate states serve as the common basis for comparison. Figure 3.2 shows the annual zonal mean temperature and horizontal wind speed profile of DYN-NOMIX and the difference between DYN-MIX and DYN-NOMIX. For temperature, the troposphere (below ∼200 hPa) is slightly warmer with a maximum of 0.5 K (0.24%). The stratosphere (above ∼200 hPa) is slightly cooler with a maximum of 1 K (-0.56%). For horizontal wind speed, it shows a high consistency between the two simulations. There are slight differences of around 0.1 m/s in the region of the subtropical jet. In terms of percentage change, it mostly lies within ±8%, only with extreme values near the vicinity of the jet, which is mostly due to a slight shift of the wind pattern or interpolation error.

Modifiying water vapour

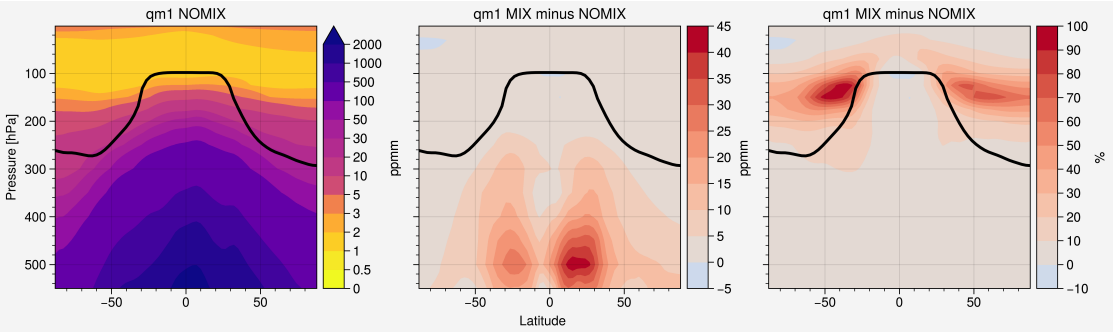

Figure 3.3: Annual zonal mean water vapour profile of DYN-NOMIX (left), difference (middle) and percentage difference (right). The black line indicates the tropopause.

Figure 3.3 shows the annual zonal mean mixing ratio and difference of the water vapour between DYN-MIX and DYN-NOMIX to assess the response of water vapour to the CAT mixing scheme. In terms of absolute changes, the CAT mixing induced changes maximize in the tropics at around 500 hPa, especially in the Northern Hemisphere, with more than 40 ppm. But considering the abundance

of water vapour in the troposphere, it turns out that only a few percent change compared to the background mixing ratio. In terms of relative changes, the water vapour is doubled at around 150 hPa between the tropical upper troposphere and the extratropical lower stratosphere. It is due to the dry environment in the stratosphere, only a few ppm change resulted in a substantial percentage increase.

Radiative impact

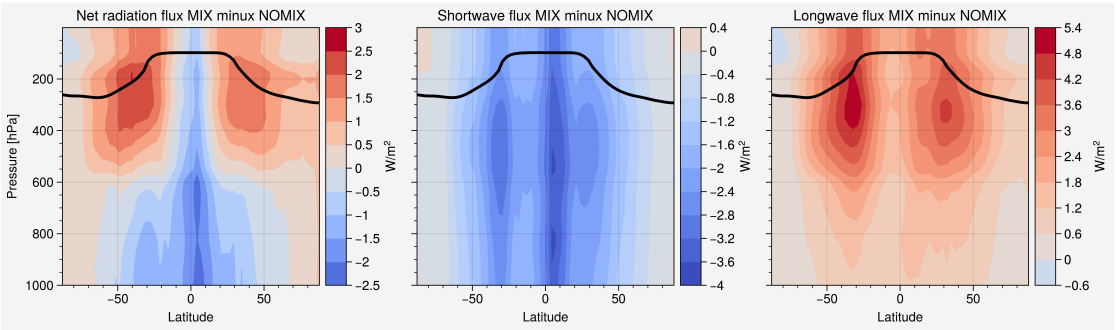

Figure 3.4: Annual zonal mean difference of net radiation (left), shortwave (middle) and longwave (right) flux. The black line indicates the tropopause.

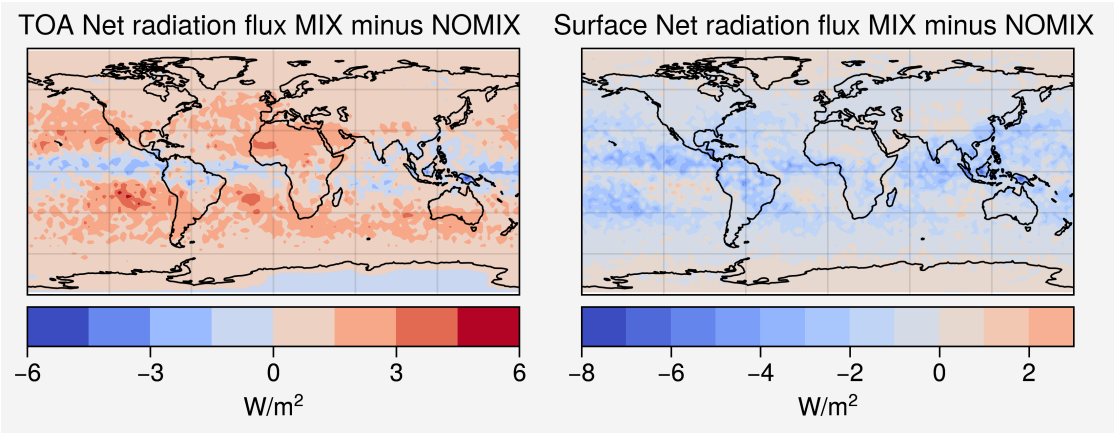

Figure 3.5: Annual mean difference of net radiation fluxes at the TOA (left) and surface (right).

Results show that the modification of water vapour by the CAT mixing scheme leads to a radiative heating at the top of the atmosphere (TOA) for 0.79 W/m^2. Figure 3.4 shows the cross section of net radiation, shortwave and longwave flux

differences between DYN-MIX and DYN-NOMIX. CAT mixing of water vapour leads to heating at the extratropics especially in the UTLS, and cooling at the tropics especially in the troposphere. The heating is due to the changes in the longwave flux, while the shortwave flux is responsible for the cooling. Figure 3.5 shows the difference of the net radiation flux at TOA and the surface respectively. CAT leads to radiative heating at TOA except for the tropics and Antarctica. It also leads to cooling at the surface except for the polar regions. The changes in the radiation budget between both simulations are a result of the changing water vapour distribution and its potential modifications to other components in the system. Although both simulations are nudged towards a similar meteorological state, water vapour is not nudged and could potentially affect cloud formation, which in turn affects cloud cover, reflection and scattering by the cloud, among other factors.

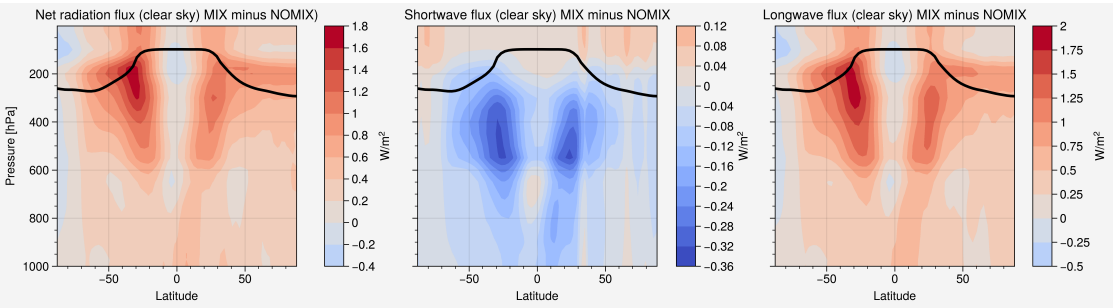

Figure 3.6: Annual zonal mean difference of net radiation (left), shortwave (middle) and longwave (right) flux under clear sky conditions. The black line indicates the tropopause.

Considering the potential difference between the cloud formation in both simulations, the radiation flux under clear sky conditions is shown in Figure 3.6. Under clear sky conditions, the net radiation flux has a significant difference, with almost only heating in the atmosphere. It is mainly contributed by the longwave radiation, since the shortwave is substantially weaker under clear sky conditions, with only one-tenth compared to the all sky conditions. Although the longwave radiation is also significantly weaker under clear sky conditions, with less than half compared to the all sky conditions, it still leads to a warmer atmosphere. The radiation fluxes under clear sky conditions are mostly a consequence of the

changing water vapour in the UTLS shown in Figure 3.3 (right) considering the nudged meteorology should not lead to a significant difference in the model dynamics. The cooling effect in the tropics and troposphere is mostly a result of the

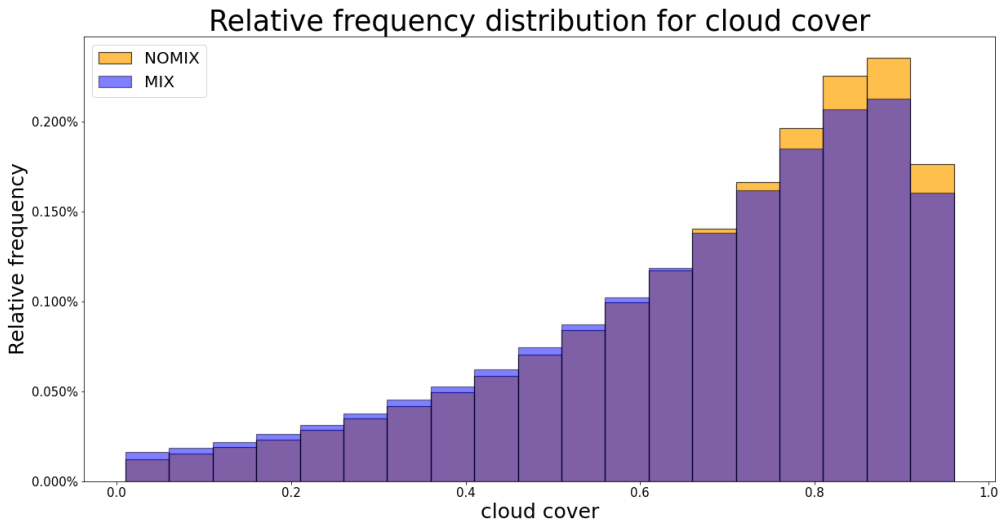

Figure 3.7: Relative frequency distribution of the cloud cover of DYN-MIX (purple) and DYN-NOMIX (orange).

changing clouds, the cloud cover is further analyzed. Figure 3.7 shows the relative frequency of the fraction of cloud cover. With mixing, the frequency of the high fraction of cloud cover is less than without mixing; the change of cloud cover leads to changes in the cloud optical depth. This requires further studies. However it is beyond the scope of the thesis.

Comparison on the nudging strength

Since both simulations with different water vapour distributions are nudged towards the same meteorological conditions, the difference in the nudging strength could imply the differences in the model dynamics. Figure 3.8 shows the instantaneous nudging temperature (NITEMP). The general nudging pattern shows no significant difference, especially in the stratosphere and in the troposphere. The main difference in the nudging strength is mainly in the UTLS, with stronger nudging at the extratropical LS and weaker in the tropical UT. The difference of the NITEMP and temperature (figure 3.2) above 200 hPa is because of the

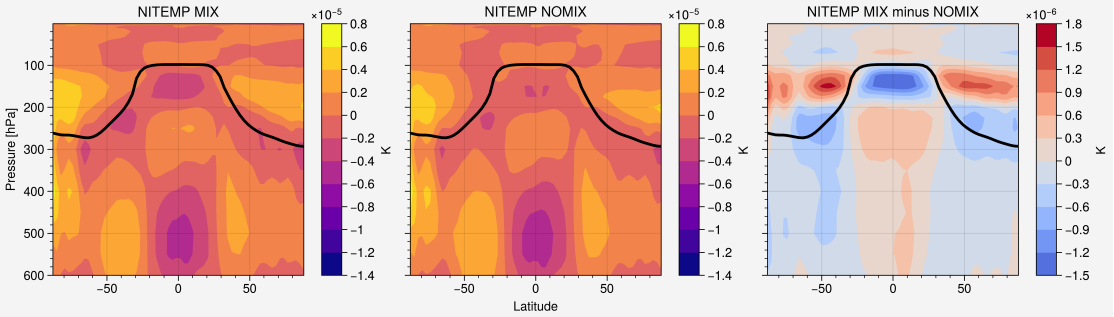

Figure 3.8: Annual zonal mean profile of the instantaneous nugding temperature of DYN-MIX (left), DYN-NOMIX (middle) and the difference (right). The black line indicates the tropopause.

calculation routine of the temperature. The nudging routine is called after the temperature calculation of ECHAM5, the modification of water vapour by CAT is calculated afterwards, as well as the further modification on the radiation, hence temperature. The temperature difference therefore always remains because of the remaining difference in water vapour. To avoid the temperature difference, one possible method would be using a larger nudging coefficient to nudge the model dynamics strongly towards the reanalysis data, but it will require further testing and will not be discussed in this thesis.

Conclusion

This chapter presents the extension of the CAT mixing scheme to water and temperature. Water vapour, ice water content, liquid water content and temperature are now included in the CAT mixing scheme. Two nudged decadal simulations are conducted to investigate the role of CAT mixing on water vapour. Results show that the water vapour near the subtropical jet is significantly increased. The redistribution of water vapour leads to a significant radiative impact of 0.79 W/m^2 on the Earth's radiation budget. This heating is a combination of the changing absorption by water vapour as well as the changed cloud cover.

3.4 Jet shifting with in MECO(n)

This chapter presents the preliminary results of the findings of the preparation work for simulating the TPEx I campaign in 2024. The MECO(n) model is used to simulate the atmospheric conditions under high horizontal and vertical resolution with multiple nests. A jet shift is discovered in the model, causing the model TPEx flight track to be next to the mislocated target jet stream, hence difficulties in direct comparison between measurements and modelling results. This chapter discusses the representation of MECO(n) on a synoptic scale and examines the possible solution to better represent the atmosphere.

3.4.1 TPEx I campaign 2024

The TPEx (TropoPause composition gradients and mixing Experiment) I campaign (Bozem et al., 2025) is the aircraft campaign of the transregional collaborative research centre TPChange (The Tropopause Region in a Changing Atmosphere). The flight campaign took place from 10 to 21 June 2024, based at the Hohn airfield in Northern Germany. The research aircraft Learjet 35A is used for the campaign. It is equipped with instrumentation to measure trace gases, aerosols, and etc. The TPEx I campaign also used a special approach by attaching a fully automated towed sensor shuttle (TPC-TOSS) with the aircraft and deploying it during the operation. This approach provides measurements like potential temperature and ozone mixing ratios as a vertical gradient between the aircraft and the TPC-TOSS. This approach is aimed to examine the small-scale variabilities by small-scale processes (e.g. turbulence) considering the short distance of 200 m between both platforms. There are a total of 8 scientific flights, 4 of them are operated with the TPC-TOSS over the Baltic Sea or North Sea. Flight 10 (further denoted as F10) conducted on 20 June 2024 on the North Sea is the targeted flight of the simulation preparation based on the preliminary results suggested the occurrence of turbulent mixing.

3.4.2 Model setup

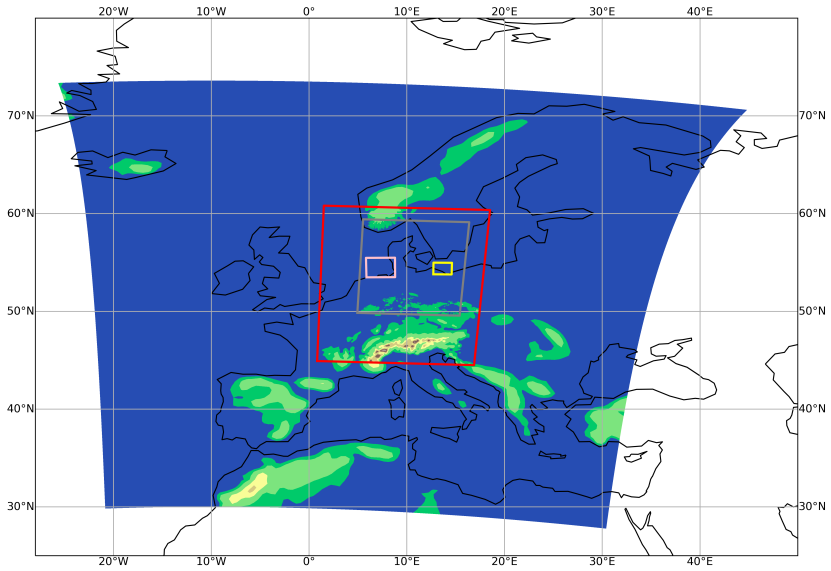

Figure 3.9: Model domain of CM40 with surface height. Red, grey, pink and yellow indicate the domain of CM10, CM2, CM1-N and CM1-B of the TPEx campaign.

The multi-scale climate chemistry model MECO(n) is used. The simulation contains 3 smaller COSMO/MESSy nests besides the global model EMAC (Figure 3.9). EMAC performed under T42L90MA (further denoted as EMAC-T42) is nested with a COSMO/MESSy (CM) instance covering most of Europe (further denoted as CM40-T42). CM40-T42 was further nested with another CM instance covering Germany (further denoted as CM10). CM10 is again coupled with another CM covering Northern Germany (further denoted as CM2).

The MECO(n) set up for EMAC-T42, CM40-T42 and CM10 is identical to the simulation in Chapter 3.1, except for the changed domain and the data used for initializing the simulation. Instead of using ERAI (Dee et al., 2011), ERA5 reanalysis (Hersbach et al., 2020) is used. For CM2, the parametrization of deep convection is switched off; only shallow convection is parametrized. The CM2 has a horizontal resolution of 0.02° with the enhanced vertical resolution EH-84 and a model time step of 6 s. CM2 is prepared to be further coupled with another 2 CM covering the North Sea (CM1-N) and the Baltic Sea (CM1-B), where the toss

mission took place, but is not used in this chapter.

3.4.3 Comparison with ERA5 data

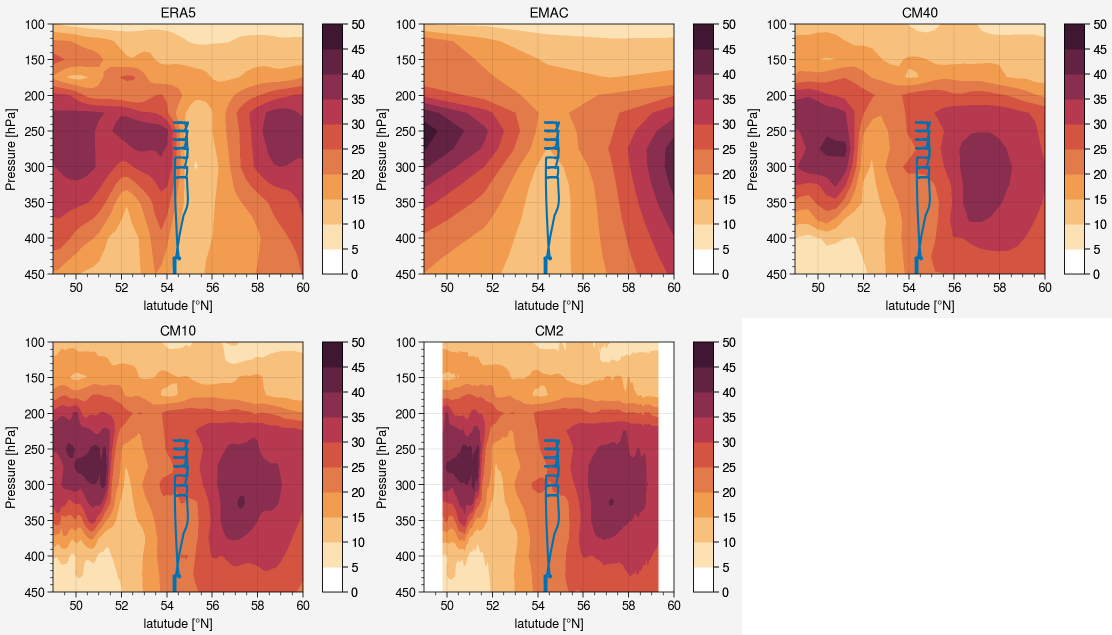

Figure 3.10: Cross section of the horizontal wind speed of ERA5, EMAC-T42, CM40-T42, CM10 and CM2 at 20 June 2024 0600 UTC. The blue lines indicate the flight track of the TPEx F10.

Figure 3.10 shows the cross-section of the horizontal wind during the start of F10 of ERA5, EMAC-T42, CM40-T42, CM10 and CM2. For ERA5, the F10 flight track is located in the southern branch of the jet system. The ERA5 reanalysis is used as the initial condition as well as the nudging data during the simulation. However, in EMAC-T42, the jet system shifted southward, resulting in the flight track located between two branches of the jet, and leaning more towards the northern branch. The jet mislocation further intensified for CM40-T42, CM10 and CM2, where the flight track was completely located within the northern branch of the jet system. The differences between the CM are minor. The discrepancy between ERA5 and EMAC-T42 could be attributed to the differences in the horizontal resolution. The ERA5 reanalysis is with 0.25° horizontal resolution while the EMAC-T42 is 2.8°.

The coarse horizontal resolution of EMAC-T42 resulted in a shift of 1 grid box horizontally after the interpolation from a normal lat/lon spacing to the spectral spacing used by ECHAM5. In order to obtain a broader picture of the jet system, the horizontal wind and relative humidity of ERA5, EMAC-T42 and CM40-T42 at 250 hPa are further compared (Figure 3.11).

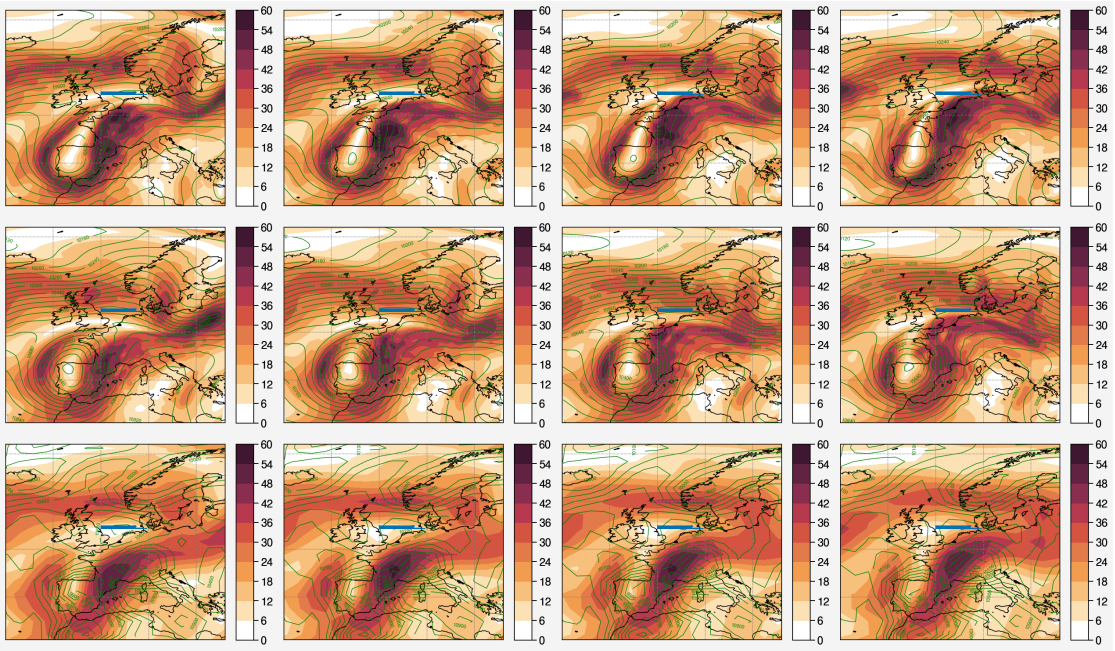

Figure 3.11: Map of the horizontal wind speed of ERA5 (top), CM40-T42 (middle) and EMAC-T42 (bottom) at 250 hPa at 20 June 2024 0000 (left), 0300 (middle left), 0600 (middle right), 0900 (right) UTC. The green contour represents the geopotential height. The blue lines indicate the flight track of the TPEx F10.

In general, MECO(n) reproduced features of the synoptic situation reasonably by comparing the ERA5 with CM. EMAC-T42 (Figure 3.11 bottom) under the T42 horizontal resolution is already known to be insufficient for reproducing a specific weather event due to its coarse resolution; the following discussion focuses on CM40-T42 (Figure 3.11 middle) with ERA5 (Figure 3.11 top). The ERA5 low pressure system is more elongated compared to the CM40-T42, which is relatively circular. Throughout the evolution of the low pressure system, e.g 0600 UTC (Figure 3.11 middle right), the ridge axis is bent more westward by the circular

low-pressure system of CM. This resulted in the trough of ERA5 in the Baltic countries at 0300 UTC, which propagated out of the domain already at 0600 UTC, is still remaining in the Baltic countries at 0600 UTC for CM. The ERA5 low pressure system is also propagating more towards the east, while CM remains at a similar location. The wind field of the ERA5 is also more continuous with slightly higher wind speed.

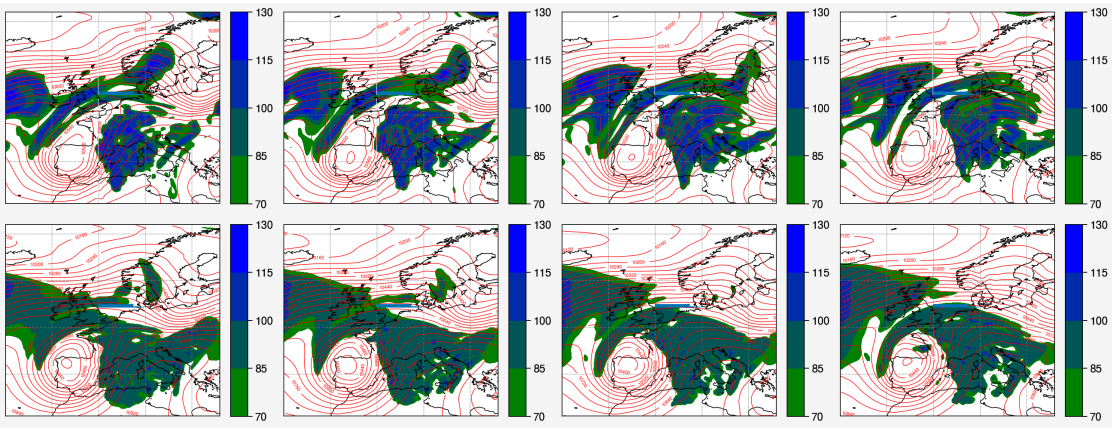

Figure 3.12: Map of the relative humidity (%) of ERA5 (top) and CM40 (bottom) at 250 hPa at 20 June 2024 0000 (left), 0300 (middle left), 0600 (middle right), 0900 (right) UTC. The red contour represents the geopotential height. The blue lines indicate the flight track of the TPEx F10.

Figure 3.12 shows the water content of ERA5 and CM, ERA5 is comparatively moister, the water vapour is supersaturated with RH $>$ 100%. For CM, since the COSMO cloud scheme will adjust supersaturation to a saturated state (Doms et al., 2011), it is relatively drier. However, since the low pressure system in ERA5 is more elongated, it shows a dry patch at the tail of the centre, which does not appear on COSMO. Overall, MECO(n) is able to reproduce the synoptic condition. However, the slight differences caused by the model resolution and differences in the parametrization scheme lead to deviation in the system, which makes direct comparison with observations difficult.

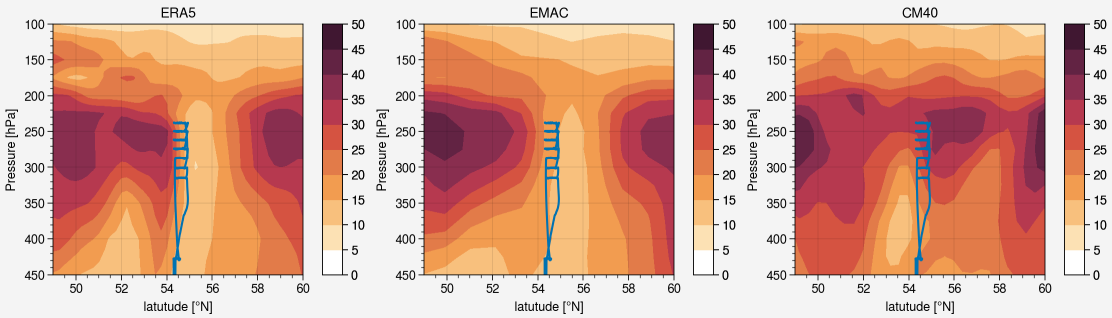

Figure 3.13: Cross section of the horizontal wind speed of ERA5, EMAC-T106 and CM40-T106 at 20 June 2024 0600 UTC. The blue lines indicate the flight track of the TPEx F10.

Therefore, an MECO(n) simulation with a higher horizontal resolution of T106 (1.125°) on EMAC is conducted (further denoted as EMAC-T106 and CM40-T106). Figure 3.13 shows the comparison between ERA5, EMAC-T106 and CM40-T106. By increasing the horizontal resolution of EMAC from T42 to T106, the horizontal wind shows a better consistency with the ERA5, where the flight track is now located nearer to the southern branch of the jet. For CM40-T106, it can reproduce a similar 3-maxima structure as the ERA5, however, its location is again mislocated.

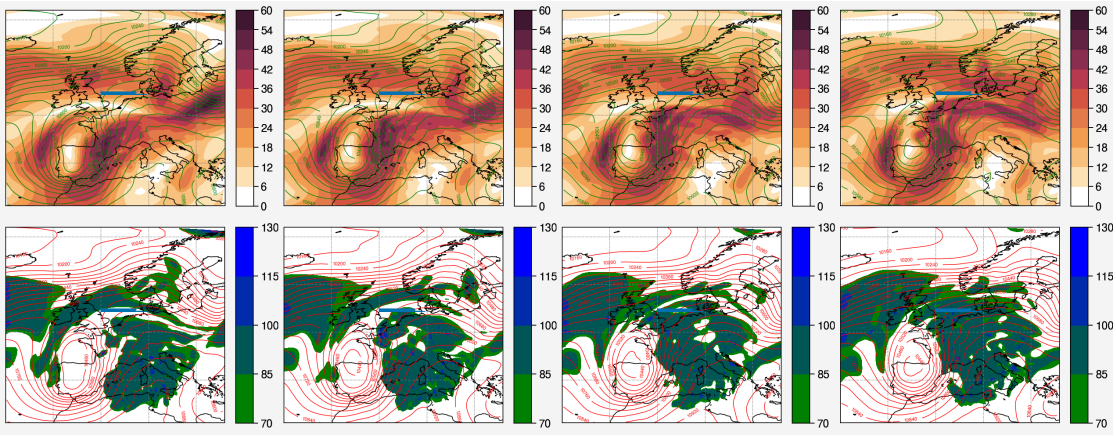

Figure 3.14: Map of the horizontal wind (top) and relative humidity (bottom) of ERA5 (top) and CM40 (bottom) at 250 hPa at 20 June 2024 0000 (left), 0300 (middle left), 0600 (middle right), 0900 (right) UTC. The red contour represents the geopotential height. The blue lines indicate the flight track of the TPEx F10.

Figure 3.14 shows the map of the horizontal wind and relative humidity of the CM40-T106. The CM40-T106 low pressure system is more consistent with the ERA5, with an elongated pressure centre without tilting. CM40-T106 is still overall drier than ERA5 because of the cloud scheme, but the dry patch of the low pressure centre is reconstructed as ERA5. The ridge trough structure also shows a better consistency between ERA5 and CM40-T106 than CM40-T42.

3.4.4 Comparison with measurement from TPEx

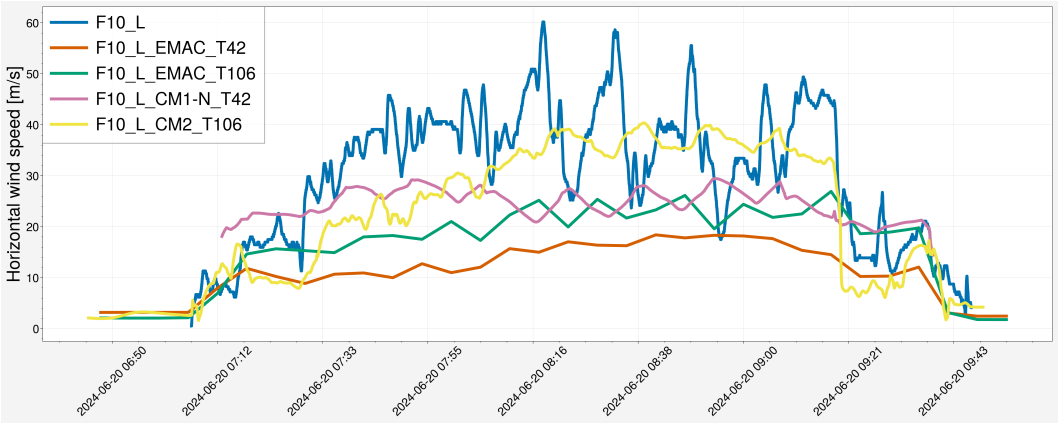

Figure 3.15: Time series of the TPEx F10 horizontal wind speed from the Learjet (blue), EMAC-T42 (orange), EMAC-T106 (green), CM1-N-T42 (pink) and CM2-T106 (yellow). Considering the computational cost, CM1-N under T106 resolution is not conducted. The highest resolution CM is taken from both simulations (CM1-N-T42 and CM2-T106) for comparison.

Figure 3.15 shows the comparison of the horizontal wind between the Learjet measurement and simulations. During F10, the Learjet traversed the jet stream boundary multiple times in order to measure the potential turbulence and experience high wind speeds. Along the flight track, EMAC-T42 (orange) is experiencing significantly lower wind speed compared to the measurement (blue), due to the mislocation of the jet. The nested CM of T42 (CM1-N-T42, pink) shows a higher wind speed. However, it shows an anti correlation with the measurement in terms of the fluctuation, indicating the flight track of the simulation traversed the jet in a

different time compared to the measurement. EMAC-T106 significantly improves with higher wind speed. It is also able to capture the signal of traversing the jet by reconstructing a similar fluctuation in the wind speed. However, the nested CM of T106 (CM2-T106, yellow) does not perform as well as the EMAC-T106 due to the discrepancy between the EMAC-T106 and its CM. It performs relatively reasonable in the first half of the flight. However, starting from 8:15, the model flight track shows again an anti correlation as CM1-N-T42, the traverse through the jet is again mistimed.

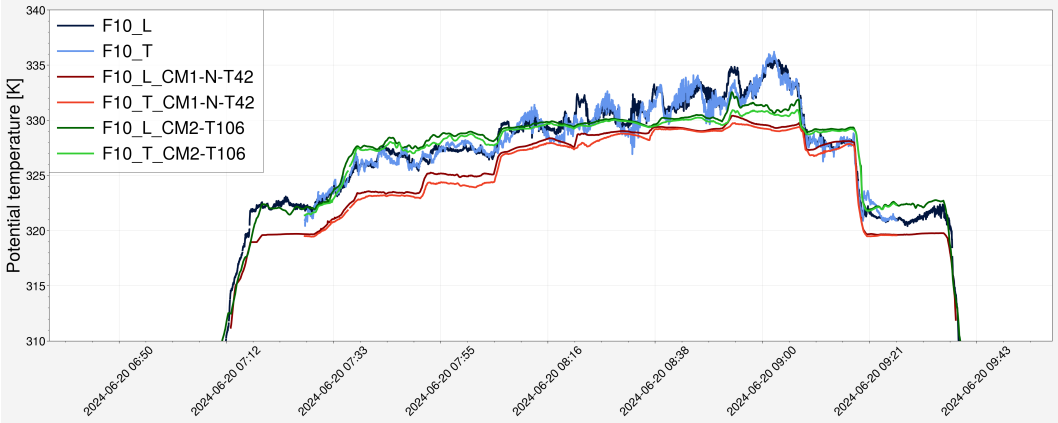

Figure 3.16: Time series of the TPEx F10 potential temperature from the Learjet (dark blue), TPC-Toss (light blue), CM1-N-T42-Learjet (dark red), CM1-N-T42-Toss (light red), CM2-T106-Learjet (green) and CM2-T106-Toss (light green).

Figure 3.16 shows the time series of the measured potential temperature from Learjet and TPC-TOSS, and the simulated path of the Learjet and TOSS by the simulations. Potential temperature is expected to increase with altitude, considering the TPC-TOSS is towed below the Learjet during the flight time, the potential temperature of the TPC-TOSS is expected to be lower than the Learjet. Exceptional circumstances could be the transportation of air mass by small scale processes e.g. turbulence, which brought the air from the lower altitude to the higher, causing a flipped relationship of potential temperature with altitude. The measured potential temperature from Learjet (dark blue) and TPC-TOSS (blue) during F10 shows multiple flips, where the TPC-TOSS measured a higher potential temperature than the Learjet, indicating possible turbulence occurrence. However,

these features are not reconstructed by either the T42 or T106 simulations. Despite the failure in reconstructing the flip, the T106 simulation at least shows better consistency on the potential temperature, while the T42 simulation is significantly cooler.

MECO(n) with chemistry

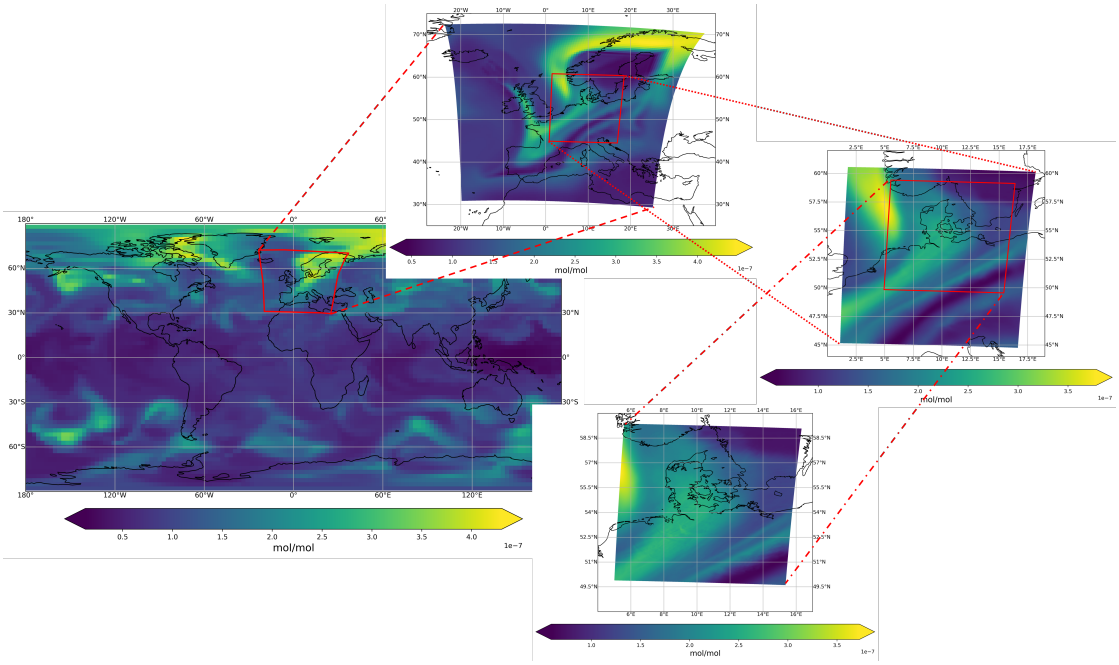

Figure 3.17: Map for ozone of the nested setup (EMAC-T42, CM40-T42, CM10, CM2) of MECO(n) at 250 hPa.

This section presents an example MECO(n) simulation prepare for TPEx I to examine the chemistry coupling in MECO(n). The simulation setup is adapted from the MECO(n) setup in Section 3.4.2 by enabling the chemistry-related submodel. Figure 3.17 shows the ozone of the EMAC-T42, CM-40-T42, CM10 and CM2. The signal from the larger instances are able to propagate and transfer to the smaller instances, with finer details, driven by the model dynamics of the smaller instances, showing the potential for investigating the chemical transport by small-scale processes using the multiple nest chemical setup of MECO(n).

3.4.5 Conclusion and outlook

To conclude, MECO(n) can represent the general synoptic features by nesting CM with higher resolution. However, the T42 EMAC resolution may lead to deviation due to its coarse resolution and affect the nested instances, leading to difficulties in direct comparison with measurements. By applying the higher T106 horizontal resolution of EMAC, the synoptic feature shows better consistency with ERA5. However, the discrepancy between CM40-T106 and EMAC-T106 is becoming larger compared to CM40-T42 and EMAC-T42. This discrepancy might be able to solved by applying spectral nudging to the COSMO instances of MECO(n). The spectral nudging (Waldron et al., 1996) is a method to force the regional model to reproduce the large-scale atmospheric state from the reanalysis or GCMs. It allows forcing not only at the boundary of the domain, but also in the interior. One possible solution in the future would be apply spectral nudging on the larger CM domain, like CM40 and CM10, considering a previous study shows a negligible effect on spectral nudging with small model domains (Schaaf et al., 2017).

4 Conclusion and Outlook

The work in this thesis improves the understanding on how tracers in the UTLS are modified by turbulence and its potential impact on the UTLS chemistry and the Earth's radiation balance. The new enhanced vertical resolution setup of MECO(n) allows a more detailed analysis on small-scale processes in the UTLS. The novel diagnostics delta tracer-tracer correlation provides a new method to investigate the impact of a single process in model experiments. The newly developed CAT submodel parametrized the turbulent mixing of tracers in the UTLS for EMAC allowing investigation on the impact of clear air turbulence in redistributing the UTLS chemistry and its radiative impact.

Results from Section 3.1 introduced an enhanced vertical setup for the multi-scale climate chemistry model MECO(n). The setup with enhanced vertical resolution in the UTLS provides a suitable tool for understanding and quantifying the small-scale bidirectional cross-tropopause transport. In this Section, a detailed analysis of turbulent mixing on tracers in the UTLS is conducted. The enhanced setup allows a better representation on the model turbulence as well as the mixing of tracers. The simulations are able to capture several distinct turbulent mixing events in the UTLS within a relatively short simulation period with different characteristics including balanced and imbalanced bidirectional mixing induced by turbulence and strong vertical tracer gradient. A novel diagnostic delta tracer-tracer correlation is introduced as well. It is the correlation between the differences of the tracers from the model experiments. This novel diagnostic is used to investigate the sole impact of a single process in the model simulation by releasing multiple tracers. This study also serves as a foundation for the following study in Section 3.2 where it proves that the turbulence diagnostic calculated from the model grid scale wind field is well matched with the highly parametrized sub-grid scale turbulence scheme of the regional model COSMO in the UTLS. This allows

a simplified parametrization scheme based on turbulence diagnostics to be applied to the climate chemistry model EMAC.

Section 3.2 examined the sensitivity of the radiatively active gases in the UTLS on turbulent mixing by introducing a newly developed CAT submodel for the climate chemistry model EMAC. The mixing scheme of CAT is based on the newly introduced turbulence diagnostic MoCATI. MoCATI is modified from the well-known Ellrod-Knox index and shows a comparable performance with the Ellrod-Knox index. The result shows that the CAT mixing scheme reduces the ozone bias at the polar mid-stratosphere compared with the satellite based data SWOOSH. It shows that the non well-mixed gases like ozone are most sensitive to turbulent mixing and are significantly modified in the UTLS. It is a result of both the physical mixing and the chemical feedback from other tracers. Ozone chemical regime is also changed by CAT, it becomes relatively more NO_x sensitive (less VOCs sensitive). The methane lifetimes are also found to be shortened by the more effective HO_x catalytic cycle. This section also shows the radiative effect of turbulent mixing in the UTLS. The turbulent mixing by clear air turbulence could lead to radiative cooling at TOA for -0.2 W/m^2, which is mainly contributed by ozone.

Section 3.3 presents an extension work of the CAT submodel by extending the mixing scheme of CAT from only applied on tracers to on water and temperature variables as well. This extension tries to mimic the mixing of an airmass; water vapour, ice water content, liquid water content and temperature is now included in the CAT mixing scheme. Result shows that the water vapour near the subtropical jet is significantly increased. The modification of water vapour by CAT could lead to a significant radiative impact of 0.79 W/m^2 at TOA.

The final section (Section 3.4) presents the preparation work for simulating the TPEx I airborne measurement campaign. This section examines the representation of MECO(n) on specific synoptic conditions. MECO(n) in general are able to represent the synoptic features by nesting COSMO with higher resolution. However, a slight mislocation of the jet system is notified under T42 horizontal resolution of EMAC which leads to difficulties in direct comparison with measurement data. Increasing horizontal resolution in EMAC could improve the representation of the jet system significantly. However, discrepancies still exist.

Outlook

This work improves the understanding and representation of turbulent mixing in climate chemistry models. The EMAC-QCTM simulations with CAT in this thesis examine the impact of CAT mixing on tracers without dynamical feedback and EMAC with nudged dynamics to examine the impact of CAT mixing on water vapour. In the future, conducting simulations with coupling between chemistry and dynamics could allow a more realistic and comprehensive estimation of how the clear air turbulence could shape the UTLS chemistry as well as the Earth's radiation budget. By applying the enhanced vertical setup for MECO(n), future studies will be able to analyse other small scale processes in the UTLS with the help of delta tracer-tracer correlation. The notification of the deviation of synoptic features in MECO(n) also provides insights into future preparation for simulating the measurement campaign.

A Bibliography

M. Baldauf, A. Seifert, J. Förstner, D. Majewski, M. Raschendorfer, and T. Reinhardt. Operational convective-scale numerical weather prediction with the cosmo model: Description and sensitivities. *Monthly Weather Review*, 139(12): 3887 – 3905, 2011. doi: 10.1175/MWR-D-10-05013.1. URL https://journals.ametsoc.org/view/journals/mwre/139/12/mwr-d-10-05013.1.xml.

W. T. Ball, N. A. Krivova, Y. C. Unruh, J. D. Haigh, and S. K. Solanki. A new satire-s spectral solar irradiance reconstruction for solar cycles 21–23 and its implications for stratospheric ozone. *Journal of the Atmospheric Sciences*, 71(11): 4086 – 4101, 2014. doi: 10.1175/JAS-D-13-0241.1. URL https://journals.ametsoc.org/view/journals/atsc/71/11/jas-d-13-0241.1.xml.

H. Bozem, P. Joppe, Y. Li, N. Emig, A. Afchine, A. Breuninger, J. Curtius, S. Hofmann, S. Ismayil, K. Kandler, D. Kunkel, A. Kutschka, H.-C. Lachnitt, A. Petzold, S. Richter, T. Röschenthaler, C. Rolf, L. Schneider, J. Schneider, A. Vogel, and P. Hoor. The tropopause composition towed sensor shuttle (tpc-toss): A new airborne dual platform approach for atmospheric composition measurements at the tropopause. *EGUsphere*, 2025:1–34, 2025. doi: 10.5194/egusphere-2025-3175. URL https://egusphere.copernicus.org/preprints/2025/egusphere-2025-3175/.

G. P. Brasseur and D. J. Jacob. *Modeling of atmospheric chemistry*. Cambridge University Press, 2017.

U. Burkhardt, B. Kärcher, M. Ponater, K. Gierens, and A. Gettelman. Contrail cirrus supporting areas in model and observations. *Geophysical Research Letters*, 35(16), 2008. doi: https://doi.org/10.1029/2008GL034056. URL https://agupubs.onlinelibrary.wiley.com/doi/abs/10.1029/2008GL034056.

N. Butchart and A. A. Scaife. Removal of chlorofluorocarbons by increased mass exchange between the stratosphere and troposphere in a changing climate. *Nature*, 410(6830):799–802, 2001.

C. H. Chau, P. Hoor, K. Kaiser, and H. Tost. Parametrizing the mixing by clear air turbulence in the chemistry climate model emac and its respective radiative impact. *EGUsphere*, 2025:1–26, 2025a. doi: 10.5194/egusphere-2025-5382. URL https://egusphere.copernicus.org/preprints/2025/egusphere-2025-5382/.

C. H. Chau, P. Hoor, and H. Tost. Simulated mixing in the utls by small-scale turbulence using multi-scale chemistry-climate model meco(n). *Atmospheric Chemistry and Physics*, 25(20):13123–13140, 2025b. doi: 10.5194/acp-25-13123-2025. URL https://acp.copernicus.org/articles/25/13123/2025/.

P. M. de F. Forster and K. P. Shine. Radiative forcing and temperature trends from stratospheric ozone changes. *Journal of Geophysical Research: Atmospheres*, 102(D9):10841–10855, 1997. doi: https://doi.org/10.1029/96JD03510. URL https://agupubs.onlinelibrary.wiley.com/doi/abs/10.1029/96JD03510.

R. Deckert, P. Jöckel, V. Grewe, K.-D. Gottschaldt, and P. Hoor. A quasi chemistry-transport model mode for emac. *Geoscientific Model Development*, 4(1):195–206, 2011. doi: 10.5194/gmd-4-195-2011. URL https://gmd.copernicus.org/articles/4/195/2011/.

D. P. Dee, S. M. Uppala, A. J. Simmons, P. Berrisford, P. Poli, S. Kobayashi, U. Andrae, M. A. Balmaseda, G. Balsamo, P. Bauer, P. Bechtold, A. C. M. Beljaars, L. van de Berg, J. Bidlot, N. Bormann, C. Delsol, R. Dragani, M. Fuentes, A. J. Geer, L. Haimberger, S. B. Healy, H. Hersbach, E. V. Hólm, L. Isaksen, P. Kållberg, M. Köhler, M. Matricardi, A. P. McNally, B. M. Monge-Sanz, J.-J. Morcrette, B.-K. Park, C. Peubey, P. de Rosnay, C. Tavolato, J.-N. Thépaut, and F. Vitart. The era-interim reanalysis: configuration and performance of the data assimilation system. *Quarterly Journal of the Royal Meteorological Society*, 137(656):553–597, 2011. doi: https://doi.org/10.1002/qj.828. URL https://rmets.onlinelibrary.wiley.com/doi/abs/10.1002/qj.828.

S. Dietmüller, P. Jöckel, H. Tost, M. Kunze, C. Gellhorn, S. Brinkop, C. Frömming, M. Ponater, B. Steil, A. Lauer, and J. Hendricks. A new radiation infrastructure for the modular earth submodel system (messy, based on version 2.51). *Geoscientific Model Development*, 9(6):2209–2222, 2016. doi: 10.5194/gmd-9-2209-2016. URL https://gmd.copernicus.org/articles/9/2209/2016/.

G. Doms, J. Förstner, E. Heise, H.-J. Herzog, D. Mironov, M. Raschendorfer, T. Reinhardt, B. Ritter, R. Schrodin, J.-P. Schulz, et al. A description of the nonhydrostatic regional cosmo model. part ii: Physical parameterization. *Deutscher Wetterdienst, Offenbach, Germany*, 2011.

J. A. Dutton and H. A. Panofsky. Clear air turbulence: A mystery may be unfolding. *Science*, 167(3920):937–944, 1970. doi: 10.1126/science.167.3920.937. URL https://www.science.org/doi/abs/10.1126/science.167.3920.937.

R. Eichinger and P. Jöckel. The generic messy submodel tendency (v1.0) for process-based analyses in earth system models. *Geoscientific Model Development*, 7(4):1573–1582, 2014. doi: 10.5194/gmd-7-1573-2014. URL https://gmd.copernicus.org/articles/7/1573/2014/.

R. Eichinger, P. Jöckel, S. Brinkop, M. Werner, and S. Lossow. Simulation of the isotopic composition of stratospheric water vapour – part 1: Description and evaluation of the emac model. *Atmospheric Chemistry and Physics*, 15(10):5537–5555, 2015. doi: 10.5194/acp-15-5537-2015. URL https://acp.copernicus.org/articles/15/5537/2015/.

G. Ellrod, P. Lester, and L. Ehernberger. Clear air turbulence. In J. R. Holton, editor, *Encyclopedia of Atmospheric Sciences*, pages 393–403. Academic Press, Oxford, 2003. ISBN 978-0-12-227090-1. doi: https://doi.org/10.1016/B0-12-227090-8/00104-4. URL https://www.sciencedirect.com/science/article/pii/B0122270908001044.

G. P. Ellrod and D. I. Knapp. An objective clear-air turbulence forecasting technique: Verification and operational use. *Weather and Forecasting*, 7(1):150 – 165, 1992. doi: 10.1175/1520-0434(1992)007⟨0150:AOCATF⟩2.

0.CO;2. URL https://journals.ametsoc.org/view/journals/wefo/7/1/1520-0434_1992_007_0150_aocatf_2_0_co_2.xml.

G. P. Ellrod and J. A. Knox. Improvements to an operational clear-air turbulence diagnostic index by addition of a divergence trend term. *Weather and Forecasting*, 25(2):789 – 798, 2010. doi: 10.1175/2009WAF2222290.1. URL https://journals.ametsoc.org/view/journals/wefo/25/2/2009waf2222290_1.xml.

J. G. Esler and L. M. Polvani. Kelvin–helmholtz instability of potential vorticity layers: A route to mixing. *Journal of the Atmospheric Sciences*, 61 (12):1392 – 1405, 2004. doi: 10.1175/1520-0469(2004)061⟨1392:KIOPVL⟩2.0.CO;2. URL https://journals.ametsoc.org/view/journals/atsc/61/12/1520-0469_2004_061_1392_kiopvl_2.0.co_2.xml.

P. Forster, T. Storelvmo, K. Armour, W. Collins, J.-L. Dufresne, D. Frame, D. J. Lunt, T. Mauritsen, M. D. Palmer, M. Watanabe, M. Wild, and H. Zhang. The earth's energy budget, climate feedbacks, and climate sensitivity. In V. Masson-Delmotte, P. Zhai, A. Pirani, S. L. Connors, C. Péan, S. Berger, N. Caud, Y. Chen, L. Goldfarb, M. I. Gomis, M. Huang, K. Leitzell, E. Lonnoy, J. B. R. Matthews, T. K. Maycock, T. Waterfield, O. Yelekçi, R. Yu, and B. Zhou, editors, *Climate Change 2021: The Physical Science Basis. Contribution of Working Group I to the Sixth Assessment Report of the Intergovernmental Panel on Climate Change*, chapter 7, pages 923–1054. Cambridge University Press, Cambridge, United Kingdom and New York, NY, USA, 2021. doi: 10.1017/9781009157896.009.

P. M. d. F. Forster and K. P. Shine. Assessing the climate impact of trends in stratospheric water vapor. *Geophysical Research Letters*, 29(6):10–1–10–4, 2002. doi: https://doi.org/10.1029/2001GL013909. URL https://agupubs.onlinelibrary.wiley.com/doi/abs/10.1029/2001GL013909.

A. Gettelman, P. Hoor, L. L. Pan, W. J. Randel, M. I. Hegglin, and T. Birner. The extratropical upper troposphere and lower stratosphere. *Reviews of Geophysics*, 49(3), 2011. doi: https://doi.org/10.1029/2011RG000355. URL https://agupubs.onlinelibrary.wiley.com/doi/abs/10.1029/2011RG000355.

M. A. Giorgetta, E. Manzini, E. Roeckner, M. Esch, and L. Bengtsson. Climatology and forcing of the quasi-biennial oscillation in the maecham5 model. *Journal of Climate*, 19(16):3882 – 3901, 2006. doi: 10.1175/JCLI3830.1. URL https://journals.ametsoc.org/view/journals/clim/19/16/jcli3830.1.xml.

M. A. Giorgetta, R. Brokopf, T. Crueger, M. Esch, S. Fiedler, J. Helmert, C. Hohenegger, L. Kornblueh, M. Köhler, E. Manzini, T. Mauritsen, C. Nam, T. Raddatz, S. Rast, D. Reinert, M. Sakradzija, H. Schmidt, R. Schneck, R. Schnur, L. Silvers, H. Wan, G. Zängl, and B. Stevens. Icon-a, the atmosphere component of the icon earth system model: I. model description. *Journal of Advances in Modeling Earth Systems*, 10(7):1613–1637, 2018. doi: https://doi.org/10.1029/2017MS001242. URL https://agupubs.onlinelibrary.wiley.com/doi/abs/10.1029/2017MS001242.

V. Grewe. The origin of ozone. *Atmospheric Chemistry and Physics*, 6(6):1495–1511, 2006. doi: 10.5194/acp-6-1495-2006. URL https://acp.copernicus.org/articles/6/1495/2006/.

J. D. Haigh. The sun and the earth's climate. *Living reviews in solar physics*, 4 (1):2, 2007.

D. H. Hathaway. The solar cycle. *Living reviews in solar physics*, 12(1):4, 2015.

H. Hersbach, B. Bell, P. Berrisford, S. Hirahara, A. Horányi, J. Muñoz-Sabater, J. Nicolas, C. Peubey, R. Radu, D. Schepers, A. Simmons, C. Soci, S. Abdalla, X. Abellan, G. Balsamo, P. Bechtold, G. Biavati, J. Bidlot, M. Bonavita, G. De Chiara, P. Dahlgren, D. Dee, M. Diamantakis, R. Dragani, J. Flemming, R. Forbes, M. Fuentes, A. Geer, L. Haimberger, S. Healy, R. J. Hogan, E. Hólm, M. Janisková, S. Keeley, P. Laloyaux, P. Lopez, C. Lupu, G. Radnoti, P. de Rosnay, I. Rozum, F. Vamborg, S. Villaume, and J.-N. Thépaut. The era5 global reanalysis. *Quarterly Journal of the Royal Meteorological Society*, 146(730):1999–2049, 2020. doi: https://doi.org/10.1002/qj.3803. URL https://rmets.onlinelibrary.wiley.com/doi/abs/10.1002/qj.3803.

C. O. Hines. Doppler-spread parameterization of gravity-wave momentum deposition in the middle atmosphere. part 1: Basic formulation. *Journal of*

Atmospheric and Solar-Terrestrial Physics, 59(4):371–386, 1997. ISSN 1364-6826. doi: https://doi.org/10.1016/S1364-6826(96)00079-X. URL https://www.sciencedirect.com/science/article/pii/S136468269600079X.

J. R. Holton, P. H. Haynes, M. E. McIntyre, A. R. Douglass, R. B. Rood, and L. Pfister. Stratosphere-troposphere exchange. *Reviews of Geophysics*, 33(4):403–439, 1995. doi: https://doi.org/10.1029/95RG02097. URL https://agupubs.onlinelibrary.wiley.com/doi/abs/10.1029/95RG02097.

P. Hoor. The tropopause region in a changing atmosphere (tpchange). https://utls.ipa.uni-mainz.de/tpchange/, 2022. Accessed: 2025-11-16.

B. Hu, J. Tang, J. Ding, and G. Liu. Regional downscaled future change of clear-air turbulence over east asia under rcp8.5 scenario within the cordex-ea-ii project. *International Journal of Climatology*, 41(10):5022–5035, 2021. doi: https://doi.org/10.1002/joc.7114. URL https://rmets.onlinelibrary.wiley.com/doi/abs/10.1002/joc.7114.

J. Imbrie, E. A. Boyle, S. C. Clemens, A. Duffy, W. R. Howard, G. Kukla, J. Kutzbach, D. G. Martinson, A. McIntyre, A. C. Mix, B. Molfino, J. J. Morley, L. C. Peterson, N. G. Pisias, W. L. Prell, M. E. Raymo, N. J. Shackleton, and J. R. Toggweiler. On the structure and origin of major glaciation cycles 1. linear responses to milankovitch forcing. *Paleoceanography*, 7 (6):701–738, 1992. doi: https://doi.org/10.1029/92PA02253. URL https://agupubs.onlinelibrary.wiley.com/doi/abs/10.1029/92PA02253.

A. B. M. Jeuken, P. C. Siegmund, L. C. Heijboer, J. Feichter, and L. Bengtsson. On the potential of assimilating meteorological analyses in a global climate model for the purpose of model validation. *Journal of Geophysical Research: Atmospheres*, 101(D12):16939–16950, 1996. doi: https://doi.org/10.1029/96JD01218. URL https://agupubs.onlinelibrary.wiley.com/doi/abs/10.1029/96JD01218.

P. Jöckel, R. Sander, A. Kerkweg, H. Tost, and J. Lelieveld. Technical note: The modular earth submodel system (messy) - a new approach towards earth system modeling. *Atmospheric Chemistry and Physics*, 5(2):433–444, 2005. doi: 10.

5194/acp-5-433-2005. URL https://acp.copernicus.org/articles/5/433/2005/.

P. Jöckel, H. Tost, A. Pozzer, C. Brühl, J. Buchholz, L. Ganzeveld, P. Hoor, A. Kerkweg, M. G. Lawrence, R. Sander, B. Steil, G. Stiller, M. Tanarhte, D. Taraborrelli, J. van Aardenne, and J. Lelieveld. The atmospheric chemistry general circulation model echam5/messy1: consistent simulation of ozone from the surface to the mesosphere. *Atmospheric Chemistry and Physics*, 6(12):5067–5104, 2006. doi: 10.5194/acp-6-5067-2006. URL https://acp.copernicus.org/articles/6/5067/2006/.

P. Jöckel, A. Kerkweg, J. Buchholz-Dietsch, H. Tost, R. Sander, and A. Pozzer. Technical note: Coupling of chemical processes with the modular earth submodel system (messy) submodel tracer. *Atmospheric Chemistry and Physics*, 8(6):1677–1687, 2008. doi: 10.5194/acp-8-1677-2008. URL https://acp.copernicus.org/articles/8/1677/2008/.

P. Jöckel, A. Kerkweg, A. Pozzer, R. Sander, H. Tost, H. Riede, A. Baumgaertner, S. Gromov, and B. Kern. Development cycle 2 of the modular earth submodel system (messy2). *Geoscientific Model Development*, 3(2):717–752, 2010. doi: 10.5194/gmd-3-717-2010. URL https://gmd.copernicus.org/articles/3/717/2010/.

P. Jöckel, H. Tost, A. Pozzer, M. Kunze, O. Kirner, C. A. M. Brenninkmeijer, S. Brinkop, D. S. Cai, C. Dyroff, J. Eckstein, F. Frank, H. Garny, K.-D. Gottschaldt, P. Graf, V. Grewe, A. Kerkweg, B. Kern, S. Matthes, M. Mertens, S. Meul, M. Neumaier, M. Nützel, S. Oberländer-Hayn, R. Ruhnke, T. Runde, R. Sander, D. Scharffe, and A. Zahn. Earth system chemistry integrated modelling (escimo) with the modular earth submodel system (messy) version 2.51. *Geoscientific Model Development*, 9(3):1153–1200, 2016. doi: 10.5194/gmd-9-1153-2016. URL https://gmd.copernicus.org/articles/9/1153/2016/.

J. W. Kaiser, A. Heil, M. O. Andreae, A. Benedetti, N. Chubarova, L. Jones, J.-J. Morcrette, M. Razinger, M. G. Schultz, M. Suttie, and G. R. van der

Werf. Biomass burning emissions estimated with a global fire assimilation system based on observed fire radiative power. *Biogeosciences*, 9(1):527–554, 2012. doi: 10.5194/bg-9-527-2012. URL https://bg.copernicus.org/articles/9/527/2012/.

T. Kaluza, D. Kunkel, and P. Hoor. On the occurrence of strong vertical wind shear in the tropopause region: a 10-year era5 northern hemispheric study. *Weather and Climate Dynamics*, 2(3):631–651, 2021. doi: 10.5194/wcd-2-631-2021. URL https://wcd.copernicus.org/articles/2/631/2021/.

J. L. Keller. Clear air turbulence as a response to meso- and synoptic-scale dynamic processes. *Monthly Weather Review*, 118(10):2228 – 2243, 1990. doi: 10.1175/1520-0493(1990)118⟨2228:CATAAR⟩2.0.CO;2. URL https://journals.ametsoc.org/view/journals/mwre/118/10/1520-0493_1990_118_2228_cataar_2_0_co_2.xml.

A. Kerkweg and P. Jöckel. The 1-way on-line coupled atmospheric chemistry model system meco(n) – part 2: On-line coupling with the multi-model-driver (mmd). *Geoscientific Model Development*, 5(1):111–128, 2012a. doi: 10.5194/gmd-5-111-2012. URL https://gmd.copernicus.org/articles/5/111/2012/.

A. Kerkweg and P. Jöckel. The 1-way on-line coupled atmospheric chemistry model system meco(n) – part 1: Description of the limited-area atmospheric chemistry model cosmo/messy. *Geoscientific Model Development*, 5(1):87–110, 2012b. doi: 10.5194/gmd-5-87-2012. URL https://gmd.copernicus.org/articles/5/87/2012/.

A. Kerkweg and P. Jöckel. The infrastructure messy submodels grid (v1.0) and import (v1.0). *Geoscientific Model Development Discussions*, 8:8607–8633, 2015. doi: 10.5194/gmdd-8-8607-2015. URL https://gmd.copernicus.org/preprints/8/8607/2015/.

A. Kerkweg, J. Buchholz, L. Ganzeveld, A. Pozzer, H. Tost, and P. Jöckel. Technical note: An implementation of the dry removal processes dry deposition and sedimentation in the modular earth submodel system (messy). *Atmospheric*

Chemistry and Physics, 6(12):4617–4632, 2006a. doi: 10.5194/acp-6-4617-2006. URL https://acp.copernicus.org/articles/6/4617/2006/.

A. Kerkweg, R. Sander, H. Tost, and P. Jöckel. Technical note: Implementation of prescribed (offlem), calculated (onlem), and pseudo-emissions (tnudge) of chemical species in the modular earth submodel system (messy). *Atmospheric Chemistry and Physics*, 6(11):3603–3609, 2006b. doi: 10.5194/acp-6-3603-2006. URL https://acp.copernicus.org/articles/6/3603/2006/.

A. Kerkweg, C. Hofmann, P. Jöckel, M. Mertens, and G. Pante. The on-line coupled atmospheric chemistry model system meco(n) – part 5: Expanding the multi-model-driver (mmd v2.0) for 2-way data exchange including data interpolation via grid (v1.0). *Geoscientific Model Development*, 11(3):1059–1076, 2018. doi: 10.5194/gmd-11-1059-2018. URL https://gmd.copernicus.org/articles/11/1059/2018/.

A. Kerkweg, T. Kirfel, D. H. Do, S. Griessbach, P. Jöckel, and D. Taraborrelli. The messy dwarf (based on messy v2.55.2). *Geoscientific Model Development*, 18(4):1265–1286, 2025. doi: 10.5194/gmd-18-1265-2025. URL https://gmd.copernicus.org/articles/18/1265/2025/.

S. A. Klein, Y. Zhang, M. D. Zelinka, R. Pincus, J. Boyle, and P. J. Gleckler. Are climate model simulations of clouds improving? an evaluation using the isccp simulator. *Journal of Geophysical Research: Atmospheres*, 118(3):1329–1342, 2013. doi: https://doi.org/10.1002/jgrd.50141. URL https://agupubs.onlinelibrary.wiley.com/doi/abs/10.1002/jgrd.50141.

A. A. Lacis, D. J. Wuebbles, and J. A. Logan. Radiative forcing of climate by changes in the vertical distribution of ozone. *Journal of Geophysical Research: Atmospheres*, 95(D7):9971–9981, 1990. doi: https://doi.org/10.1029/JD095iD07p09971. URL https://agupubs.onlinelibrary.wiley.com/doi/abs/10.1029/JD095iD07p09971.

S. H. Lee, P. D. Williams, and T. H. Frame. Increased shear in the north atlantic upper-level jet stream over the past four decades. *Nature*, 572(7771):639–642, 2019.

J. Lelieveld and F. J. Dentener. What controls tropospheric ozone? *Journal of Geophysical Research: Atmospheres*, 105(D3):3531–3551, 2000. doi: https://doi.org/10.1029/1999JD901011. URL https://agupubs.onlinelibrary.wiley.com/doi/abs/10.1029/1999JD901011.

M. B. McElroy, R. J. Salawitch, and K. Minschwaner. The changing stratosphere. *Planetary and space science*, 40(2-3):373–401, 1992.

D. S. McKenna, P. Konopka, J.-U. Grooß, G. Günther, R. Müller, R. Spang, D. Offermann, and Y. Orsolini. A new chemical lagrangian model of the stratosphere (clams) 1. formulation of advection and mixing. *Journal of Geophysical Research: Atmospheres*, 107(D16):ACH 15–1–ACH 15–15, 2002. doi: https://doi.org/10.1029/2000JD000114. URL https://agupubs.onlinelibrary.wiley.com/doi/abs/10.1029/2000JD000114.

MESSy consortium. Messy$_p$*oster*$_v$7., 2015. Accessed: Oct 1, 2025.

M. Milankovitch. Kanon der erdbestrahlung und seine anwendung auf das eiszeitenproblem. *Royal Serbian Academy Special Publication*, 133:1–633, 1941.

K. Mohanakumar. *Stratosphere troposphere interactions: an introduction*. Springer, 2008.

D. Muñoz-Esparza, R. D. Sharman, and S. B. Trier. On the consequences of pbl scheme diffusion on utls wave and turbulence representation in high-resolution nwp models. *Monthly Weather Review*, 148(10):4247 – 4265, 2020. 10.1175/MWR-D-20-0102.1. URL https://journals.ametsoc.org/view/journals/mwre/148/10/mwrD200102.xml.

M. Nützel, L. Stecher, P. Jöckel, F. Winterstein, M. Dameris, M. Ponater, P. Graf, and M. Kunze. Updating the radiation infrastructure in messy (based on messy version 2.55). *Geoscientific Model Development*, 17(15):5821–5849, 2024. 10.5194/gmd-17-5821-2024. URL https://gmd.copernicus.org/articles/17/5821/2024/.

A. Overeem. *Verification of clear-air turbulence forecasts*. KNMI De Bilt, The Netherlands, 2002.

J. Penner, M. Andreae, H. Annegarn, L. Barrie, J. Feichter, D. Hegg, A. Jayaraman, R. Leaitch, D. Murphy, J. Nganga, et al. Aerosols, their direct and indirect effects. In *TAR Climate Change 2001: The Scientific Basis*. 2001.

R. Pincus and B. Stevens. Paths to accuracy for radiation parameterizations in atmospheric models. *Journal of Advances in Modeling Earth Systems*, 5(2): 225–233, 2013. https://doi.org/10.1002/jame.20027. URL `https://agupubs.onlinelibrary.wiley.com/doi/abs/10.1002/jame.20027`.

A. Pozzer, P. Jöckel, R. Sander, J. Williams, L. Ganzeveld, and J. Lelieveld. Technical note: The messy-submodel airsea calculating the air-sea exchange of chemical species. *Atmospheric Chemistry and Physics*, 6(12):5435–5444, 2006. 10.5194/acp-6-5435-2006. URL `https://acp.copernicus.org/articles/6/5435/2006/`.

W. J. Randel, F. Wu, and P. Forster. The extratropical tropopause inversion layer: Global observations with gps data, and a radiative forcing mechanism. *Journal of the Atmospheric Sciences*, 64(12):4489 – 4496, 2007. 10.1175/2007JAS2412.1. URL `https://journals.ametsoc.org/view/journals/atsc/64/12/2007jas2412.1.xml`.

M. Riese, F. Ploeger, A. Rap, B. Vogel, P. Konopka, M. Dameris, and P. Forster. Impact of uncertainties in atmospheric mixing on simulated utls composition and related radiative effects. *Journal of Geophysical Research: Atmospheres*, 117 (D16), 2012. https://doi.org/10.1029/2012JD017751. URL `https://agupubs.onlinelibrary.wiley.com/doi/abs/10.1029/2012JD017751`.

G. Ritchie. *Atmospheric Chemistry: from the Surface to the Stratosphere*. World Scientific Publishing Company, 2017.

E. Roeckner, G. Bäuml, L. Bonaventura, R. Brokopf, M. Esch, M. Giorgetta, S. Hagemann, I. Kirchner, L. Kornblueh, E. Manzini, et al. The atmospheric general circulation model echam 5. part i: Model description. 2003.

E. Roeckner, R. Brokopf, M. Esch, M. Giorgetta, S. Hagemann, L. Kornblueh, E. Manzini, U. Schlese, and U. Schulzweida. Sensitivity of simulated climate to horizontal and vertical resolution in the echam5 atmosphere model. *Journal*

of Climate, 19(16):3771 – 3791, 2006. 10.1175/JCLI3824.1. URL https://journals.ametsoc.org/view/journals/clim/19/16/jcli3824.1.xml.

R. Sander, A. Kerkweg, P. Jöckel, and J. Lelieveld. Technical note: The new comprehensive atmospheric chemistry module mecca. *Atmospheric Chemistry and Physics*, 5(2):445–450, 2005. 10.5194/acp-5-445-2005. URL https://acp.copernicus.org/articles/5/445/2005/.

R. Sander, A. Baumgaertner, S. Gromov, H. Harder, P. Jöckel, A. Kerkweg, D. Kubistin, E. Regelin, H. Riede, A. Sandu, D. Taraborrelli, H. Tost, and Z.-Q. Xie. The atmospheric chemistry box model caaba/mecca-3.0. *Geoscientific Model Development*, 4(2):373–380, 2011. 10.5194/gmd-4-373-2011. URL https://gmd.copernicus.org/articles/4/373/2011/.

R. Sander, P. Jöckel, O. Kirner, A. T. Kunert, J. Landgraf, and A. Pozzer. The photolysis module jval-14, compatible with the messy standard, and the jval preprocessor (jvpp). *Geoscientific Model Development*, 7(6):2653–2662, 2014. 10.5194/gmd-7-2653-2014. URL https://gmd.copernicus.org/articles/7/2653/2014/.

R. Sander, A. Baumgaertner, D. Cabrera-Perez, F. Frank, S. Gromov, J.-U. Grooß, H. Harder, V. Huijnen, P. Jöckel, V. A. Karydis, K. E. Niemeyer, A. Pozzer, H. Riede, M. G. Schultz, D. Taraborrelli, and S. Tauer. The community atmospheric chemistry box model caaba/mecca-4.0. *Geoscientific Model Development*, 12(4):1365–1385, 2019. 10.5194/gmd-12-1365-2019. URL https://gmd.copernicus.org/articles/12/1365/2019/.

B. Schaaf, H. von Storch, and F. Feser. Does spectral nudging have an effect on dynamical downscaling applied in small regional model domains? *Monthly Weather Review*, 145(10):4303 – 4311, 2017. 10.1175/MWR-D-17-0087.1. URL https://journals.ametsoc.org/view/journals/mwre/145/10/mwr-d-17-0087.1.xml.

J. Seinfeld and S. Pandis. *Atmospheric chemistry and physics: from air pollution to climate change*. Wiley-Interscience, 2006.

M. A. Shapiro. Turbulent mixing within tropopause folds as a mechanism for the exchange of chemical constituents between the stratosphere and troposphere. *Journal of Atmospheric Sciences*, 37(5):994 – 1004, 1980. 10.1175/1520-0469(1980)037¡0994:TMV

URL https://journals.ametsoc.org/view/journals/atsc/37/5/1520-0469_1980_037_0994_tmwtfa_2_0_co_2.xml.

I. H. Smith, P. D. Williams, and R. Schiemann. Clear-air turbulence trends over the north atlantic in high-resolution climate models. *Climate Dynamics*, 61(7): 3063–3079, 2023.

D. S. Spiegel, S. N. Raymond, C. D. Dressing, C. A. Scharf, and J. L. Mitchell. Generalized milankovitch cycles and long-term climatic habitability. *The Astrophysical Journal*, 721(2):1308, sep 2010. 10.1088/0004-637X/721/2/1308. URL https://doi.org/10.1088/0004-637X/721/2/1308.

M. Sprenger, M. Croci Maspoli, and H. Wernli. Tropopause folds and cross-tropopause exchange: A global investigation based upon ecmwf analyses for the time period march 2000 to february 2001. *Journal of Geophysical Research: Atmospheres*, 108(D12), 2003. https://doi.org/10.1029/2002JD002587. URL https://agupubs.onlinelibrary.wiley.com/doi/abs/10.1029/2002JD002587.

G. L. Stephens, J. Li, M. Wild, C. A. Clayson, N. Loeb, S. Kato, T. L'ecuyer, P. W. Stackhouse Jr, M. Lebsock, and T. Andrews. An update on earth's energy balance in light of the latest global observations. *Nature Geoscience*, 5(10):691–696, 2012.

B. Stevens, M. Giorgetta, M. Esch, T. Mauritsen, T. Crueger, S. Rast, M. Salzmann, H. Schmidt, J. Bader, K. Block, R. Brokopf, I. Fast, S. Kinne, L. Kornblueh, U. Lohmann, R. Pincus, T. Reichler, and E. Roeckner. Atmospheric component of the mpi-m earth system model: Echam6. *Journal of Advances in Modeling Earth Systems*, 5(2):146–172, 2013. https://doi.org/10.1002/jame.20015. URL https://agupubs.onlinelibrary.wiley.com/doi/abs/10.1002/jame.20015.

D. S. Stevenson, F. J. Dentener, M. G. Schultz, K. Ellingsen, T. P. C. van Noije, O. Wild, G. Zeng, M. Amann, C. S. Atherton, N. Bell, D. J. Bergmann, I. Bey, T. Butler, J. Cofala, W. J. Collins, R. G. Derwent, R. M. Doherty, J. Drevet, H. J. Eskes, A. M. Fiore, M. Gauss, D. A. Hauglustaine, L. W. Horowitz, I. S. A. Isaksen, M. C. Krol, J.-F. Lamarque, M. G. Lawrence, V. Montanaro, J.-F. Müller, G. Pitari, M. J. Prather, J. A. Pyle, S. Rast, J. M. Rodriguez, M. G. Sanderson, N. H. Savage, D. T. Shindell, S. E. Strahan, K. Sudo, and S. Szopa. Multimodel ensemble simulations of present-day and near-future tro-

pospheric ozone. *Journal of Geophysical Research: Atmospheres*, 111(D8), 2006. https://doi.org/10.1029/2005JD006338. URL https://agupubs.onlinelibrary.wiley.com/doi/abs/10.1029/2005JD006338.

A. Stohl, P. Bonasoni, P. Cristofanelli, W. Collins, J. Feichter, A. Frank, C. Forster, E. Gerasopoulos, H. Gäggeler, P. James, T. Kentarchos, H. Kromp-Kolb, B. Krüger, C. Land, J. Meloen, A. Papayannis, A. Priller, P. Seibert, M. Sprenger, G. J. Roelofs, H. E. Scheel, C. Schnabel, P. Siegmund, L. Tobler, T. Trickl, H. Wernli, V. Wirth, P. Zanis, and C. Zerefos. Stratosphere-troposphere exchange: A review, and what we have learned from staccato. *Journal of Geophysical Research: Atmospheres*, 108(D12), 2003. https://doi.org/10.1029/2002JD002490. URL https://agupubs.onlinelibrary.wiley.com/doi/abs/10.1029/2002JD002490.

L. N. Storer, P. D. Williams, and M. M. Joshi. Global response of clear-air turbulence to climate change. *Geophysical Research Letters*, 44(19):9976–9984, 2017. https://doi.org/10.1002/2017GL074618. URL https://agupubs.onlinelibrary.wiley.com/doi/abs/10.1002/2017GL074618.

H. Tost, P. Jöckel, A. Kerkweg, R. Sander, and J. Lelieveld. Technical note: A new comprehensive scavenging submodel for global atmospheric chemistry modelling. *Atmospheric Chemistry and Physics*, 6(3):565–574, 2006a. 10.5194/acp-6-565-2006. URL https://acp.copernicus.org/articles/6/565/2006/.

H. Tost, P. Jöckel, and J. Lelieveld. Influence of different convection parameterisations in a gcm. *Atmospheric Chemistry and Physics*, 6(12):5475–5493, 2006b. 10.5194/acp-6-5475-2006. URL https://acp.copernicus.org/articles/6/5475/2006/.

H. Tost, P. Jöckel, and J. Lelieveld. Lightning and convection parameterisations ndash; uncertainties in global modelling. *Atmospheric Chemistry and Physics*, 7(17):4553–4568, 2007. 10.5194/acp-7-4553-2007. URL https://acp.copernicus.org/articles/7/4553/2007/.

H. Tost, M. G. Lawrence, C. Brühl, P. Jöckel, T. G. Team, and T. S.-O.-D. Team. Uncertainties in atmospheric chemistry modelling due to convection parameterisations and subsequent scavenging. *Atmospheric Chemistry and Physics*, 10(4):1931–1951, 2010. 10.5194/acp-10-1931-2010. URL https://acp.copernicus.

org/articles/10/1931/2010/.

M. Traub and J. Lelieveld. Cross-tropopause transport over the eastern mediterranean. *Journal of Geophysical Research: Atmospheres*, 108(D23), 2003. https://doi.org/10.1029/2003J URL https://agupubs.onlinelibrary.wiley.com/doi/abs/10.1029/2003JD003754.

K. M. Waldron, J. Paegle, and J. D. Horel. Sensitivity of a spectrally filtered and nudged limited-area model to outer model options. *Monthly Weather Review*, 124 (3):529 – 547, 1996. 10.1175/1520-0493(1996)124¡0529:SOASFA¿2.0.CO;2. URL https://journals.ametsoc.org/view/journals/mwre/124/3/1520-0493_1996_124_0529_soasfa_2_0_co_2.xml.

P. Warneck. *Chemistry of the natural atmosphere*, volume 71. Elsevier, 1999.

C. Watkins and K. Browning. The detection of clear air turbulence by radar. *Physics in Technology*, 4(1):28, jan 1973. 10.1088/0305-4624/4/1/I01. URL https://doi.org/10.1088/0305-4624/4/1/I01.

P. D. Williams. Increased light, moderate, and severe clear-air turbulence in response to climate change. *Advances in atmospheric sciences*, 34(5):576–586, 2017.

P. D. Williams and M. M. Joshi. Intensification of winter transatlantic aviation turbulence in response to climate change. *Nature Climate Change*, 3(7):644–648, 2013.

J. K. Wolff and R. D. Sharman. Climatology of upper-level turbulence over the contiguous united states. *Journal of Applied Meteorology and Climatology*, 47 (8):2198 – 2214, 2008. 10.1175/2008JAMC1799.1. URL https://journals.ametsoc.org/view/journals/apme/47/8/2008jamc1799.1.xml.

World Meteorological Organization. World meteorological organization bulletin. *World Meteorol. Org. Bull.*, 6:136, 1957.